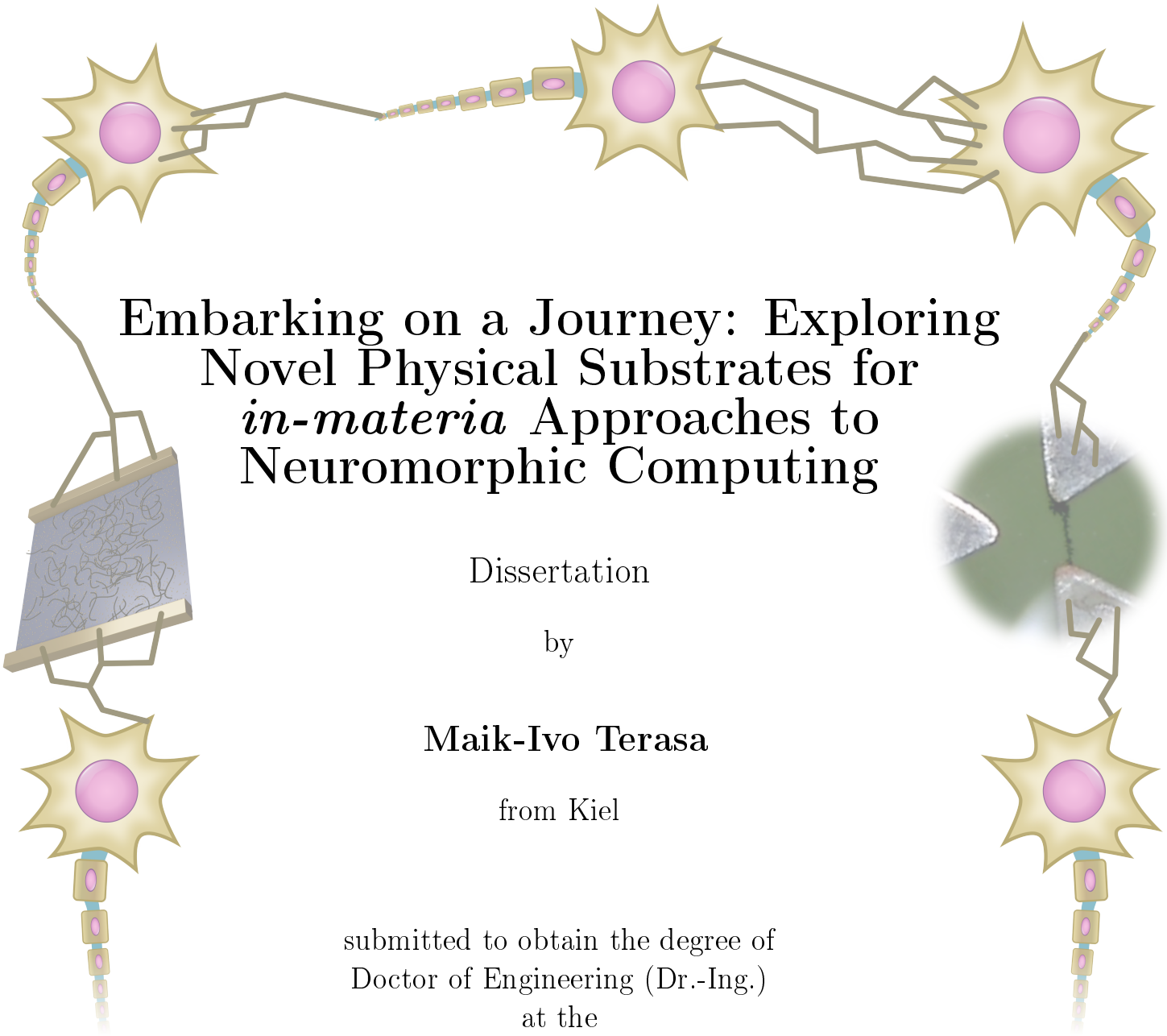

Embarking on a Journey: Exploring Novel Physical Substrates for *in-materia* Approaches to Neuromorphic Computing

Dissertation

by

Maik-Ivo Terasa

from Kiel

submitted to obtain the degree of
Doctor of Engineering (Dr.-Ing.)
at the
Department of Materials Science
Faculty of Engineering
Kiel University

Kiel, 2024

Date of oral examination: 22.05.2024

First examiner: **Rainer Adelung**
Chair for Functional Nanomaterials
Faculty of Engineering, Kiel University

Second examiner: **Hermann Kohlstedt**
Chair for Nanoelectronics
Faculty of Engineering, Kiel University

Declaration of Authorship

I hereby declare that this thesis and the respective research, except for scientific supervision by my supervisor, was independently composed and authored by myself.
This work complies with the DFG recommendations for safeguarding good scientific practice. All content and ideas drawn directly or indirectly from external sources are clearly indicated.
This thesis has not been published or been submitted to any other examining body and all related research items that have been composed and published in peer-review journals are clearly indicated as such.
I declare that no academic degree has been withdrawn from me.

Kiel, January 22nd 2024

Maik-Ivo Terasa

The Fellowship of the Thesis

The time during which this thesis has been created has been and still is a significant part of my life. There are many people to whom I owe my gratitude for being with me on this adventure. Of course including all who are not explicitly mentioned here, I am who and where I am thanks to you!

Prof. Rainer Adelung, the **Shooting Star**, tirelessly leading the way, as a shining beacon of scientific notion. Only by your grace was I allowed to embark on this journey and only by your guidance was I able to keep my destination in sight.
May you walk beyond the stars and unravel the universe.

Sören Kaps, the **Atlas**, he who carries so many worlds on his shoulders with a titanic endurance. You are the foundation that all of my accomplishments are built upon. You are the hand that catches my fall, the one that drags me up and the one that pushes me onwards. Words cannot express your importance for this part of my life. Without you I would never have arrived.

Pia Pooker, the **Song of Harmony**, who never stops to fill the world around her with love, compassion and positivity; who I long to hear every day. Had you not been in my life I would have missed your melody so dearly. Please never stop smiling. Please never stop singing.

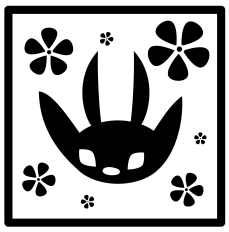

Roshani Madurawala, the **Ori**, a galaxy of kindness orbiting a giant star of unmatched power and potential. Never would I have wished for someone else to succeed me. Never would I have expected to find this uniqueness near me.
Spread your wings and fly. Blast on and reach for the sky.

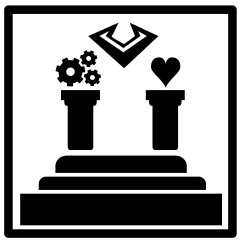

Jörg Bahr, the **Paragon**, an icon of craftsmanship, benevolence and wisdom alike. An icon I will never stop to look up to. You stand far above so many and yet stand right beside us. It is an honour and serendipity to sit next to you; to grasp the excellence you emanate and the compassion you share.

Everybody else from the FUN group, the **Ark**, the community, that provides a safe and welcoming haven for anyone in the rough and uncharted seas of science. Driven by mutual respect it is steered in a team effort where every individual matters. Instead of a chore, you have made this journey a breeze, that I wanted to return to every day.

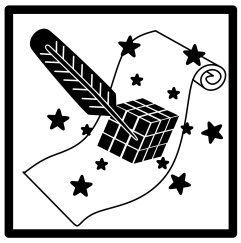

Vivien Wehr and **Beate Minten**, the **Wizards**, defending us from the Beast of Bureaucracy. As unassuming heroes you cast the shield that wards us, so we can work in peace. As brave champions you fight the stacks of paper we procreate every day. Nothing would be possible without you.

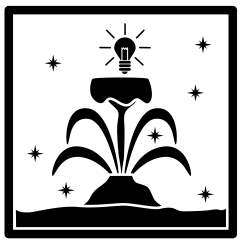

Alexander Vahl, the **Mountain Spring**, from which the waters of knowledge flow in an endless stream, but always calm and of flawless purity. Whenever I was in need, I could come to you, relaxing by your tranquility while sating my thirst. May your virtues be as valued as they have been valuable to me, wherever you will go.

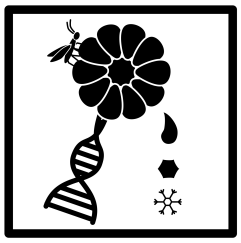

Prof. Franz Faupel, **Prof. Hermann Kohlstedt** and their groups, the **Aspects of Emergence**, a myriad of stories testifying that a gathering of parts can be so much more than their sum. You have written some with me and I would be honoured to write some further.

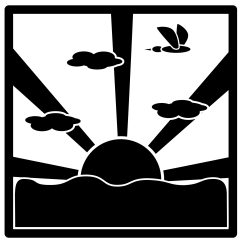

Christian Lasch and **Svenja Thiel**, the **Calm Skies**, where I could float among the clouds with pizza or cards or beer or blue shells. Where everyday life slows from a rush to a still and its sorrows are only distant apparitions. You are an essential key for keeping my sanity.

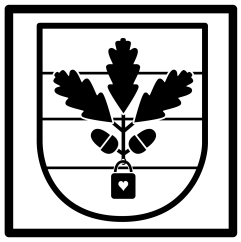

My **mother** and my sisters **Berit**, **Cristin** and **Katja**, the **Heartbound**, that always have my back with their unconditional support. You cannot choose your family but even if I could I would never want another.

My wife **Jenny**, my kids **Gwendolyn** and **Tristan**, my **precious**, my **sunshine**, my **anchor**, my **well of serenity**, my **reason to carry on**.
All I do, I do for you.

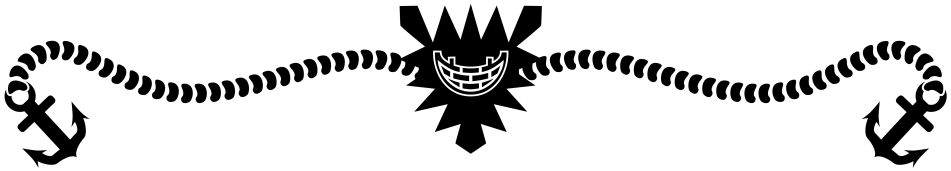

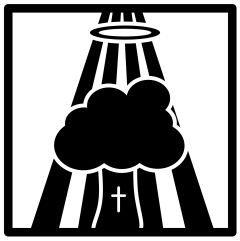

Finally, **Lutz Terasa**, the **Memory**, who left this world before I was able to live up to my promise. Your love and dedication will forever be a part of this work.
Until we meet again, so I can show it to you.

Abstract

The ongoing digitalization of society imposes new challenges on science and technology to address the ever growing energy demand and physical limits reached in miniaturization of electronic circuits and devices. The increasing need for computational resources in the form of processing units, memory storage and sensor systems clashes with the boundaries of today's conventional serial computing architectures, e.g. with the von-Neumann bottleneck.
Thus, inspiration has started to be taken from information processing in organic life forms that show capabilities to perform cognitive tasks and solve complex problems; all with a remarkable energy efficiency, as biological systems have been shaped and optimized over millions of years of evolution.
Research avenues like machine learning, neuromorphic computing and *in-materia* computing have started to emerge taking biological neural networks as a model to mimic or to harness their advantageous properties, resulting from their structure and functioning.
This thesis explores new material systems beyond silicon-based components and circuits to act as physical substrates for *in-materia* approaches, aiming to complement the capabilities of existing neuromorphic devices.
To support the assessment of this work's results, the following three aspects of a neuromorphic system are defined:

- **The component space:** Representing individual building blocks such as artificial neurons or memristors, making up the functional part of the system.
- **The network space:** Representing the arrangement of the components, the way they are interconnected and how these interconnections evolve spatio-temporally.
- **The design space:** Representing pre-determined sections of a network with a specific functionality, e.g. the input layer for external signals to the network.

For the component space with a tangent to the network space, a new concept for a lateral memristor is presented making use of superimposed sparse networks of both carbon nanotubes as well as bimetallic nanoparticles. The electrochemical

metallization-type resistive switching shows a second-scale retention time, which makes the approach conceivable as a component to emulate a short-term memory effect and occupy the regime between non-volatile and highly volatile memristive cells. Moreover, the fabrication route of the sparse nanotube network is a promising facile starting point for substrates towards reservoir computing applications.
Furthermore, mainly in the context of the network space, two approaches are discussed to alter the topology of a network via electrical stimuli in a liquid matrix to avoid fixed, two-dimensional wiring schemes, as found e.g. in cross-bar arrays:

- Specific conductive interconnections are grown between two explicit electrodes via electrochemical metallization, based on the electrical signal applied. This approach mimics various neuromorphic features such as plasticity, true three-dimensionality, long-term potentiation and coupled oscillator synchronization.
- A network of ZnO nanoparticles is exposed to oscillating electrical fields leading to a collective change of topology via dielectrophoresis. The UV-sensitivity as a gauge for the particle density is used as a measure to assess the connection strength between nodes unifying plasticity with sensor properties of metal oxide particles.

As part of the design space, it is explored how Direct Ink Writing (DIW) can be deployed in research and development as a method for the rapid prototyping and fabrication of functional sensor circuits with ZnO-based sensors as an example system. A special emphasis is put on the degrees of freedom provided by both the Direct Ink Writing and the subsequent laser milling technique yielding flexible, freestanding sensor devices. Furthermore, it is discussed how the doping and decoration of metal oxide materials can be used to tune the sensor properties, adding even more versatility to the approach.
The results of this work provide a solid perspective on how exploring new material platforms is a valuable step for the development of physical substrates of neuromorphic research that aim to overcome limitations exhibited by current silicon-based circuits. Novel material-based approaches as well as their respective fabrication routes promotes broader design considerations contributing to the development of material systems for bio-inspired *in-materia* computing.

Kurzfassung

Die fortschreitende Digitalisierung der Gesellschaft stellt Wissenschaft und Technologie vor neue Herausforderungen, um den stetig wachsenden Energiebedarf und die physikalischen Grenzen der Miniaturisierung von elektronischen Schaltkreisen und Geräten zu bewältigen. Der zunehmende Bedarf an Rechenressourcen in Form von Prozessoreinheiten, Speicherplatz und Sensorsystemen stößt an die Grenzen der heutigen, konventionellen, seriellen Rechenarchitekturen, z. B. den von-Neumann-Flaschenhals.
Daher begann die Wissenschaft, Inspiration aus der Informationsverarbeitung in organischen Lebensformen zu ziehen, die die Fähigkeit zur Durchführung kognitiver Aufgaben und zur Lösung komplexer Probleme zeigen. Dies geschieht mit bemerkenswerter Energieeffizienz, da biologische Systeme über Millionen Jahre der Evolution geformt und optimiert wurden.
Forschungsbereiche wie maschinelles Lernen, neuromorphes Computing und *in-materia*-Computing sind entstanden und verwenden biologische neuronale Netzwerke als Modellsysteme, um deren vorteilhafte Eigenschaften, die in ihrer Struktur und Funktionsweise begründet sind, zu imitieren und zu nutzen.
Diese Arbeit erforscht neue Materialsysteme jenseits von siliziumbasierten Komponenten und Schaltkreisen, die als physische Substrate für *in-materia*-Ansätze dienen sollen, um die Fähigkeiten vorhandener neuromorpher Systeme zu ergänzen.
Zur Unterstützung der Bewertung der Ergebnisse dieser Arbeit werden die folgenden drei Aspekte eines neuromorphen Systems definiert:

- **Der Komponentenraum:** Repräsentiert einzelne Bausteine wie künstliche Neuronen oder Memristoren, die den funktionalen Teil des Systems ausmachen.

- **Der Netzwerkraum:** Repräsentiert die Anordnung der Komponenten, wie sie miteinander verbunden sind und wie sich diese Verbindungen räumlich und zeitlich entwickeln.

- **Der Designraum:** Repräsentiert vorbestimmte Abschnitte eines Netzwerks mit einer spezifischen Funktionalität, z. B. die Schnittstelle für externe Signale in das Netzwerk.

Für den Komponentenraum, mit Berührungspunkten zum Netzwerkraum, wird ein neues Konzept für einen lateralen Memristor vorgestellt, das auf überlagerten spärlichen Netzwerken von sowohl Kohlenstoffnanoröhren als auch bimetallischen Nanopartikeln basiert. Das resistive Schalten, das über elektrochemische Metallisierung funktioniert, zeigt eine Retentionszeit im Sekundenbereich, was den Ansatz denkbar macht als Komponente zur Implementierung eines Kurzzeitgedächtniseffektes wodurch es den Bereich zwischen nichtflüchtigen und hochflüchtigen memristiven Zellen ausfüllt. Darüber hinaus ist der Herstellungsweg des spärlichen Kohlenstoffnanoröhrennetzwerks ein vielversprechender Ausgangspunkt für Substrate in Anwendungen im Reservoir-Computing.
Weiterhin werden, hauptsächlich im Kontext des Netzwerkraums, zwei Ansätze diskutiert, die die Topologie eines Netzwerks über elektrische Anregung in einer flüssigen Matrix verändern, wodurch festgelegte zweidimensionale Verschaltungsschemata, wie sie z.B. in Cross-Bar-Arrays zu finden sind, vermeiden werden:

- Spezifische leitfähige Verbindungen werden zwischen zwei expliziten Elektroden durch elektrochemische Metallisierung generiert, basierend auf dem angelegten elektrischen Signal. Dieser Ansatz imitiert verschiedene neuromorphe Merkmale wie Plastizität, echte Dreidimensionalität, Langzeitpotenzierung und Synchronisation von gekoppelten Oszillatoren.

- Ein Netzwerk von ZnO-Nanopartikeln wird oszillierenden elektrischen Feldern ausgesetzt, was zu einer kollektiven Änderung der Topologie durch Dielektrophorese führt. Die UV-Sensitivität in Abhängigkeit der Partikeldichte wird als Maßstab verwendet für die Verbindungsstärke zwischen Knoten, wodurch Plastizität mit den Sensor-Eigenschaften von Metalloxidpartikeln vereint wird.

Als Teil des Designraums wird untersucht, wie das Direct-Ink-Writing (DIW) in Forschung und Entwicklung als Methode für das schnelle Prototyping und die Herstellung funktionaler Sensor-Schaltkreise verwendet werden kann, wobei ZnO-basierte Sensoren als Beispiel gezeigt werden. Ein besonderer Schwerpunkt liegt auf den Freiheitsgraden, die sowohl das DIW als auch die anschließende Technik des Laserfräsens bieten. Darüber hinaus wird diskutiert, wie die Dotierung und Dekoration von Metalloxidmaterialien genutzt werden können, um die Sensor-Eigenschaften gezielt zu beeinflussen, was dem Ansatz noch mehr Vielseitigkeit verleiht.
Die Ergebnisse dieser Arbeit bieten eine Perspektive darauf, wie die Erforschung neuer Materialplattformen ein wertvoller Schritt ist für die Entwicklung physischer Substrate in der neuromorphen Forschung, die u.a. darauf abzielen, die Einschränkungen aktueller siliziumbasierter Schaltkreise zu überwinden. Neuartige materialbasierte Ansätze sowie ihre jeweiligen Herstellungsmethoden fördern umfassendere Designüberlegungen und tragen zur Entwicklung von Materialsystemen für bioinspiriertes *in-materia*-Computing bei.

Contents

Acronyms

AM	Additive manufacturing
CAD	Computer-aided design
CNC	Computerized numerical control
CNT	Carbon nanotube
DIW	Direct ink writing
DMSO	Dimethyl sulfoxide
ECM	Electrochemical metallization
EDX	Energy-dispersive X-ray spectroscopy
FIB	Focused ion-beam
GAS	Gas-aggregation source
GND	Ground potential
HRS	High resistive state
ISI	Interspike intervals
LED	Light emitting diode
LRS	Low resistive state
LTP	Long-term potentiation
MB	Methylene blue
MOS	Metal oxide semiconductor
MWCNT	Multi-walled carbon nanotube
NP	Nanoparticle
PCB	Printed circuit board
PEDOT	Poly(3,4-ethylenedioxythiopene)
PSS	Polystyrene sulfonate
PVB	Polyvinyl butyral
SMU	Source measure unit
STDP	Spike-timing dependent plasticity
SWCNT	Single-walled carbon nanotube
t-ZnO	Tetrapodal zinc oxide
UV	Ultraviolet

Chapter 1

Introduction

Since life has started to inhabit the earth about 4 billion years ago[1], living organisms have been shaped by the principles of Darwinistic evolution, continuously adapting to ever changing environments[2]. Among the most remarkable features that have developed over the millions of years of evolution are the capabilities of perception and the consequential performing of cognitive tasks[3].
Perceiving the immediate or remote vicinity allows to collect information to improve on finding food sources, possible mating partners or avoiding present predators, which enhances the chances of survival and reproduction.
A link between sensory capabilities and motor response as well as adaptive behaviour has already been shown in single-celled organisms like bacteria or slime-moulds[4, 5]. But the development of a nervous system allowed for increasingly complex cognitive actions with remarkable energy efficiency. Central aspects of efficient cognition are pattern recognition and memory, as these allow to perform heuristic predictions without the need to gather all information repeatedly. As an example, remembering the shape, colours and sounds of a predator enable a prey to recognize and avoid them even before an attack. Not only does it provide a survival advantage by avoiding danger but also energetically as it requires less energy to recall existing information than to store new ones. In this context the principle of Hebbian learning plays a crucial role, sometimes also referred to as "What fires together wires together". This phrase refers to that the repetition of concurrent information gradually improves their concurrent recall, where the experiment by Ivan Pavlov on a dog's conditioning is likely the most popular example: Seeing food lets a dog salivate, where a bell ring alone does not. However, after repeated concurrent exposure to food and a bell ring, the bell's sound alone led to the dog salivating. The information of seeing food and hearing the sound have been linked so that the perception of one leads to the recall and thus according behaviour of the other.

Now, how is the field of neurobiology linked to material science and technology? With the transition towards smart cities, the "internet of things" and the resulting

mass of data, also referred to as "Big Data", the need for computational resources will continue to increase dramatically. The same holds for the according power consumption as both the number of users and devices as well as the power demand per user grows[6, 7]. This issue also applies to the accelerating development and utilization of artificial intelligence (AI) to complement and expand human capabilities.
Scientists and engineers are inspired to tackle the arising challenges of the digital age by taking nature as an example due to its non-deterministic way of processing information as well as its high energy efficiency.
However, to understand this motivation, one has to consider the way modern digital computers operate:
Conventional computers have been developed as pure calculators i.e. for solving mathematical problems based on serial algorithmic computation. Despite extraordinary technological advances, the basic working principle grounded on boolean operations and the von-Neumann architecture, in which the processing unit and data storage are separate, is still present in today's silicon-based systems.
Extreme calculation speed and vast storage space has made digital computers a central part of modern society, so that they are deployed for all kinds of information processing.
However, the von-Neumann architecture has shown to reach severe limitations referred to as the "von-Neumann bottleneck"[8]. With an ever increasing size of data sets, the limiting factor in the computational performance is not the speed of the processing unit itself but instead the communication between data storage and processor, which also results in higher energy consumption[9]. Furthermore, processing units have reached physical limitations in terms of operating frequency and miniaturization, so that it has become necessary to parallelize the hardware into multi-core CPUs and computing clusters.
So facing these roadblocks while attempting to keep up with the growing demand for computational resources, a new research avenue has emerged to complement existing technology: shifting the computing scheme to approach the architecture of "biological computers", first and foremost the central nervous system and the brain.

The astounding capabilities and efficiency of the nervous system are founded on its structure and the mechanisms making it up. The basic building block of the nervous system is the neuron or nerve cell, that generates dendrites, synapses and axons to connect to other neurons. These neurons form a neural network that can vary drastically in size, from a few thousand nerve cells in a polyp[10] to many billions in the human brain[11]. Each neuron can have more than 10,000 synaptic connections to others, that serve as conveyors for the neuron's activity.
For neurons, a direct link between biology and electrical engineering has been established by modelling the propagation of action potentials as an electrical circuit

first with time-variant resistors and later with memristors[12, 13].
In a neural network the connections between neurons and thus the paths along which signals are transmitted, are capable of changing continuously, i.e. they can grow stronger or decay depending on the network's activity. This plasticity is an essential mechanism of a neural network and tightly bound to an organism's ability to learn and adapt.

The way scientists and engineers are driven towards emulating biological information processing, due to its unique features, has manifested in three main routes that are pursued: Machine learning, neuromorphic engineering and *in-materia* computing.
Machine learning is the approach to mimic signal processing and storage of neural networks on an abstract level. It is already employed in many different popular applications as artificial intelligence (AI), such as text generation (ChatGPT, [14]), image generation (Stable Diffusion, [15]), personalization in social media and many more. It is also heavily researched for medical applications, already showing how diagnostics are improved by machine learning methods[16–18].
A prominent core feature of machine learning are artificial neural networks (ANN). ANNs are - inspired by networks of neurons and synapses - abstract models composed of layers of nodes that are connected by edges[19]. However, since the network only exists in a computer, it is purely represented by numbers and the operation of the network, including the training, is performed by heavy calculations of the output values and edge weights[20].
So despite its merits machine learning, as it is implemented today, is a severely energy demanding method; especially when compared to its biological role model, the human brain, whose power consumption of around 20 W is only a fraction of that of a conventional digital computer under computational load[21].
Neuromorphic engineering in its current state aims to create very-large-scale-integrated circuits (VLSI circuits), with both digital and analogue components to overcome the limitations of classical von-Neumann computing[22, 23]. A prominent aspect in this context is highly parallelized in-memory computing[24–26]. However, these circuits are still limited by their two-dimensional wiring scheme, which imposes severe constraints on the connectivity in contrast to biological three-dimensional networks.
The term *in-materia* computing describes how a physical system is subjected to a computer-controlled input and reacts via material interactions producing a processed output signal[27]. This is commonly displayed in the context of reservoir computing via networks of nano-objects[28–30], but it has also been shown that self-organized networks of metal nanoparticles exhibit brain-like dynamics in the form of spike avalanches and a state of criticality when subjected to electrical input[31–34].

This work in particular introduces new material systems as complementary substrates for neuromorphic assemblies, that aim to complement existing merits of neuromorphic devices.
To support the assessment of this work's results, the following three aspects of a neuromorphic system are defined (also displayed in *Figure 1.1*):
The **component space** represents individual self-contained building blocks like artificial neurons that make up the functional nodes of a neuromorphic network. Among the most prominent candidates for those building blocks is the *memristor*, a two-terminal device whose internal state determines its resistance. Memristors are broadly investigated as non-volatile memory components but also for in-memory computing and are considered to be an essential part of neuromorphic engineering.
The **network space** represents the topology of the network, i.e. how individual nodes are interconnected, and the spatio-temporal changes of these connections. Properties like modularity and a "small-world"-configuration have a severe impact on the efficiency of signal propagation through the network[35]. The way the component space impacts and reacts to the network space is a central factor for the operation of the system.
Finally, the **design space** represents all additional functional parts of the network, that are integrated into it by design to serve a specific purpose. While plasticity is an essential feature of the working principle of a neuromorphic network, there will most likely also be sections that are supposed to fulfil a designated role, that requires a fixed, pre-determined blueprint. For example, analogous to the visual perception via photoreceptors in nature, external input to a neuromorphic network might be provided by an arrangement of sensor components. Thus, while the processing of the signal is subject to the network's plasticity, the intake of the stimulus has to be ensured by stable sensor operation.

Considering these spaces, the results presented in the chapters 3, 4 and 5 are

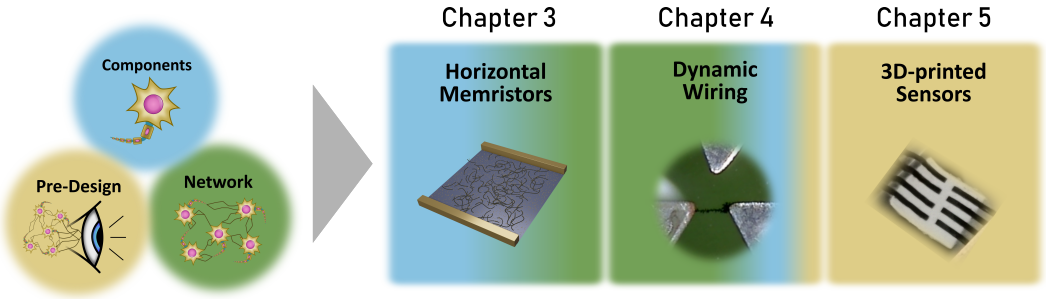

Figure 1.1: *Graphical illustration of the structure of this thesis. Each chapter is attributed to one or more aspects of a neural network: Individual components such as neurons, networking mechanisms like plasticity determining the topology and pre-designed parts, such as systems for sensory input.*

referred to them, as depicted in *Figure 1.1*, to support the discussion of their role in a neuromorphic assembly.
First, in *Chapter* 3 the development and technical realization of a new lateral memristor concept is presented, that is based on the superposition of sparse networks of both carbon nanotubes as well as bimetallic nanoparticles. It shows a hybrid resistive switching mode between diffusive and bipolar switching as well as a retention time in the second regime made available by a limitation of Ag as the active species. In contrast, current memristive devices are fabricated either as non-volatile with a retention of thousands of seconds up to many years[36] or as volatile where most show a retention in the range of ns to ms[37], missing out on the middle-ground in the range of several s. Thus, as part of the component space this memristor concept fills an intermediate role as a conceivable, biologically plausible short-term memory. Additionally, the chapter is at a tangent to the network space due to the sparse network of carbon nanotubes, whose facile fabrication route provides the basis for multi-terminal approaches, such as reservoir computing, as well.
When considering a network of components, the commonly deployed static two-dimensional wiring schemes of cross-bar arrays exhibit a limited pre-defined connectivity[38]. This is in stark contrast to the dynamic, three-dimensional structure of biological neural networks, where connections between neurons are generated when required. In *Chapter* 4 the search for wiring schemes beyond a static cross-bar architecture is addressed by presenting two material systems capable of generating three-dimensional material-based network interconnections dynamically according to an electrical input. One acts via dielectrophoresis of dielectric particles, the other via electrochemical metallization. The presented approaches are mainly attributed to the network space as they offer a degree of plasticity for the topology of a network but also border on the component space and design space as well.
Finally, *Chapter* 5 tackles the challenge of a facile fabrication of pre-designed functional components for an integration into neuromorphic circuits as sensory input. Direct Ink Writing as a type of additive manufacturing is presented as a fabrication method to obtain sensor devices based on functional micro-particles with ZnO as an example system. Being part of the design space, the technique motivates the search for new particle-based materials with sensor capabilities incentivized by its tremendous versatility with respect to material choices and geometry of the sensor component.

Chapter 2

Theoretical Background

This chapter provides the background knowledge required to understand the experiments and results presented in this work. This includes the theoretical treatment of all relevant topics as well as a fundamental introduction of the more involved fabrication and characterization techniques.

2.1 Memristors

2.1.1 Introducing the Memristor Concept

Today, memristive devices are considered to be an essential building block for bio-inspired brain-like computing architectures. However, the initial description of the memristor and its placement in the scientific landscape have been purely theoretical in nature:
The term memristor has been coined by Leon O. Chua in 1971 as a portmanteau from the words *memory* and *resistor*[39]. He described the memristor as the fourth basic passive circuit element besides the resistor, inductor and capacitor. His reasoning based on symmetry and completeness. The four circuit variables, i.e. current I, voltage U, charge Q and magnetic flux Φ, as well as the relations between them and the time t had been formulated as:

$$\begin{aligned} \int_{-\infty}^{t} I(t)dt &= Q \\ \int_{-\infty}^{t} U(t)dt &= \Phi \\ dQ/dU &= C \\ d\Phi/dI &= L \\ dU/dI &= R \end{aligned}$$

With C, L and R being capacitance, inductance and resistance respectively as displayed in *Figure 2.1a*. However, there was the relation missing, that linked magnetic flux Φ and charge Q, which Chua defined as

$$d\Phi/dQ \quad = \quad M$$

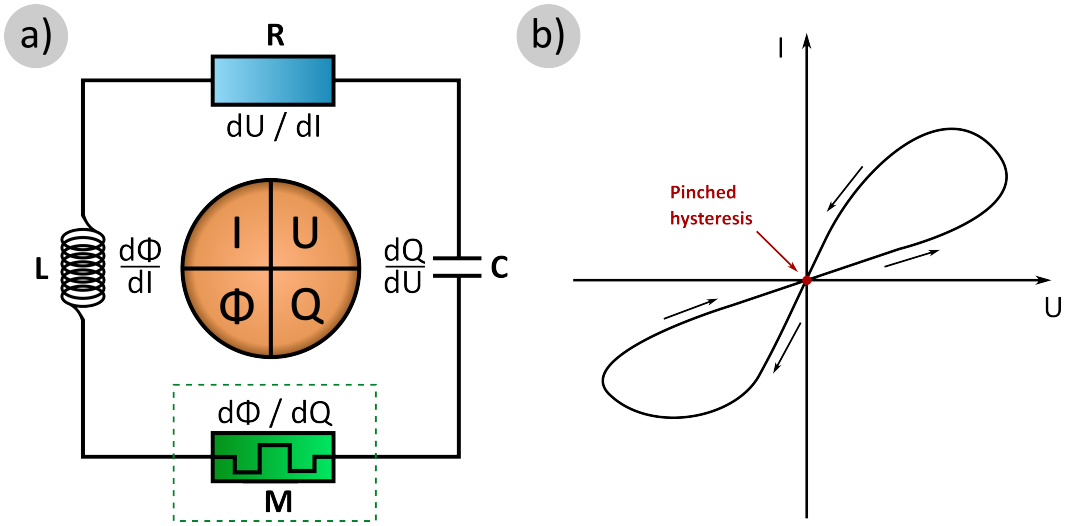

Figure 2.1: *a) Graphical representation of the relations between the fundamental circuit elements. The green dashed line indicates how the memristance M has been introduced based on symmetry considerations.*
b) Schematic IV-behaviour of a theoretical memristor showing the pinched hysteresis denoted by the arrows and the pinch point at the origin.

where $M(Q)$ has been called a *memristance* indicated by the green dashed line in *Figure 2.1a*. The term has been chosen due to the fact, that it behaves like a *resistor*, with the twist that its resistance depends on the total charge Q that has passed the memristor's terminals. Therefore, it depends on the history of the current flowing through it, i.e. its time integral from $-\infty$ to t_0. A more generalized concept about memristive systems has been published a few years later, where Chua et *al.* also elaborated on how different systems - including the Hodgkin-Huxley model of the neuron - can be modelled with memristor theory[40].
However, the practical relevance was minor until - many years later in 2008 - Strukov et *al.* presented a physical device based on non-stochiometric TiO_x whose hysteretic I-V behaviour was described by the equations of Chua's theoretical work[41]. Two main features have been assigned to identify a system as a memristor:

1. The resistance must be a function of the internal state, which in turn must depend on the preceding current history.

2. It's a passive element, so at zero voltage there must be zero current flowing.

These two requirements are fulfilled by a so-called "pinched hysteresis" in the memristors IV-behaviour, which is schematically depicted in *Figure 2.1b*, where, in addition to the hysteretic shape, the pinch point at the origin satisfies the passivity condition.

2.1.2 Memristive Switching

In the context of improving digital memory systems, various mechanisms for resistive switching have been studied well before the publication of Strukov's memristor. Material systems for resistive random access memory cells (ReRAM)[42, 43] have been investigated as well as magnetic effects such as spin torque transfer magnetization switching (STS)[44] or ferroelectric tunneling junctions (FTJ)[45, 46] for magnetic and ferroelectric random access memory cells (MRAM and FeRAM respectively).
After Strukov et al. brought the concept of the "memristor" into the spotlight, the term "resistive switching" got extended by several additional mechanisms, where the most common ones will be discussed below. For the sake of clarity the following terms will be introduced explicitly, which are essential for the description of resistive switching devices:
The term *SET* operation is used to denote bringing the system from its High Resistive State (HRS) to its Low Resistive State (LRS). The reverse is denoted as a RESET operation, bringing the system from its LRS back to its HRS.
The time for which a LRS is stable is denoted as the "retention time".

2.1.2.1 Switching Mechanisms

It is worth mentioning that resistive switching is investigated in a large variety of systems such as Phase Change Materials (PCM), where switching occurs between crystalline and amorphous phases[47–49], carbon- and polymer based materials[50, 51] or even biological memristors made of soy[52, 53]. However, to stay in the scope of this work, the two most common mechanisms are described in more detail: The **Valence Change Mechanism (VCM)** is introduced since it is the most widely studied process for memristive switching and **Electrochemical Metallization (ECM)** is described in more detail, as it is most important for the results of this work.

Valence Change Mechanism (VCM):
A widely investigated material class for resistive switching applications are non-stochiometric metal oxides[54]. VCM devices commonly consist of a sandwich

structure with two electrodes made of inert metals such as Pt or Au and in between them a structure of layers of one or more metal oxides[55]. This structure contains non-stochiometric oxides, which are rich in oxygen vacancies, e.g. Pt/-TiO_2/TiO_{2-x}/Pt[41] or Pt/SiO_2/Ta_2O_{5-x}/TaO_{2-x}/Pt[56].
The resistance of a layer is determined by the concentration and distribution of oxygen vacancies, as these introduce defect states into the band structure of the metal oxide and thus act as a dopant[54, 57]. The oxygen anions are mobile and drift in an electrical field applied to the electrodes, so that the dopant concentration shifts and forms conductive filaments eventually. Thus it is also called anion-based switching. Kwon et *al.* have visualized the formation of a Ti_4O_7 phase in a TiO_2 layer and have shown the higher conductivity in the non-stochiometric phase[58]. Schematics of the HRS and LRS in such a system are shown in *Figure 2.2.*

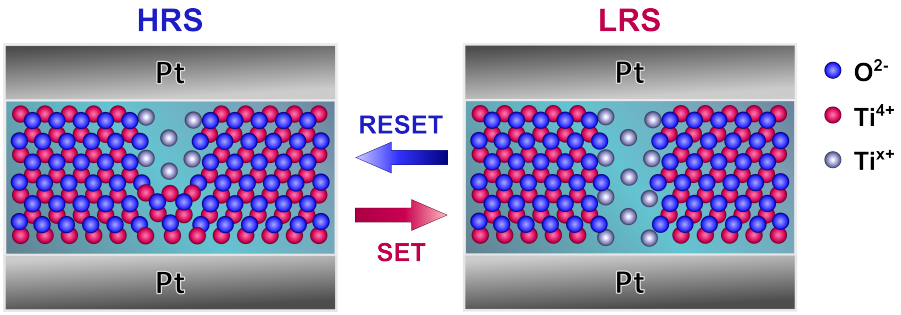

Figure 2.2: *Schematic depiction of the SET and RESET states of a TiO_2 based VCM memristor.*

Electrochemical metallization (ECM):
The most common configuration for ECM-based memristors are a sandwich of an insulating matrix between two electrodes made of different metals: one is inert (Pt, Au), while the other one is electrochemically more active (Cu, Ag)[59].
In terms of energy, the terms "inert" and "active" can be described such (after [60]): The Gibbs free energy for oxidation $\Delta_f G$ of a species in ECM cells has to be positive, so that the reduced state is stable and the ions do not form metal oxides. For large values of $\Delta_f G$ the electrode material is "inert" as its oxidation requires large potentials. Consequently, the ideal candidate for the active species has a $\Delta_f G$, that is positive but as small as possible, so that it can be easily oxidized, but is stable in its metallic phase. This is reflected by Cu and Ag ($\Delta_f G_{(Cu^+/Cu)} = 50\ kJmol^{-1}$ and $\Delta_f G_{(Ag^+/Ag)} = 77\ kJmol^{-1}$) being the most common active electrode materials compared to Au ($\Delta_f G_{(Au^+/Au)} = 177\ kJmol^{-1}$), which is considered as inert.

Applying a suitable voltage to an ECM cell leads to an electrochemical redox reaction at the anode oxidizing metal atoms of the active species. Thus this mechanism is also called cation-based switching. The resulting cations drift in the electrical field through the separation layer towards the cathode, where they are reduced to metal atoms again and form a conductive filament between the electrodes:

$$\text{Anode: } M \rightarrow M^{z+} + ze^{-} \tag{2.1}$$

$$\downarrow \qquad \text{Drift of } M^{z+} \qquad \downarrow$$

$$\text{Cathode: } M^{z+} + ze^{-} \rightarrow M \tag{2.2}$$

M is the active metal species and z the valence of the metal ion.
The tip formed by the first metal atoms reduced at the cathode acts as an electrical field concentrator, so that new atoms preferably reduce at the leading tip of the filament[61]. Once the metal filament crosses the insulating layer, the conductivity between the electrodes switches from insulator-determined to metal-determined (HRS $\rightarrow$ LRS, i.e. the *SET* process) by establishing a galvanic or tunneling contact[62].
The kinetics of electrochemical metallization are dominated by the charge-transfer between electrode and reactive species in the separation layer, which is described by the current density J_{Me} according to the Butler-Volmer equation[63]:

$$J_{Me} = J_0 * \left[\exp\left(\frac{(1-\alpha)ze}{k_B T}U_i\right) - \exp\left(\frac{\alpha ze}{k_B T}U_i\right)\right] \tag{2.3}$$

where J_0 is the exchange current density, U_i is the overpotential, α is the transfer coefficient, z is the number of electrons exchanged in the redox-reaction, e is the elementary charge, k_B is the Boltzmann constant and T is the temperature.
Considering the current density, the filament growth speed can be derived from Faraday's law of electrolysis to

$$\frac{\partial x}{\partial t} = \frac{m_{Me}}{ze\rho_{Me}} J_{Me} \tag{2.4}$$

where x is the length of the filament, m_{Me} is the atomic mass of the metal and ρ_{Me} is the metal's density[63]. The derivation can be found in *Appendix* A.1.

The RESET mechanism of an ECM device involves the filament to collapse to return to matrix-determined conductance. A constant driving force for the collapse is the minimization of surface energy, i.e. from an elongated filament shape towards

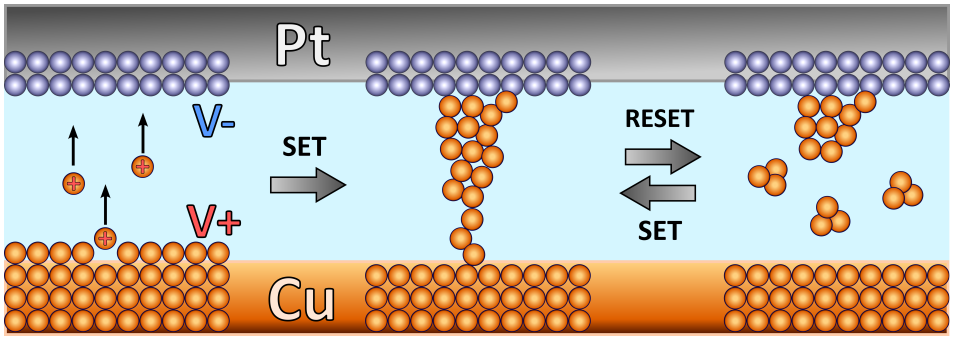

Figure 2.3: *Schematic depiction of the SET and RESET mechanisms for ECM type resistive switching. The formation and dissolution of the metal filament through the separation layer changes the resistance state respectively.*

an energetically favourable spherical shape[61]. This transition relies on surface diffusion of metal atoms on the filament, which is highly temperature dependent. Thus, Joule heating is considered a main factor for resetting galvanically contacted bipolar ECM devices[64, 65]. In case of a tunneling contact the redox processes can as well be reversed, so that the filament is oxidized and dissolves[62].
The constant driving force to minimize surface energy leads to a limited filament lifetime, which is mainly dependent on its size[66]. Since the collapse of the filament is equivalent to a state switch LRS → HRS, its lifetime is a direct measure of the device's retention time.

2.1.2.2 Behaviour of IV-Hysteresis

In addition to the switching mechanism, memristors are categorized by the behaviour of their IV-hysteresis. One aspect is the number of resistance states (see *Figure 2.4*), which classifies a memristor's switching as:

- **Binary:** Two discrete resistance states
- **Multi-level:** More than two discrete resistance states
- **Analogue:** A multitude of continuous resistance states

Binary switching is the most common and basic switching type. Its two states are referred to as low-resistive state (LRS) and high-resistive state (HRS) and directly reflect the presence or absence of its conductive state. For filamentary switching, which is the case for VCM and ECM systems, this refers to the formation and rupture of the conductive filament. For STS, in contrast, the two states are determined by the parallel or anti-parallel spin orientation of the two

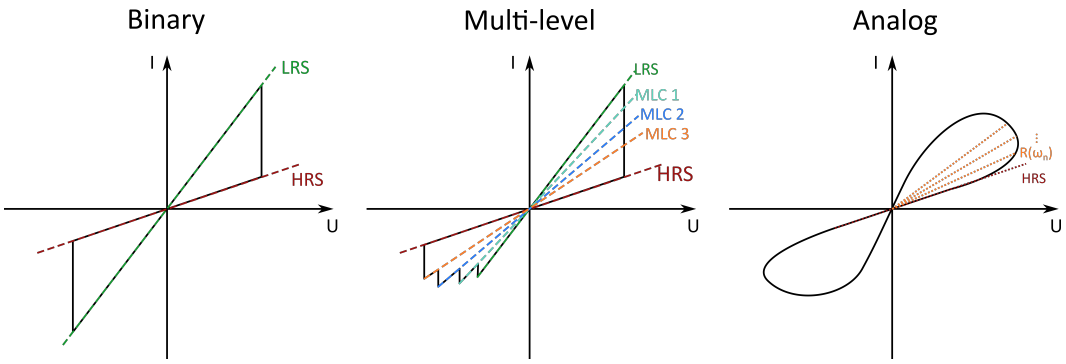

Figure 2.4: *Possible resistance state modes for resistive switching. In binary mode it is only distinguished between HRS and LRS (also referred to as OFF/ON respectively). Multi-level switching is characterized by intermediate states (MLC = Multi-level cell). For the theoretical analog switching the resistance state is continuous and given by the internal state variable* ω_n.

ferromagnetic layers[44].

The term **multi-level switching** is used to describe cells that are stable in multiple resistance states, which have been attributed to various origins, such as the shape of the conductive filament and a respective modulation of the Schottky barrier to the electrode material[67–70]. Another example reported for resistive switching in a layer of reduced graphene oxide (RGO) proposed the gradual formation of a high-resistance graphene oxide layer at the interface between the RGO and an indium tin oxide (ITO) electrode due to oxygen diffusion[71]. Careful voltage or current control is applied to enable a specific resistance state, mostly reached from the LRS.

Finally, **analogue switching** is a type of multi-level switching but with the capability to change the device state in sufficiently small steps to consider it continuously. For example, in [72] a continuous series of few hundred resistance states has been shown, controlled by accordingly small steps of either voltage or current limitation. Analogue switching is especially interesting for analogue matrix multiplication applications.

The other aspect of the IV-hysteresis used to categorize resistive switching is the polarity of *SET* and *RESET* operations (see also *Figure 2.5*):

- **Bipolar:** The polarities for *SET* and *RESET* have opposite signs.
- **Unipolar:** The polarities for *SET* and *RESET* have the same sign.

- **Diffusive:** A subform of unipolar switching, where *RESET* happens below a certain threshold voltage.

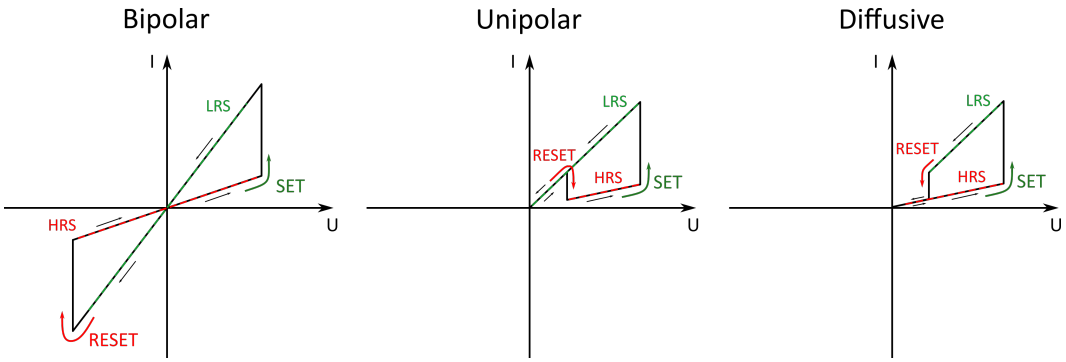

Figure 2.5: *The three switching polarity modes for a binary memristor.*

Devices that show **bipolar switching** have a stable HRS and LRS and the SET and RESET operations occur at opposing polarities. Most commonly bipolar switching devices with a long retention time are considered for non-volatile memory applications, since its state is retained until it is explicitly overwritten[50, 68, 73–75]. The detailed mechanism depends on the type of memristive switching.

In contrast to bipolar switching, **Unipolar switching** SETs and RESETs occur the same voltage polarity (see *Figure 2.5*), where the SET voltage is higher than the RESET voltage[76–78]. The SET mechanism involves the formation of a conductive filament and the RESET an out-diffusion assisted by Joule heating due to the higher current flowing[78, 79]. Similar to bipolar memristors, the HRS and LRS are stable so that this kind of device is also considered for memory applications. The advantage over bipolar memristors is the single voltage polarity, facilitating the external circuitry when integrated in logic arrays[79].

Diffusive switching has been first reported by Wang et *al.*[80] and is a subtype of ECM-based unipolar switching. The filament formed under forward bias is thin enough, i.e. its lifetime is short enough, that it collapses immediately as soon as the bias voltage decreases under a certain threshold voltage. Thus, this kind of switching cannot retain its state at zero voltage making it unsuitable for memory applications. However, diffusive memristive systems have been discussed in the context of their similarities to neural mechanisms like synaptic plasticity and feedback inhibition in feed-forward networks[80, 81].

2.1.2.3 Nanoparticle Switching:

In the context of resistive switching, nanostructured electrodes in an ECM device have been reported as a means to concentrate the electric field and localize the switching sites[82, 83], thus preventing the unlocalized formation of an undefined number of filaments. The same reasoning can be extended to embedded nanoparticles, which have been investigated as an alternative to bulk electrodes, such as in networks of noble metal nanoparticles[84, 85] as well as single or stacks of few nanoparticles[86]. The basal switching mechanism is identical to electrode-based ECM, but the active species forms filaments between the embedded particles, as these mediate the electric field.

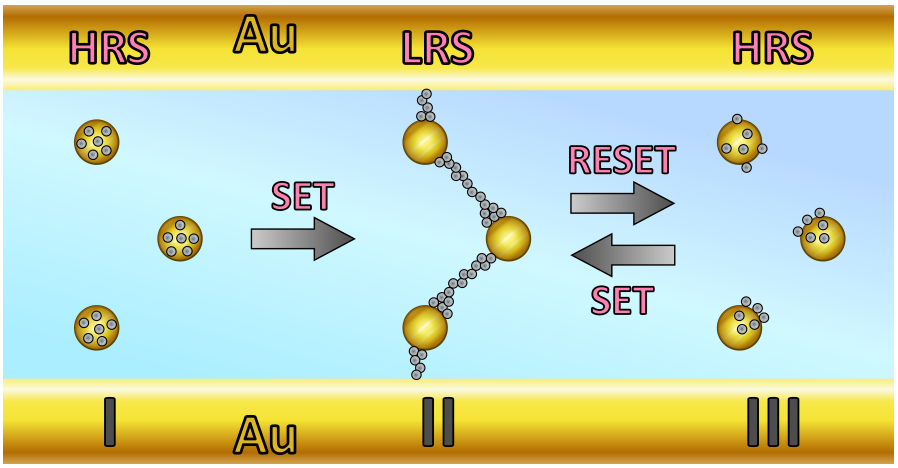

Figure 2.6: *Schematic of resistive switching based on AgAu nanoparticles. I) Initially all Ag is dissolved in the Au particles. II) Applying the SET voltage leads to ECM-type filament formation of the Ag atoms. The gold particles are immobile and do not react. III) During the RESET the filaments collapse and the Ag atoms preferably dissolve into the Au particles again.*

The resistive switching mechanism relevant for this section is based on bimetallic AgAu nanoparticles, which have been reported in [86] and are shown schematically in *I* in *Figure 2.6*. They show diffusive ECM-type switching, where the silver acts as the active, mobile species. In contrast to the silver, the gold portion of the particles is inert and immobile giving it a two-fold function: According to what has been described above, it acts as a field mediator, concentrating the electrical field and localizing the resistive switching. Additionally, it serves as an anchor and reservoir for the silver, limiting the availability of the active species, while attenuating an uncontrolled diffusion of silver atoms through the matrix.

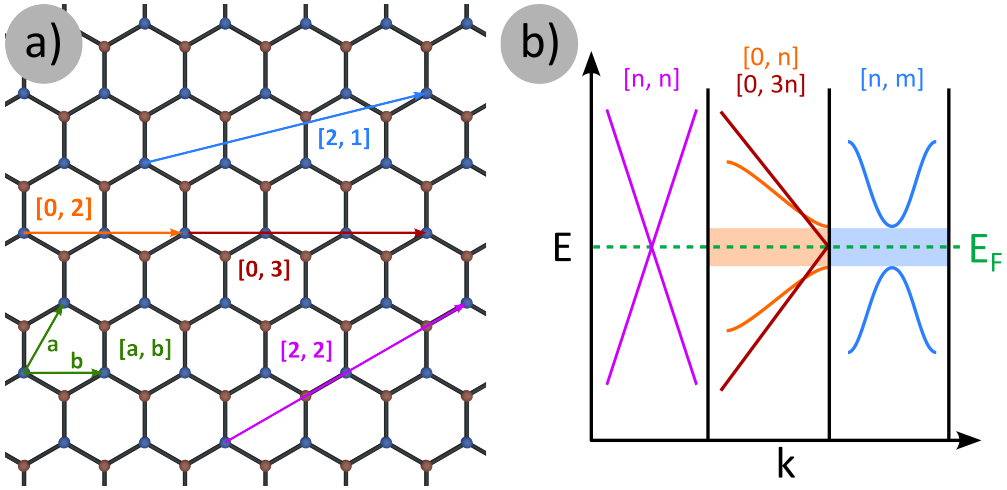

Figure 2.7: *a) Planar schematic of a graphene lattice. The coloured arrows indicate the base vectors as well as the contour vectors for armchair, zigzag and chiral configurations respectively, when rolled up to a CNT. b) Schematic graph of the dispersion of CNTs in the various configurations. It is seen that the armchair and the 3n-zigzag configuration show a singularity in the band diagram, whereas other zigzag as well as chiral configurations yield a band gap[94, 95].*

2.2 Carbon Nanotubes

Already since the 1950s tubes of carbon have been observed[87]. However, they only have been thoroughly investigated after in 1991 Iijima reported on tubular "graphitic carbon needles" with multiple shells which nowadays are well known as multi-walled carbon nanotubes (MWCNTs)[88]. The synthesis of single-walled carbon nanotubes (SWCNTs) followed two years later in 1993[89].
Since 1991 carbon nanotubes (CNTs) have become tremendously popular as a promising material for many different applications due to their remarkable electrical, chemical and mechanical properties[90–93] with over 230,000 publications in the "Web of Science Core Collection" by 2023 (search term "carbon nanotubes").

CNTs can be described as rolled-up graphene sheets, with either one or more concentrical layers, where the orientation of a layer is decisive for its electronic properties.
The orientation of a CNT is defined by a two-dimensional vector $[a, b]$ on a hexagonal plane (see green arrows in *Figure 2.7a*) that describes the direction of a tube's perpendicular contour. which is depicted in *Figure 2.7a*. Several cases are distinguished, which were given dedicated terms[96]:

- If $a = b > 0$ the configuration is called "armchair" (see purple arrow in *Figure 2.7a*).

- If $b > 0$ and $a = 0$ (or vice versa) the configuration is called "zigzag" (see red and orange arrows in *Figure 2.7a*).

- In any other case the configuration is termed "chiral" (see blue arrow in *Figure 2.7a*).

For this work two features of CNTs are of particular interest:

Aspect ratio: A CNT's diameter is generally in the nanometer range. However, their length can differ vastly from less than 1 μm to over 50 cm[97]. Due to their exceptionally high aspect-ratio CNTs can be considered as one-dimensional objects[98], which has an impact on their percolation behaviour in a network configuration (see *section* 2.3).

Electrical conductivity: Graphene and CNTs consist of sp^2-hybridized carbon atoms[95]. Besides the strongly bound electrons in the three σ-bonds, the sp^2-hybridization includes a weak π-bond, i.e. the double bond, which provides mobile electrons, across the whole structure. However, by being "rolled up" CNTs differ from graphene by additional periodic boundary conditions. This leads to different electric behaviour for CNTs depending on how the carbon lattice of the CNT is oriented, due to differing band structures:
Generally, the band structure of CNTs contains a band gap of various size, making it a semiconducting material. However, in an armchair configuration, as well as in a zigzag configuration $[n, 0]$ with $n \ mod \ 3 = 0$, the band structure shows a singularity between valence and conduction band, yielding a band gap of 0 eV (see *Figure 2.7b*). In this case the material behaves like a metal, so it is also referred to as a "semi-metal"[94, 95].
MWCNTs are concentric shells of single tubes, so their collective conductivity is composed of the individual tubes. However, it has been found that the two outmost shells dominate, as the inter-shell conduction occurs by tunneling between overlapping π-orbitals. They show a significantly higher resistance, which is also dependent on the mismatch of lattice orientations[99].
When it comes to networks of CNTs, its conductivity is mostly limited by tunneling contacts between the tubes. Considering networks of MWCNTs they show metallic behaviour predominantly, especially at room temperature, where thermally assisted hopping is facilitated[100].

2.3 The Role of Percolation

The term percolation is used to describe a state of long-range connectivity in a system of statistically distributed elements. Practically, this concept has a high relevance for numerous fields such as the behaviour of liquids in porous media (e.g. [101]).
For this work, the most kindred example is a conductive composite, where filler particles with high conductivity are embedded into an insulating matrix. The filler has to reach or exceed the percolation point in the matrix so that the composite's conductivity is determined by the filler rather than the matrix.

On a formal level, percolation is a theoretical, statistical process where a graph made up of nodes (also called "vertices") and edges (or "bonds") is split into finite clusters by removing nodes or edges with a given probability p or vice-versa by inserting them[102]. All nodes that can be reached from another given node are part of its cluster. And when the graph is considered to be infinite, two states can be defined: Either only finite clusters exist or there is at least one infinite cluster, depending on the occupation probability p. So, there exists a critical value p_c also called percolation threshold[103, 104], for which holds[1]:

- While $p < p_c$ all clusters are finite
- While $p > p_c$ there is at least one infinite cluster

In other words, for a finite network the percolation threshold describes the amount of elements necessary so that it is possible to cross the network from one border to another.

To illustrate the concept, *Figure 2.8* displays a 2D graph with a hexagonal lattice in three different percolation states. It can be imagined as an edge network of electrical conductivities with external terminals at the top and bottom sides. An edge element represents a finite conductivity, whereas a missing element is regarded to have zero conductivity. It becomes clear how important p_c is for this kind of network: On the one hand, below p_c the network will only consist of "finite" clusters, which means - with respect to the finiteness of any real system - that no cluster will span the whole network and thus there will be no continuous connection yielding zero conductivity in total from one terminal to the other. An "infinite" cluster on the other hand, which is present for $p > p_c$, crosses the network completely thus connecting the two terminals with a non-zero conductivity. In addition, simulations conducted by Langley et *al.*[105] revealed that for one-dimensional objects, which CNTs are as described in *section* 2.2, the critical density

[1]Formally, by [102] p_c is defined as the value of occupation probability p below which the probability of the origin to be part of an infinite cluster is zero.

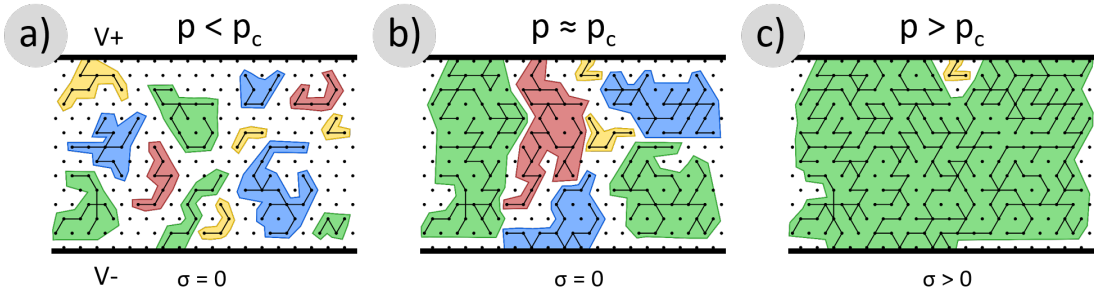

Figure 2.8: *Schematic of a 2D-graph with a hexagonal lattice and only edges as elements representing conductivities. The top and bottom sides are external terminals. The colored areas show separate clusters for increasing percolation states from left to right. a) Below the percolation threshold all clusters are finite so that none of them spans the whole network. b) Near the percolation threshold there are less and larger clusters that are closer to each other and almost span the network. c) Above the percolation threshold the majority of clusters merged into one that makes up most of the network. In this state there will be a non-zero conductivity between the terminals.*

for percolating networks decreases significantly with increasing length; or in other words, the percolation probability increases with increasing length for a given object density.
Properties of a composite, such as the conductivity, vary drastically near the percolation threshold. For the case $p < p_c$ this is reflected in the equation

$$\sigma = \sigma_f * (p_c - p)^{-s} \tag{2.5}$$

where σ is the conductivity of the composite, σ_f is the conductivity of the filler and s is an empiric exponent that has found to be between $s = 1.1$ to 1.3 for a two-dimensional system[106].

While percolation theory, due to its stochastic nature, might not be suitable for precise predictions, it is a valuable tool to describe and understand the behaviour of likewise stochastic physical systems. In the context of this chapter, the aforementioned aspects of percolation theory are used to discuss and justify qualitatively the treatment of the network of carbon nanotubes and the deposition of bi-metallic nanoparticles. Both kinds of network have been considered resistance networks and in both cases the aim was to fabricate a network just below the percolation threshold, i.e. $p \lessapprox p_c$:
The CNT network has been prepared top-down, by creating an overpercolated network with $p > p_c$ and subsequently removing elements by Joule heating (see *section* 3.2.3).

The nanoparticles formed a bottom-up network where elements are inserted via sputtering until the target point is reached (see *section* 3.2.4).

2.4 Fundamentals of Dielectrophoresis

Electrophoresis is an electrokinetic effect that describes the migration of charged particles through a viscous medium due to an applied electrical field. It relates the velocity of a particle v to the applied electrical field strength E by[107]

$$v = \nu_{EP} E \tag{2.6}$$

where the proportionality factor ν_{EP} is called the "electrophoretic mobility" and depends on the properties of the medium as well as the particle:

$$\nu_{EP} = \frac{2\epsilon\zeta}{3\mu} \tag{2.7}$$

Here, ϵ and μ are the permittivity and the viscosity of the medium respectively, whereas ζ is the zeta potential of the particle. For particles with dimensions larger than the Debye-length λ_D, where the electrical field is screened by the double layer ν_{EP} becomes

$$\nu_{EP} = \frac{\epsilon\zeta}{\mu} \tag{2.8}$$

instead.
Now, the term "dielectrophoresis" is used for a related effect, where a non-uniform electrical field E exerts a force on a particle in a medium. The non-uniformity induces a dipole moment in the particle, which results in a charged interface to the medium.
The time-average of the dielectrophoretic force $\langle F_{DEP} \rangle$ on a spherical particle of radius r in a medium with permittivity ϵ_m is given by

$$\langle F_{DEP} \rangle = \pi r^3 \epsilon_m Re[f_{CM}] \nabla E^2 \tag{2.9}$$

where f_{CM} is the Clausius-Mossotti factor which derives from the polarizability of the particle and is

$$f_{CM} = \frac{(\epsilon_p - \epsilon_m) - i\left(\frac{\sigma_p - \sigma_m}{\omega}\right)}{(\epsilon_p + 2\epsilon_m) - i\left(\frac{\sigma_p + 2\sigma_m}{\omega}\right)} \tag{2.10}$$

where ω is the frequency, σ is the conductivity and the indices m and p indicate medium and particle respectively.
For small frequencies f_{CM} becomes

$$f_{CM} \rightarrow \frac{\sigma_p - \sigma_m}{\sigma_p + 2\sigma_m} \tag{2.11}$$

and therefore solely dependent on the conductivities.
In contrast to electrophoresis *Equation* (2.9) shows that a non-uniform E-field, indicated by the gradient ∇E^2, can be used either to migrate even uncharged particles due to the induced polarization or add an additional force based on the properties of particle and medium. The electrokinetic effect of dielectrophoresis is commonly used in biology for separating or relocating cells, DNA and other biological particles as well as for orienting or arranging particles such as CNTs[108–113]. In *Chapter* 4 it will be utilized to rearrange dielectric ZnO particles in a liquid around a grid of electrodes.

2.5 Sensing with Metal Oxides

This section is attributed to ZnO and its properties and mechanisms as a sensing material, which is of relevance for *Chapter* 4 as well as *Chapter* 5.

2.5.1 Zinc oxide

ZnO is a II-VI semiconducting metal oxide with a bandgap of $E_g \approx 3.37$ eV. Under ambient conditions, it's crystal structure is the wurtzite structure, where hexagonal lattices of oxygen and zinc are interpenetrating into each other leading to an alternating stack of Zn^{2+} and O^{2-}[114, 115], as depicted in *Figure 2.9a.*

ZnO has been discussed to be a n-type semiconductor due to impurities acting as donors when substituting Zn as well as O. This holds even for H from an interstitial position[116]. The interactions with photons and gases give rise to the functional properties of ZnO, as will be described in detail in *section* 2.5.2.

Tetrapodal ZnO: ZnO nanoparticles have been synthesized in various morphologies and sizes, such as spheres, wires, flower-like structures, porous plates and "sea-urchins"[117–120].
A particularly interesting morphology is the so-called "tetrapodal ZnO". It consists of a central nucleus, from where four arms stretch out with an angle of $\approx 110°$[121] so that its form is close to a perfect tetrahedron (see *Figure 2.9b*).

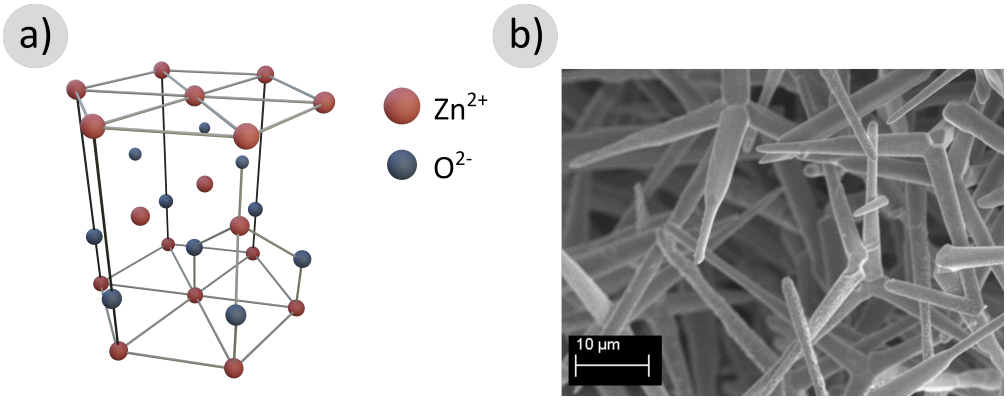

Figure 2.9: *a) 3D-model wurzite crystal structure of ZnO. b) SEM micrograph of tetrapodal ZnO.*

Due to its bulky shape bundles of tetrapodal ZnO show a large free volume and thus an accordingly large surface area. This feature is particularly useful for sensor applications, since the active surface is a decisive factor for the sensor performance. The free volume also allows for a facile incorporation of decorative or interfacing species, as will be shown in *section* 5.2 for a t-ZnO/CNT interface.

2.5.2 Sensing mechanisms of metal oxide semiconductors

This section will cover the mechanisms that make metal oxides suitable as a functional material for sensor applications. To keep it concise, it will be limited to ZnO as a model system and the two main stimuli relevant for this work, i.e. photons and surrounding gases.
The essential property of ZnO for both mechanisms is the way it interacts with ambient gases, most prominently oxygen, which has been readily described in [122]: Oxygen vacancies in the ZnO act as shallow donors near the conduction band. Ambient O_2 molecules can chemically adsorb to the surface of the ZnO by catching electrons from the donor states:

$$O_2 + 2e^- \rightarrow 2O^-(ad) \tag{2.12}$$

In the surface-near region this process bends the band structure upwards and depletes it from its electrons, thus forming an electron depletion layer (EDL), whose thickness depends on the amount of adsorbed oxygen. The EDL shows a decreased concentration of charge carriers and consequently a higher resistance, so that it decreases the conductive cross-section of the material.
This mechanism also has an impact on the interface to contacting materials, since a Schottky barrier at the interface depends on the adsorbed oxygen determining the conductance across it[123].

The following two paragraphs will elucidate the interactions of ZnO and the adsorbed oxygen with photons and gas molecules respectively.

Photons: As described above, ZnO is a direct wide band gap semiconductor with a band gap of ≈ 3.37 eV. Thus it is able to absorb light with a wavelength of $\lesssim 368$ nm (UV-light) by generating electron-hole-pairs. Additionally, defect states, e.g. by oxygen vacancies, expand the absorption capabilities to the visible spectrum[124].
The charge carriers generated migrate through the bulk material and are separated when reaching the electrical field of the space-charge region in the EDL, i.e. the positively charged holes drift towards the surface. If holes reach the surface, they interact with the adsorbed oxygen, leading to a desorption and consequential release of the bound electrons[125]:

$$2O^{-}(ad) + h^{+} \rightarrow O_2 \tag{2.13}$$

This desorption shrinks the high-resistance EDL, increasing the conducting cross-section of the bulk.

Gas molecules: The sensing mechanism of ZnO for gases also revolves around the adsorbed oxygen on the bulk surface and the resulting EDL.
Organic compounds such as acetone or ethanol are proposed to undergo chemical reactions with the oxygen adsorbed on the ZnO surface[122, 126, 127]. Oxygen is removed, thus releasing electrons and shrinking the EDL. The same mechanism is reported for H_2S, albeit discussed as non-exhaustive[122]. A similar reaction has been proposed for hydrogen environments by creating H_2O[121].

2.6 Features of Neural Assemblies

This section covers mechanisms shown by biological neural networks, that are essential to their functioning and are emulated by the material systems presented in *Chapter* 4.

2.6.1 Spike-Timing Dependent Plasticity

The term "Spike-Timing Dependent Plasticity" (STDP) describes a collection of electrical mechanisms in biological neural assemblies that are correlated to Hebbian learning and memory capabilities[128, 129]. It states that a synaptic connection between two neurons is modified based on their relative neural spiking behaviour, giving rise to the two important principles Long-Term Potentiation (LTP) and

Long-Term Depression (LTD). LTP occurs when the pre-synaptic neuron spikes in a time-window of tens of *ms* before the post-synaptic one. In this case the synaptic connection is potentiated, i.e. it increases in transmission efficiency. Similarly, LTD occurs when the pre-synaptic neuron fires shortly after the post-synaptic one, which leads to a weakening of the connection.
LTP and LTD are crucial mechanisms for learning and memorizing, as well as forgetting, as these cause the long-lasting structural changes - i.e. the plasticity - in a neural circuit that are considered basal for encoding behaviour or storing information. Since neural activity represents externally perceived events via its spiking patterns, its information can be considered to be encoded in the effect of the event signal's transmission on the neural structure[130].

2.6.2 Synchronization of Neural Oscillators

The electrical oscillations of action potentials and the spatio-temporal firing patterns in neurons are another basal mechanism for the processing and coordination of neural activity. A central role plays the phase synchronization state of neural oscillators, in both local as well as long-range integration. The interplay of short and long range synchrony with low and high frequency oscillations has been found to be crucial for environmental cognition, higher brain functions and coordinated responses e.g. for sensory-motor processes or preparation for an anticipated task[131–133].
Oscillating components can be found in many technical as well as natural systems. A common characteristic among them is the phenomenon of mutual phase synchronization, when the oscillators are coupled. The universality of this feature led to thorough mathematical descriptions[134, 135].

For this work, in *Chapter* 4 relaxation-type oscillators have been used to emulate brain-like dynamics by mimicking an oscillatory ensemble. The technical details of the oscillators are given in *Appendix* A.3. It is showcased how guided redox-wiring is capable of an activity-driven phase (de-)synchronization via the oscillators' coupling, as described in *section* 4.1.4.3.

2.7 Additive Manufacturing

The majority of this section is excerpted from [136].

Traditional manufacturing of parts is mostly subtractive e.g. milling, drilling, etc., where material is removed from the part until it is shaped as intended. This creates a substantial deal of waste while it becomes more and more difficult and

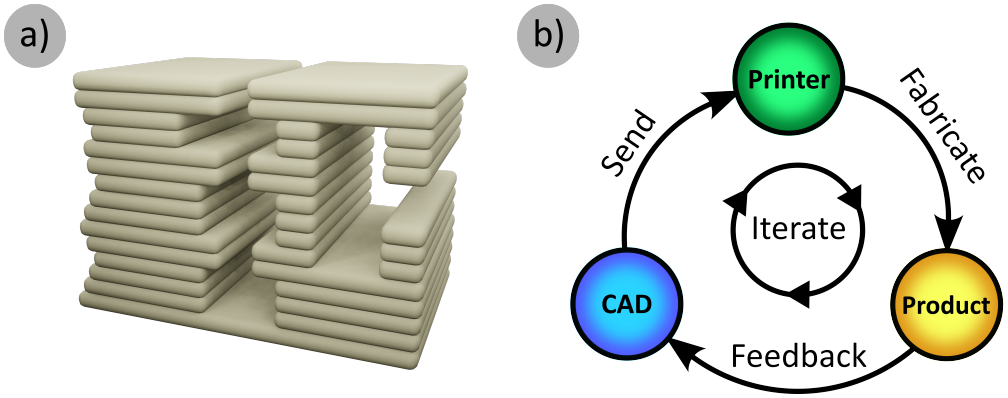

Figure 2.10: *a) 3D model illustrating how layers of material are stacked to form three-dimensional objects. This bottom-up approach allows undercuts, cavities and other features that are difficult or impossible to achieve by conventional machining. b) Workflow of a design iteration cycle. The direct connection from CAD to the printer allows rapid prototyping.*

thus expensive to fabricate a particular part the more complex its shape is.

In contrast to this top-down approach, additive manufacturing works "bottom-up" by assembling the final part out of small fractions. The most common way is by stacking thin layers of material on top of each other to create three-dimensional objects (see *Figure 2.10a*). For the deposition of material for each layer there are several different approaches available, depending on the matrix material and specifications of the part such as the minimum feature size. Processes like fused deposition modelling (FDM) melt a thermoplastic filament and extrude it through a nozzle to deposit the material, while stereolithography (SLA) is based on the photo-polymerization of thin layers of liquid resin. Metal parts can be produced by selective laser sintering (SLS) or the conceptually similar selective laser melting (SLM), which heat up a metal powder to sinter or melt the grains together[137, 138]. Besides the material deposition, AM technologies use robotic elements similar to computerized numerical control (CNC) machines, where the movement of machine components is controlled by computers. This facilitates completely automated production, with design and fabrication as directly subsequent steps. The designer is given a huge freedom - depending on the manufacturing technique - in terms of shape and materials. Furthermore, the workflow allows for quick iteration cycles, as shown in *Figure 2.10b*, which led to additive manufacturing being termed as "rapid prototyping".

Direct Ink Writing Direct Ink Writing (DIW) is a subtype of AM, where an ink composed of a carrier fluid and colloidal particles with moderate to high filler content is extruded onto a substrate through a robotic nozzle. The carrier fluid consists of a volatile solvent and in some cases a polymeric binder. After extrusion

the solvent evaporates and the ink solidifies. While this technology already has been around for many years in the form of inkjet printers for digital images it also got more recent attention as means for AM by depositing ceramic particles via the ink[139–142]. Furthermore, DIW allows to print *any* materials in powder form, particularly materials that are not suitable for other additive manufacturing methods or that have complex particle morphologies. This also includes functional particles like tetrapodal ZnO (cf. *section* 2.5.1), which expands the capabilities of AM from purely structural parts towards functional or composite components.
However, the rheological properties of the ink are crucial for the reliable fabrication with DIW. The ink must remain homogeneous and flow evenly to avoid defects or aberrations in the print. Colloidal suspension inks are based on a carrier fluid and one or more species of suspended micro- and/or nanoparticles. A polymeric binder can be added to the solvent to control the inks viscosity and thus its rheology. If the particles are too large to stay suspended in the pure solvent, a polymeric binder is added to increase the viscosity preventing the particles from sedimenting. Furthermore, complex shaped particles like t-ZnO form highly porous, tangled agglomerates. In this case, a high viscosity is necessary to exert the shear forces required to move the particles, otherwise the liquid would flow through the pores and separate from them.

Table 2.1: *Selection of microparticle species used in inks during this work and possible applications as printed components.*

Ink	**Application**
Metal oxides (e.g. ZnO)	UV-/gas-sensor
Carbon nanotubes	Wiring
Fe	Magnet, wiring, oxidation to MO
Zn, Cu	Wiring, oxidation to MO
ZrO_2, SiO_2	Insulator, structural support

The carrier fluid commonly solidifies either by evaporation of the solvent, e.g. for the systems H_2O/PEG or EtOH/PVB or by a chemical reaction e.g. for silicones. Once solid it can either persist as a structural matrix for the particles or be removed by thermal or chemical decomposition. Especially for functional micro- or nanoparticles it is desired to remove the binder. Doing so, creates interfaces to other external species, like gases or light, or yields percolating, dense structures. This densification lets the printed structure approximate the properties of the bulk material e.g. in terms of electrical conductivity. In *Table 2.1* a number of exemplary species of microparticles are given, with possible applications for the respective inks. However, DIW as a method enables the creation of any mixture between kinds of particles allowing to achieve any additional benefits of material

composites or resulting material interfaces. As an example in [143] copper and iron particles have been mixed into one ink to obtain CuO/Fe_2O_3 interfaces for improved sensor performance.

2.8 Methodology

This section will cover the background about the most relevant and more involved techniques, that have been deployed during the work for this chapter. Each method will be discussed with respect to its meaning for the experiments and results presented in this work.

2.8.1 Scanning Electron Microscopy

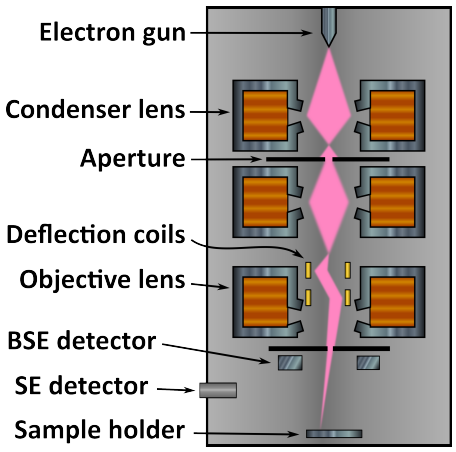

Figure 2.11: *Cross-sectional schematic of a SEM. The pink area is the electron beam.*

Scanning electron microscopy (SEM) is a prevalent method for the depiction of micro- and nanostructures. The sample is illuminated with an electron beam and the interactions of the incoming electrons with the sample material yields different kinds of signals, such as secondary electrons, that are detected and processed into an image. It also allows to detect X-rays emitted from the sample for a chemical analysis via energy-dispersive X-ray spectroscopy (EDX). A thorough treatment of the SEM can be found elsewhere (e.g. [144]).

In this work the SEM has been deployed to investigate the morphology of the material systems on the micro- and nanoscale: For *Chapter* 3 it was a valuable tool for verifying the sparseness of the superimposed CNT and nanoparticle networks, whereas in *Chapter* 5 it was used to display the structure of the fabricated devices and their embedding into the polymer matrix.
Additionally, it has been used to record the EDX measurements in *Chapter* 4.

All SEM images shown in this work have been recorded with a Zeiss Ultra 55 Plus with an in-lens detector at 5 kV acceleration voltage, 30 μm aperture and a working distance of 4-5 mm.
EDX measurements have been recorded with a ULTRIM MAX 65 detector at 10 kV acceleration voltage, where the aperture has been set to 120 μm.

2.8.2 Spin Coating

Spin coating is a facile technique for depositing viscous fluids on flat surfaces. The substrate is placed on a disc where it is fixed, commonly via vacuum, and the disc is rotated with a given angular velocity ω (see *Figure 2.12*)[145, 146]. The liquid is placed on top of the substrate, where by centrifugal forces it is sheared resulting in a liquid flow to the edges of the disk. Material is propelled off the disk until adhesive and shearing forces are balanced resulting in a mostly uniform film of defined thickness, which is essentially dependent on angular velocity, liquid viscosity and liquid-substrate interaction as well as potential solute concentrations[146].
In cases where the liquid is a solution or dispersion with a volatile solvent, evaporation plays a major role as well. During spinning the loss of liquid is first dominated by flow off the disk and transitions into being dominated by evaporation.
Generally, the higher the angular velocity as well as the evaporation rate, the thinner the resulting film will be[146].

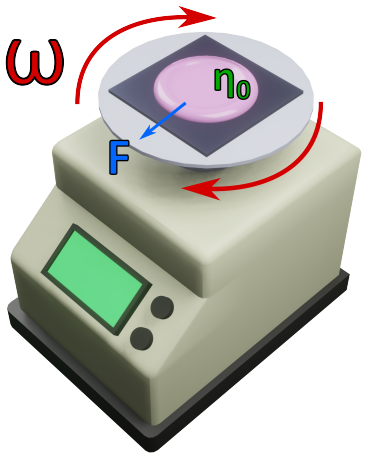

Figure 2.12: *3D-schematic of a spin coating process on a silicon substrate. The disk rotates with angular velocity ω, exerting a force F on the liquid. This results in a liquid flow by shearing depending on the liquids viscosity η_0. The flow distributes the liquid homogeneously on the substrate.*

In this work, the technique has been used to deposit CNTs dispersed in ethanol on a substrate (see *section* 3.2). Other simple deposition techniques like spray coating or drop coating showed major roadblocks like the "coffee-stain" effect[147] or lacking control of process parameters like the amount deposited or the film homogeneity.
Spin coating allows a precise control of the resulting film by its angular velocity, CNT concentration and number of droplet applications, whereas other parameters like spinning time or droplet volume have been reported to have negligible impact on the resulting film[146], reducing the methods susceptibility to errors and thus improving the reproducibility.

2.8.3 Gas-aggregation Source Sputtering

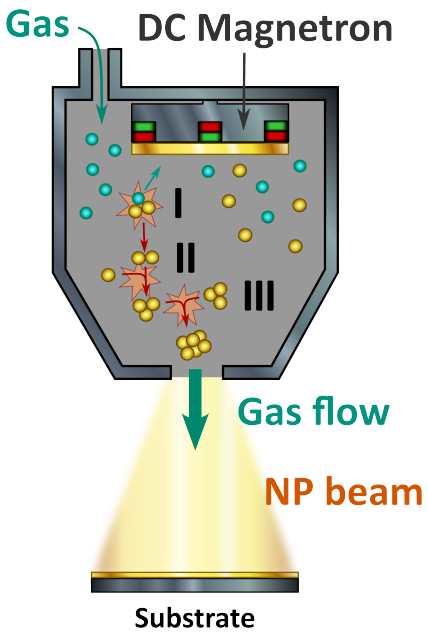

Figure 2.13: *Schematic of a gas-aggregation source chamber and the processes for the formation of nano clusters. I) Cluster nucleation by three-body collision. II) Cluster growth by atom attachment. III) Cluster coagulation.*

Sputtering in general is a physical deposition technique used to deposit thin films of specific materials from the gas phase onto a substrate. The material to form the film originates from a bulk target, where ionized gas from a plasma is accelerated towards it to desorb the target atoms. The process is a very common deposition technique as it is well controllable in terms of material, purity and layer thickness[148].
Besides thin films the deposition of particles clusters from the gas phase can be achieved by various methods such as co-sputtering[149] or co-evaporation[150]. In 1992 Haberland et al. reported on a gas-aggregation source, which was designed to generate metal clusters from two targets in a separate Ar gas chamber[151]. By maintaining a higher gas pressure (0.1 - 1 mbar) in the GAS than in the main deposition chamber, the gas including the clusters flows through an orifice, creating a particle beam towards the deposition substrate.
The metal clusters are formed by up to three steps, which are shown in *Figure 2.13*[152]:

I. Cluster nucleation occurs by a three-body collision of two metal atoms with a gas atom. The gas atom takes up energy so that the two metal atoms form a stable dimer.

II. Metal clusters grow by attachment of atoms from the gas phase.

III. Clusters might coagulate forming larger particles.

GAS sputtering allows great control over composition and size distribution of the deposited particles[152, 153]. Additionally, in [153] Vahl et *al.* reported on how to achieve varying compositions of bimetallic nanoparticles from a single composite target, where Au wires have been embedded into a Ag bulk target.

In this work, a GAS with a composite AgAu target has been used to deposit a film of sparse AgAu nanoparticles, which were acting as resistive switching sites in a network of carbon nanotubes (cf. *Figure 3.1*). Other fabrication routes, e.g. wet chemical synthesis of AgAu nanoparticles[154], have not been feasible as the liquid would have a detrimental impact on the deposited network of carbon nanotubes on the substrate.

Chapter 3

A Horizontal Memristor with Short-Term Memory

This chapter addresses two challenges that are related to the component as well as the network space mentioned in *Chapter* 1:
On the one hand, the establishment of a facile workflow to obtain a lateral sparse conductive network as a starting point towards the integration of functional parts, such as resistive switching sites, while avoiding sophisticated fabrication methods. On the other hand, the fabrication of a memristive device with a retention-time in the time scale of several seconds to be able to act as a short-term device component.
It covers the development, fabrication, characterization and discussion of a new memristive device, which is based on a sparse network of CNTs with implanted bimetallic nanoparticles as the active switching sites. The resistive switching shows a hybrid behaviour between diffusive and bipolar with a retention time in the second regime that has found to be adjustable by the voltage pulse width. In the context of the component space, this memristor concept is conceivable as a short-term memory element due to its retention properties, while it also borders to the network space by its lateral network design.
The discussion of this chapter's experimental work is split into two successive sections: The fabrication route focused on the realization of a sparse CNT network by overcoming the issues accompanying the properties of CNTs. And consecutively the electrical characterization of the resistive switching discussing the origin and peculiarities of the ECM-type switching behaviour.
The main portion of the experiments and results presented in this chapter are excerpted from the following publication to which the reader is also referred:

[155]: **M.-I. Terasa**, P. Holtz, N. Carstens, S. Kaps, F. Faupel, A. Vahl, R. Adelung, 2022, "Sparse CNT networks with implanted AgAu nanoparticles: A novel memristor with short-term memory bordering between diffusive and bipolar switching", *PLoS ONE*, 17(3) e0264846, DOI: 10.1371/journal.pone.0264846

3.1 The Concept of the "Horizontal Memristor"

In *section* 2.1.1 the concept of the memristor has been introduced in general. Now, at this point the term "Horizontal Memristor" and the reasoning behind it will be clarified.
While there exists a large number of different memristor concepts the majority of devices is based on stacks of thin films with a thickness of just a few *nm*[50, 73, 156, 157]. These nanoscaled distances - resulting in high electrical field strengths for an applied voltage - are required for the processes of memristive switching phenomena to occur, e.g. ionization and ion migration. Details on memristive switching mechanisms are found in *section* 2.1.2.
Established thin film technology allows for precise control of layer thickness, composition and purity, so that a fabrication in this configuration stands to reason.
Nontheless, the vertical orientation of such devices has the drawback, that the active layers are always hidden between the electrodes and thus are inaccessible from the outside. Designing a memristive component in a lateral geometry instead makes the active sites available for external signals. This includes investigative ones from imaging methods or surface sensitive analysis, e.g. SEM or XPS, but also stimuli like photons, e.g. for surface plasmon resonance[158–160] or chemical species, which makes the integration of sensor features into memristive systems conceivable. However, obtaining the necessary nanoscaled dimensions *laterally* requires time-consuming and sophisticated methods, e.g. focused ion beam deposition (FIB) or electron beam lithography[161, 162].
In contrast, the "horizontal memristor" described in this chapter is prepared with a new fabrication workflow without the need for sophisticated methods that utilizes a hierarchy of three length scales to reach the nanometer scale laterally as displayed in *Figure 3.1*:
On the "electrode level" the external signal is applied to the electrodes that have a gap in the range of micrometers. Between the electrodes on the "network level" a *sparse* network of CNTs is deposited providing gaps between individual tubes in the single-digit- to sub-micrometer range. Finally, a sparsely deposited layer of AgAu nanoparticles makes up the "nanoparticle level". The nanoparticles are deposited to a density below the percolation threshold, so that they exhibit gaps between them in the lower nanometer range, which are suitable for resistive switching phenomena.
When compared to a vertically layered stack, where the active sites, i.e. the nanoparticles in this case, would be sandwiched between the electrodes, the crucial role of the CNTs at the additional "network level" becomes clear: The network mediates the electrical signal from the macroscopic "electrode level" to the nanoscopic "nanoparticle level". And in addition, the deposition of CNTs is highly feasible and scalable without the need for sophisticated techniques or a clean-room environment. The detailed fabrication route will be discussed in *section* 3.2.

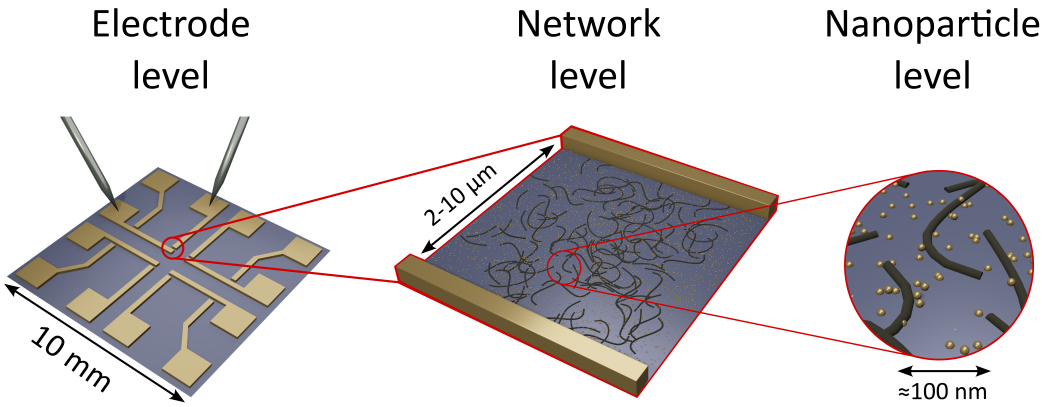

Figure 3.1: *Schematic image showing the sequential usage of three length scales: The transition is achieved from the macroscopic "electrode level" over an intermediate "network level" to the nanoscopic "nanoparticle level", where the resistive switching occurs.*

The AgAu nanoparticles act as the resistive switching sites based on the mechanism reported by Vahl et *al.*[86], which will be treated in detail in *section* 2.1.2.3.

3.2 The Fabrication Route

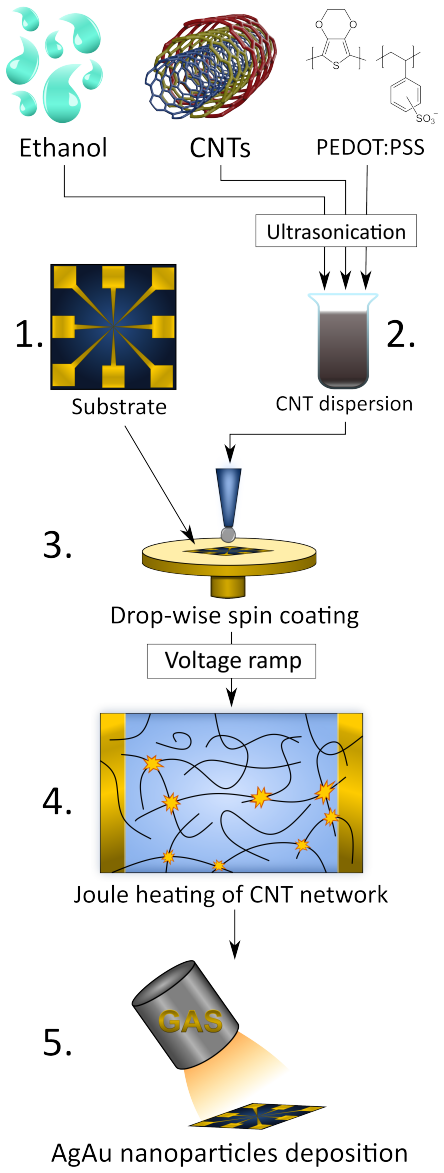

Figure 3.2: *Schematic of the workflow for the fabrication of CNT/AgAu networks. GAS = Gas aggregation source.*

The preparation of samples posed considerable challenges and thus the development of a reliable fabrication route was a notable part of the work this chapter discusses. All samples were produced by following the same general workflow, consisting of the following steps, which are also schematically depicted in *Figure 3.2*:

1. Preparation of substrate (see *section* 3.2.1)
2. Preparation of CNT dispersion by high-power ultrasonication (see *section* 3.2.2)
3. Drop-wise spin coating of CNT dispersion on substrate (cf. *section* 2.8.2)
4. Joule heating of deposited CNTs by applying a voltage ramp (see *section* 3.2.3)
5. Sputter deposition of AgAu nanoparticles (cf. *section* 2.8.3)

In the following, all steps will be described and discussed in detail. A special emphasis is put on the CNT dispersion, which has been custom-made to overcome the problems of a commercial stock solution.
Samples with deposited CNT and AgAu nanoparticle networks will also be referred to as CNT/AgAu networks.

3.2.1 Substrates

The substrates for the CNT/AgAu networks have to provide metal contacts with a spacing in the micrometer range with metal pads that allow for a connection to an external measurement setup. Three different contact designs have been deployed, which are shown in *Figure 3.3* and labelled S1, S2 and S3 respectively.
All substrates used in this work were produced from commercially available thermally oxidized p-type silicon wafers. Gold contacts have been deposited by standard UV-lithography with a Süss Microtech MA6/BA6 mask aligner, followed by a sputtering and lift-off process. The sputter process was a DC magnetron sputter deposition of 10 nm Cr acting as an adhesive layer and 200 nm Au as the contact layer. The lift-off has been performed in an ultrasonicated acetone bath held at 40 °C. After the lift-off the wafer has been cleaned by subsequent rinsing with isopropanol and deionized water and dried. Finally, the wafer has been cut into 10 x 10 mm or 11 x 11 mm pieces with a DAD3350 automated dicing saw. All steps have been performed in a clean-room environment.

3.2.2 CNT Dispersion

In the scope of this work a facile method for obtaining nanoscaled gaps with a sparse network of CNTs has been developed. As mentioned in *section* 3.1 the CNT network is crucial for the mediation between the "electrode level" and the "nanoparticle level". In order to fulfil this function, the CNT network has to meet certain requirements:

- The network must reach to all relevant electrodes to establish electrical contact.
- The CNTs must be finely dispersed when deposited. There must not be agglomerations of CNTs short-circuiting the electrodes, as those cannot be removed by Joule heating.
- The network must be around the percolation point, so that the average distance between CNTs is in the nanometer range. If the density of CNTs is too low, the distance between them becomes too large. If the density is too high, there will be too many short-circuiting paths and the CNTs will be prone to agglomeration.
- The CNTs must not be heavily coated with surfactants or other additives, as those inhibit the Joule-heating step.

The fabrication route for the networks start with the custom-made CNT dispersion, which has been prepared by mixing the following ingredients:

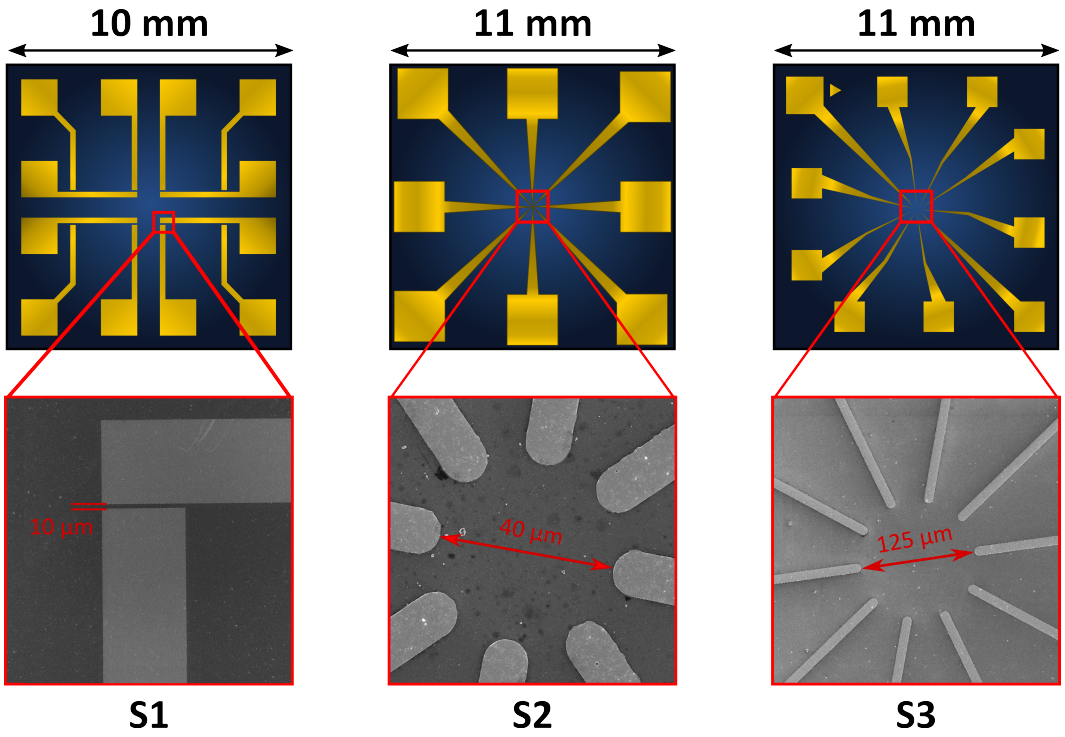

Figure 3.3: *Schematics of the three deployed chip designs and SEM micrographs of the electrode gaps.* ***S1:*** *Flat gaps, eight in total at each chip, four with a nominal spacing of 2, 4, 6, 8 µm respectively and four gaps with a nominal spacing of 10 µm.* ***S2:*** *Eight radially arranged contacts around a circle with a diameter of 40 µm. The distance between directly adjacent contacts is ≈9 µm.* ***S3:*** *Ten radially arranged contacts around a circle with a diameter of 125 µm. The distance between directly adjacent contacts is ≈40 µm.*

- Pristine CNTs as dry powder. In this form the CNTs are not coated with any additives initially.
- Ethanol as a fast evaporating solvent, facilitating a quick sequential application of dispersion droplets during spin coating.
- PEDOT:PSS as an additive keeping the CNTs finely dispersed. In contrast to using a commercial stock solution, the concentration of this additive could be controlled precisely.

The CNT dispersions have been fabricated by mixing 10 g of ethanol (99.7% purity, provided by Carl Roth) with 40 µg pristine MWCNTs (Baytubes C150P) and 1 µl of 1.3wt% aqueous solution of PEDOT:PSS (Ossila PH1000).
Using pristine CNTs already fulfils the requirement that they must not be coated initially with additives. However, the powder consists of large, dense bundles of

CNTs, so to obtain finely dispersed CNTs, the bundles are broken up by high-power ultrasonication performed with a Sonics Vibra-Cell VC 505 with 500 W at 70% amplitude. The sonication has been performed for 15 minutes in total with cycles of 3 s pulsing and 3 s pause. Since the sonication process introduces a large amount of heat the tube containing the dispersion has been kept in a water bath cooled with a Peltier element to attenuate solvent loss.
After the bundles have been broken up, the PEDOT:PSS acts as a surfactant keeping the CNTs dispersed, though without impeding the Joule heating step, as will be shown in *section* 3.2.3.

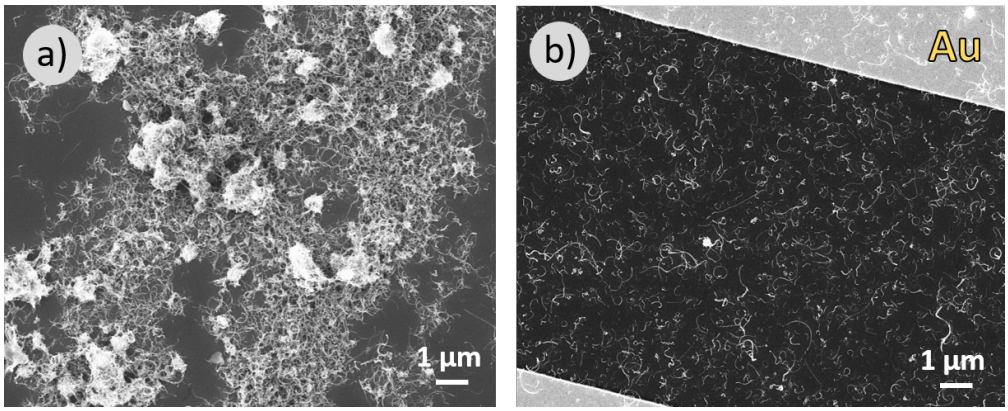

Figure 3.4: *a) SEM micrograph of a large particle of agglomerated CNTs. b) SEM micrograph of sparsely deposited CNTs. The bright spot in the centre is a small agglomerate. However, due to its size it does not impede the fabrication procedure.*

The SEM micrographs in *Figure 3.4* show a comparison of deposited CNTs from a dispersion without (*Figure 3.4a*) and with (*Figure 3.4b*) PEDOT:PSS, demonstrating its function for achieving a sparse and disperse CNT distribution.

The deposition of the dispersion on the substrates has been performed by spin coating (Spin-coater model: Laurell WS-650MZ-23NPPB), which is a facile, scalable and well controllable process (cf. *section* 2.8.2). The CNTs have been dispersed in ethanol as a fast-evaporating solvent to facilitate a sequential application of droplets. The dispersion has been dropped onto the substrate during a constant rotation at 1500 rpm, where each drop has been applied after the complete evaporation of the solvent of the previous one. Following this procedure the density of deposited CNTs can be controlled by the amount of dispersion that is dropped onto the substrate in total.
In this work each substrate has been coated with 350 μl of dispersion, dropped on with an Eppendorf pipette in steps of 50 μl, where each drop had a volume of $\approx 8\ \mu l$.

3.2.3 Joule Heating

During the Joule heating step, a voltage ramp was applied via a *Keithley 2400* Source Measure Unit (SMU) to the deposited CNT network to remove any existing conduction pathway through the CNT network from one electrode to the other. An example for such a voltage ramp is shown in *Figure 3.5a*. Considering an

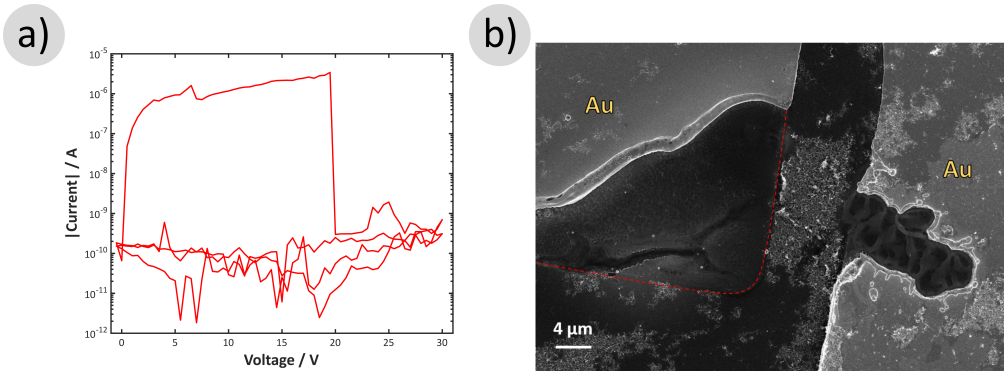

Figure 3.5: *a) Characteristic current-voltage measurement of a Joule heating process. The current drops to the substrate determined resistance at a moderate voltage of 19.5 V. The smaller drop at 6.5 V can be attributed to a single weak spot in the CNT network or the electrode. b) SEM micrograph of a gap with a dense agglomerate of CNTs, where a voltage ramp of up to 80 V has been applied to the electrodes. The gold contacts have melted, while the CNT bundle stayed intact. The red dashed line indicates the original shape of the lefthand gold electrode.*

intersection between two single CNTs, a sufficient voltage drop heats up the contact point sufficiently to destroy the junction and thus the electrical connection between them. This will apply to all intersections that are electrically connected to the electrodes, which will ensure that there is no conductive pathway remaining and the voltage will drop over the gaps in the network. In the current readouts during the Joule heating step a sudden drop in current indicates this point as seen in *Figure 3.5a*

As mentioned above in *section* 3.2.2 this procedure step is prone to failing if the deposited CNT network does not meet the criteria of consisting of finely disperse CNTs without heavy surfactant coating. Dense agglomerates of CNTs might bridge the electrodes and due to the large amount of CNTs present, no applied voltage does suffice to burn the contact points without damaging the substrate. *Figure 3.5b* shows how a large CNT bundle led to a melting of the gold electrodes.

On the other hand, a heavy coating of CNTs with surfactants, which is commonly the case for commercially available aqueous stock solutions, creates an insulating layer between two intersecting CNTs. This interface, due to its resistance, prevents the intersection to burn, since the main portion of the voltage drops over the

insulator. Thus, no voltage compatible with the substrate would be applicable to remove existing pathways.
Current readouts during the voltage ramp have been recorded across three cycles to assure a substrate determined resistance, as displayed in *Figure 3.5a*: During the first cycle the current drops into the *pA* regime, which is attributable to the substrate resistance, and stays in this regime for the remaining subsequent cycles.

3.2.4 Nanoparticle Deposition

The AgAu nanoparticles embedded into the sparse CNT network are the component responsible for the resistive switching phenomena. The Ag is acting as the electrochemically active element, forming the conductive filament, while the Au is a stable anchor (cf. *Figure 2.6*). Additionally, the Au content allows to limit the availability of Ag, while keeping the capability of forming an underpercolating conductive network.

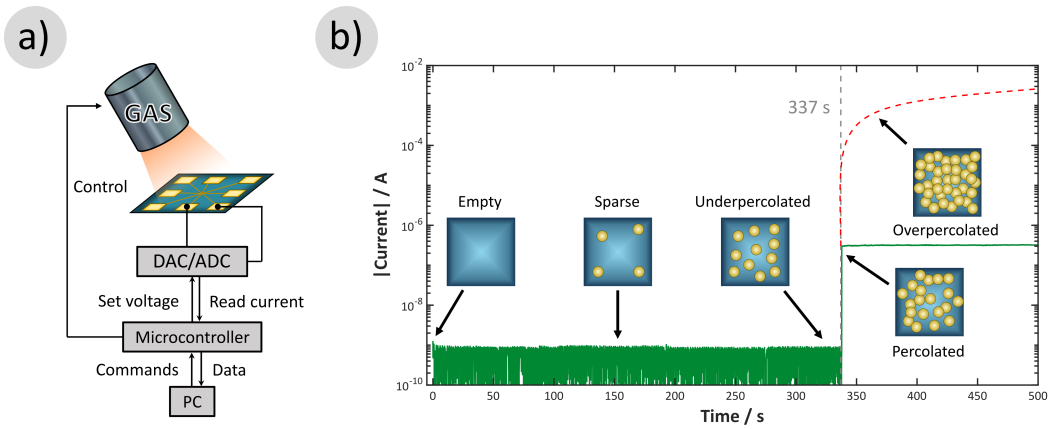

Figure 3.6: *a) Flow chart of the in-operando percolation measurement setup for the sputter deposition chamber. b) Time-resolved percolation measurement across adjacent electrodes of the S2 chip design, at a voltage of 3 V. After the current jumped into the µA-regime, the deposition has been interrupted by closing the shutter. The red dashed line indicates a typical course for the current if the deposition would have continued.*

The deposition of AgAu nanoparticles is achieved by a sputter process with a GAS as described in *section* 2.8.3. An AgAu composite target (as described in [153]) has been attached to the DC magnetron source. This deposition method enables control over particle composition and density, without affecting the deposited CNT network as it would be the case if using a wet synthesis route.
Ar has been used as process gas with a flow of 50 sccm and the magnetron power has been set to 50 W. A computer controlled shutter can be closed to interrupt

the beam during the deposition. This shutter has been kept closed for the first 30 s of each process to ensure a stable deposition rate before exposing the sample to the particle beam.
Similar to the CNT network, the network of AgAu NP must be sparse, so that no short-circuit occurs and the particles are able to form conductive filaments. However, in order to show resistive switching the particles also have to be dense enough, so that the distance between particles is in the lower nanometer range. Thus, the NP film has to stay just below the percolation point, where the average distance between particles is as low as possible while avoiding a conductive path between the electrodes.
The percolation state during deposition has been monitored by an *in-operando* current measurement setup, which is schematically depicted in *Figure 3.6a*.
In *Figure 3.6b* a time-resolved current measurement during deposition is shown for adjacent electrodes of a sample with the *S2* design. As soon as the current jumped into the μA-regime, the shutter has been closed stopping the deposition. This timestamp has been taken as the percolation point for the NP film, which has been found to be 337 s. Thus, subsequent deposition times have been set to 330 s to obtain NP densities just below the percolation.

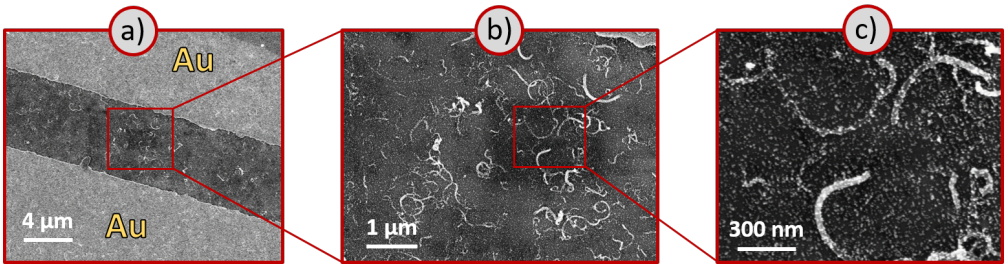

Figure 3.7: *SEM micrographs of a S1 sample with deposited CNT network and AgAu nanoparticles displaying three different features at three different length scales. a) Electrode gap with spacing of 6 µm. b) Sparse CNT network inside the electrode gap. c) Implanted AgAu NP. The nanoparticles in the nanoscaled gaps between CNTs are the active sites for resistive switching.*

To wrap up this section *Figure 3.7* shows a sequence of SEM micrographs depicting a sample fabricated by the presented workflow. It is verified that the hierarchy of length scales that has been motivated in *section* 3.1 could be achieved. A thorough electrical characterization of the samples is presented in the next section.

3.3 Electrical characterization

This section will display and discuss the results of the electrical characterization of the CNT/AgAu networks. The results are divided into three parts, where each is devoted to one of the following measurement modes:

- Current-voltage cycles in the positive voltage regime (0 $\longleftrightarrow$ U), showing resistive switching behaviour with distinct HRS and LRS.
- Current-voltage cycles in the positive and negative voltage regime (-U $\longleftrightarrow$ U), showing a voltage-induced reset.
- Time-resolved current measurements, showing a second-scale retention time potentially positively correlated to the duration of the SET voltage pulse.

3.3.1 Experimental details

The electrical characterization has been performed on a custom-made probing station, connected to a Keithley 2400 Source Measurement Unit (SMU). The SMU has been controlled by a PC via a RS-232 interface and the current compliance has been set to 100 μA for all measurements.
A custom software program has been developed for the purposes of thesis allowing for the automated execution of aforementioned measurement modes, as well as formatting and storing of measurement data.

3.3.2 Measurements

3.3.2.1 Unipolar voltage cycles

The unipolar resistive switching behaviour has been investigated by a current measurement pattern that works as follows: For each cycle the voltage starts at 0 V and is ramped up until either the threshold voltage of 7 V **or** the current threshold of 50 nA is reached. Then the voltage is held for 5 s before it is ramped down to 0 V again, and held for 5 s as well before the next cycle is started.

A respective measurement of a sample over 20 cycles is shown in *Figure 3.8*. Two distinct resistance states are visible, where at a voltage of 3 V the currents in the LRS are around two orders of magnitude higher than in the HRS. The inset in *Figure 3.8* displays the HRS and LRS currents at 3 V over the course of the voltage cycles. A unipolar, or rather diffusive, characteristic can be attributed to the CNT/AgAu network, since it is not necessary to apply reverse voltages to reset the resistance state to the HRS. Instead the resistance state resets over time while being at 0 V.

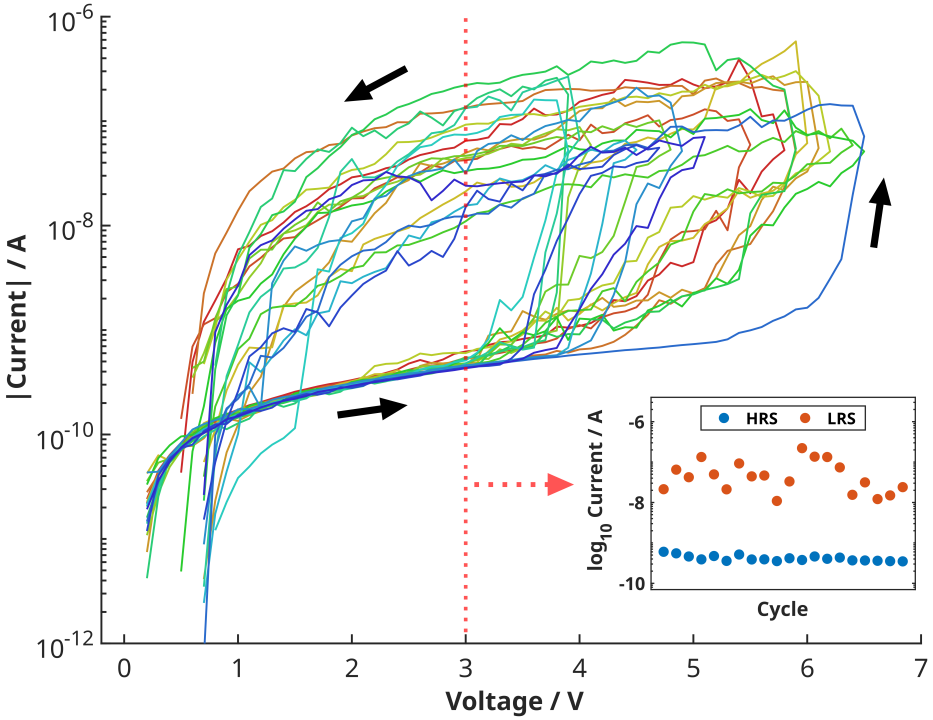

Figure 3.8: *Current measurement over 20 cycles with a current threshold of 50 nA. The inset shows the current values in the HRS and LRS over the cycles at a voltage 3 V indicated by the dashed line.*

The proposed switching mechanism is based on filamentary switching of the AgAu NP (cf. *section* 2.1.2.3). However, instead of an instantaneous reset - i.e. in the *ms* regime, cf. [86] and [80] - it is seen in *Figure 3.8* that there is no immediate reset while ramping down. Nonetheless, holding the voltage at 0 V before starting the next cycle shows to reset the resistance state consistently. This implies that the reset mechanism is diffusive in nature but differs quantitatively with respect to the time it takes to reset. This delay will be discussed in more detail in *section* 3.3.2.3.

3.3.2.2 Bipolar voltage cycles

During bipolar voltage cycles the voltage has been ramped into the negative voltage regime as shown in the current-voltage plots across three cycles in *Figure 3.9*. The resistive switching events from HRS to LRS and vice-versa are clearly visible and indicated by numbered arrows. The data shows that, in addition to the diffusive reset seen in *Figure 3.8*, the reset to the HRS also occurs by reverse voltages: During cycle 1, after switching to the LRS at ≈2.3 V in the positive regime, the reset occurred at -1.5 V before switching again at ≈-2.5V. The LRS is retained so

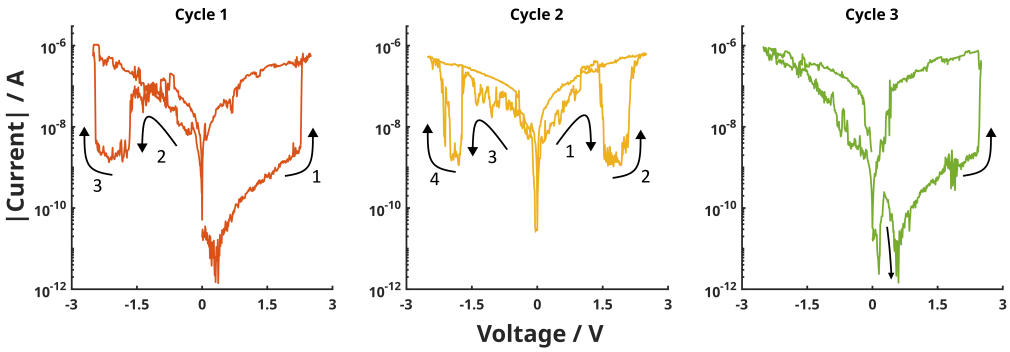

Figure 3.9: *Current measurement over three cycles where the voltage is ramped into the negative regime from 2.5 V to -2.5 V. It is shown how the resistance state is switched to the HRS at ±1.5 V during the first two cycles. However, the third cycle indicates, that this behaviour is not yet stable.*

that cycle 2 start in the LRS but shows a symmetrical behaviour: It resets to the HRS at ≈1.5 V before switching again at ≈2.2 V, and analogously in the negative regime.
This behaviour is a core feature of bipolar memristors, where the conductive filament collapses due to surface energy minimization which is thermally assisted by Joule heating (cf. *section* 2.1.2.1).
However, during cycle 3 the behaviour deteriorates. The negative regime of cycle 3 does not show distinct switching events any more, so it is proposed, that the filament has grown into a state where it is too stable to be dissolved by the RESET mechanisms. This indicates that a careful current control might be required to maintain a stable operation of the hybrid switching mode.

3.3.2.3 Time-resolved current measurements

A commonly considered figure of merit of memristive devices is the *retention time*, which quantifies the time for which the LRS is retained after switching. Bipolar memristors are designed to have retention times as high as many years, so they can be used as non-volatile memory cells[163], whereas diffusive memristors have retention times of few ms or even μs, so they reset immediately after the voltage falls below the RESET threshold (cf. *Figure 2.5*).
The retention time of the AgAu NP implanted CNT networks have been investigated by time-resolved current measurement, as shown in *Figure 3.10*. The voltage pattern applied to the sample is seen in the upper graph: At first 0 V is applied to serve as a reference. Then the voltage is set to the *READ* voltage of 0.5 V where it is seen, that the current does not change visibly and the readouts stay in the limit of detection of the SMU. This means that the sample is in its HRS, the resistance is substrate determined and thus that there is no short-circuiting current path.

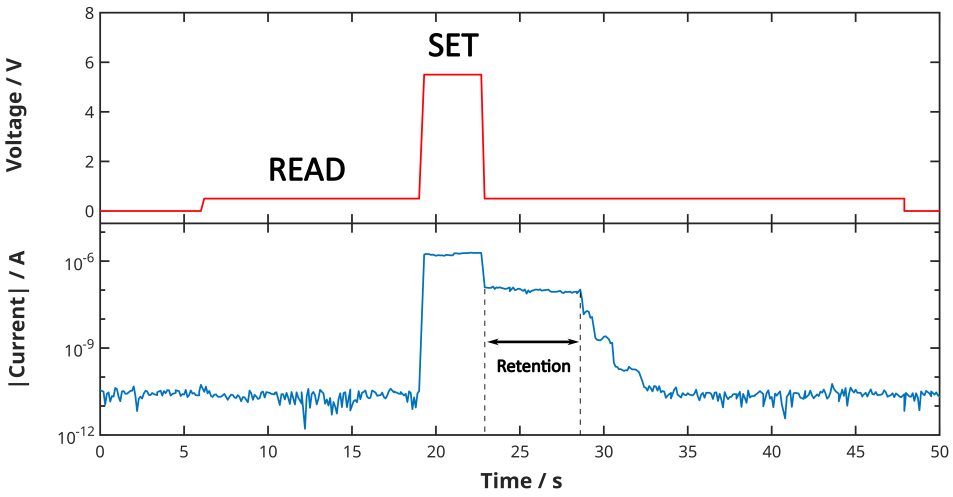

Figure 3.10: *Time-resolved current measurement, showing how the resistive switching of the AgAu NP implanted CNT networks is able to exhibit a considerable retention time of several seconds.*

As soon as the *SET* voltage of 5.5 V is applied, the flowing current drastically increases, indicating the transition into the LRS. The corresponding plateau in the current readout is at ≈1.7 μA. After the *SET* phase the voltage is reduced to the *READ* voltage again. However, now the current readouts show a significant current of ≈100 nA, which is several orders of magnitude higher than the HRS current. This means, that the LRS is retained after switching back to the *READ* voltage. The retention of the LRS holds for roughly 6 s, after which the current deteriorates over 4 s towards the initial HRS.

Altering the width of the SET pulses showed to impact the retention time as is indicated by the duration of the retained LRS in *Figure 3.11*. In this measurement, the retention time appears to be positively correlated to the duration of the SET pulse: the longer the SET pulse, the longer the retention time, which is shown as a graph in *Appendix* A.2. The gradual decay of the LRS current towards the HRS hints towards a multi-filament connection as this behaviour can be attributed to a stepwise thinning and collapse of participating filaments, whereas for the 0.1 s and 7 s pulses the abrupt current drop indicates a single filament collapse.

It is proposed that the significant retention originates from the availability of Ag atoms from the vicinity of the switching sites. As described in *section* 2.1.2.1 the filament lifetime and thus the retention time are directly related to the filament thickness[66]. Accordingly, in [86] the limitation of active species by the content of Ag in the AgAu nanoparticles has been found to be the cause of the diffusive switching mode.

For this case, it is proposed that the density of AgAu nanoparticles leads to a sufficient local availability to form filaments, whose thickness yields a lifetime in

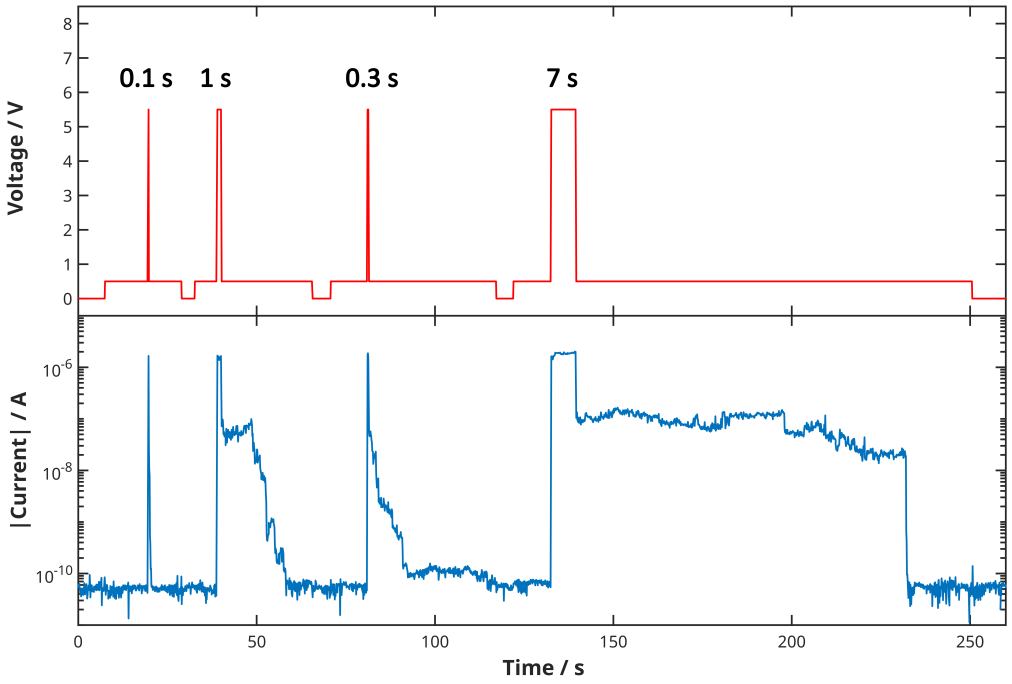

Figure 3.11: *Time-resolved current measurement with four SET pulses of different pulse widths indicated by the numeric value above the respective pulse. The retention time shows to be positively correlated to the pulse widths of the SET pulses, which is also displayed graphically in Appendix A.2.*

the second regime.
The finding of this intermediate state between bipolar and diffusive switching opens the question, whether a precise control of the density of nanoparticles can be utilized to tune the retention time of nanoparticle based resistive switching devices according to the needs of their application.

3.4 Conclusion

To conclude this chapter it will be summarized into two main claims that have addressed the challenges mentioned at the start of the chapter:

I) A conductive network of CNTs has been used as an approach to obtain nanoscaled distances in a lateral orientation without expensive or sophisticated equipment like clean-room technology. Facile preparation techniques such as ultrasonication and spin-coating have been utilized to deposit a CNT network in a controlled manner, while subsequent Joule-heating ensured the sparsity of the network by removing any conducting pathways. The current readouts never exceeding

the low μA regime also indicate that the CNT network acts as a series resistance. Inherently limiting the current yields a low-power consumption without the need for additional circuitry.
The stochastic nature of this route incentivizes to consider it for further multi-terminal approaches, where neuromorphic features, such as reservoir computing, emerge from the network dynamics[34, 164, 165].

II) A memristive device has been realized by sparsely adding AgAu nanoparticles to the CNT network, yielding ECM-type resistive switching between them. The CNT/AgAu networks showed the behaviour of operating at a border between diffusive and bipolar switching, yielding retention times in the regime of seconds, while keeping the capability to be reset by reverse voltages. The timescale of the retention time indicates the possibility for a biologically plausible short-term memory, which occupies the spot between non-volatile bipolar cells and volatile diffusive ones.
Technically, the implementation of a short-term memory offers a measure to store momentarily relevant information though erasing itself automatically, improving its energy efficiency. The capability of a bipolar reset offers additional flexibility, if the state has to be erased immediately.
This memory effect is attributed to the availability of silver as an active species from the surrounding AgAu nanoparticles. It is directly impacting the thickness and thus the lifetime of the silver filaments, which are the main factor for the resistive switching. The results suggest that a careful control of the availability of active material in the vicinity of switching sites can be used directly to tune the retention times of filament based resistive switching devices.

Now while in this chapter electrochemical metallization has been discussed as a mechanism on the nanoscale for resistive switching, the next chapter demonstrates how the same process can be deployed for the dynamic reconfiguration of network topology on a length scale several orders of magnitude larger.

Chapter 4

Network Space: Dynamic Topology in Liquid-Solid Systems

Two key aspects of biological neural networks that are interwoven inseparably are the network's topology and its dynamics[166]. Topology describes the structure, i.e. the arrangement of individual building blocks to form a larger network. The resulting connectivity is essential for the signal transmission and thus the function of the neural network. Features such as clustering, modularity and small-world configurations are decisive for the network's efficiency[35, 166].
Dynamics on the other hand describes the spatio-temporal development of the network. With respect to the topology this includes its plasticity, where connections grow, strengthen or decay based on the network's activity. Additionally, it covers the temporal evolution of the neurons' synchrony state.
To address the network space respecting both topology and dynamics, in this chapter two approaches will be presented that are capable of modifying the topology of a physical network either explicitly via guided redox wiring (*section* 4.1) or collectively by dielectrophoresis (*section* 4.2).
The aspect of dynamics is covered by showing how relaxation-type oscillators are coupled by guided redox-wiring yielding a synchronization and desynchronization based on their connection state.
Furthermore, it is discussed how several features of guided redox-wiring are resembling mechanisms in biological neural assemblies such as Long-Term Potentiation (LTP).

Several parts of this chapter have been excerpted from the following publication to which the reader is also referred:

[167]: **M.-I. Terasa**, T. Birkoben, M. Noll, B. Adejube, R. Madurawala, N. Carstens, T. Strunskus, S. Kaps, F. Faupel, A. Vahl, H. Kohlstedt, R. Adelung, 2023, "Pathways towards truly brain-like computing primitives", *Materials Today*, DOI: 10.1016/j.mattod.2023.07.019

4.1 Directed Connectivity by Guided Redox-Wiring

This section describes a concept for a liquid-based system that is capable of forming interconnections between electrodes dynamically, which can be controlled by the activity of the participating electrodes in the form of an electrical potential. Due to the approach being inherently directed, it changes a networks topology by establishing explicit connections between most active nearest neighbours.

4.1.1 Materials and Methods

For all experiments in this section dimethyl sulfoxide (DMSO) (supplied by Carl Roth GmbH, purity ≥99.5%) has been used as a solvent for the liquid electrolyte. Two different substrates have been used: SEM and EDX measurements have been performed on a custom-made PCB (see *Figure 4.1c*)[1]. All other experiments have been conducted on a custom PCB provided by *JLCPCB* shown in *Figure 4.1a* and *b*, whose electrodes consist of nickel plated copper.
Voltage supply and current measurements have been performed by a PC-controlled Keithley 2400 SMU and images have been recorded by a digital microscope camera.
EDX measurements have been performed with the EDX detector of the SEM (see *section* 2.8.1).

4.1.2 Proof of Principle

The basic experimental setup in its most simple form is depicted in *Figure 4.1d*: At least two electrodes are submerged in the electrolyte and a voltage is applied. By electrochemical metallization, which has been described in detail in *section* 2.1.2, metal atoms from the anode dissolve, drift towards the cathode and are reduced again. By the nucleus formation and subsequent material deposition on the cathode being mainly directed towards the anode it is indicated that the electrical field induced drift of ions dominates over random diffusion. Additionally, the nucleus distorts the electrical field enhancing the drift towards it, making it a self-enhanced process. This ultimately results in a filament-like connection between the electrodes as seen in *Figure 4.1d*. The filament-determined conductivity is further considered to be the "connection strength" between the participating electrodes.

[1] Produced by Tom Birkoben at the Chair for Nanoelectronics, Kiel University

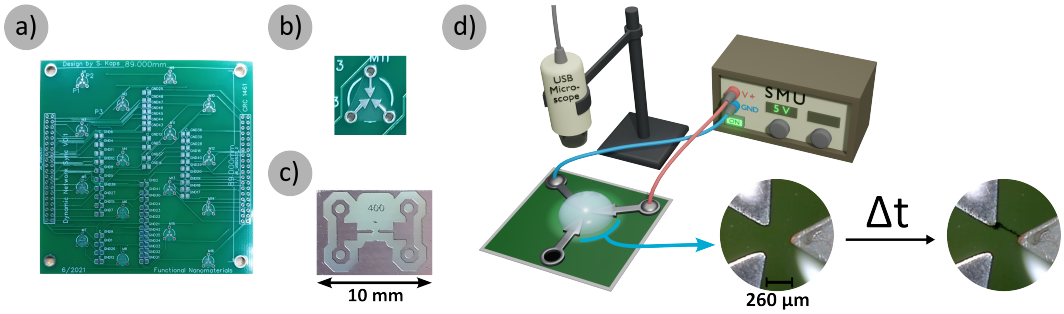

Figure 4.1: *Basics for guided redox-wiring experiments. a) Photograph of the PCB used as a substrate. The size is 100×100 mm. b) Zoomed photograph of one set of electrodes on the PCB in a). The nominal distance between the electrodes is 260 µm. c) Custom made substrates used for EDX and growth time experiments. d) 3D-schematic of the experimental setup, illustrating how the current measurements and microscope images have been acquired. The photographs show examples of how the microscope images will look like when acquired with this setup.*

The development of a connection can be read from its current profile. An example is given in *Figure 4.2*, where a time-resolved current measurement is shown. The insets show microscope images of the electrodes submerged in DMSO at the respective timestamps.

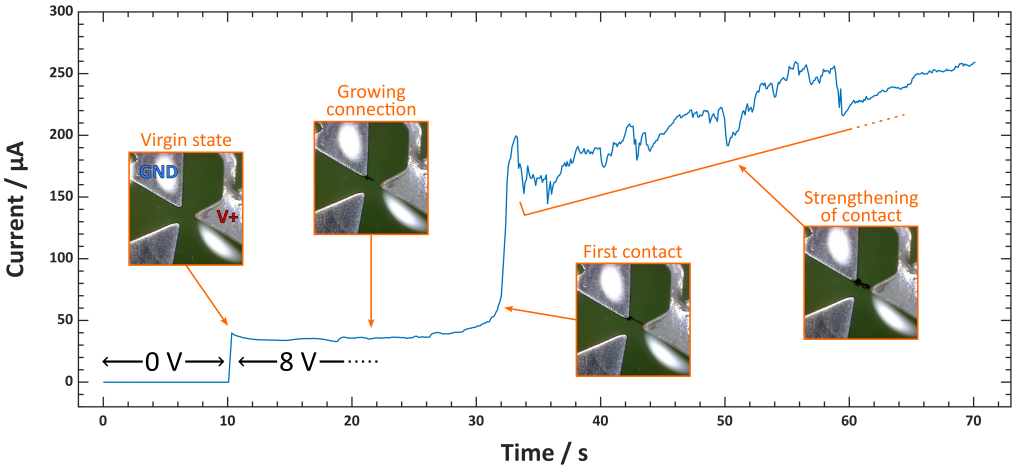

Figure 4.2: *Time-resolved current measurement for two electrodes submerged in DMSO at a constant bias voltage of 8 V. The insets show microscope images of the experiment for the respective time regimes.*

After the first 10 *s* where the voltage supply had been set to 0 *V*, a constant bias voltage of 8 *V* has been applied (*virgin state*). Over time a filament starts

to grow, while the current remains stable since at this stage it is limited by the kinetics of the electrochemical reactions (*growing connection*). As soon as the filament reaches the anode, it contributes to the conductivity and the flowing current rises quickly according to the now filament-determined resistance (*first contact*). However, the electrochemical metallization still continues. The filament grows in thickness and new branches form leading to a gradual increase in overall conductivity by the increase in total conduction cross-section (*strengthening of contact*).

4.1.3 Filament Characterization

4.1.3.1 Chemical Analysis

The chemical composition of the growing filament is proposed to consist mainly of the metal species involved in the electrochemical redox reaction of the metallization process. This is confirmed by EDX measurements conducted on PCB substrates with copper electrodes. *Figure 4.3a* shows an electron image of a substrate as shown in *Figure 4.1c*. A filament has been grown in between the electrodes, after which the electrolyte has been left to evaporate. The respective EDX map for the Cu Lα_1 transition is shown in *Figure 4.3b* indicating, that the filament mainly consists of the electrode material. However, while signals for C and O are caused by organics such as the substrate material or residues of the solvent, the stronger O signal originating from the filament indicates that it also contains an amount of copper oxide. Since the filaments are black under an optical microscope it is assumed that the filament's outer surface is oxidized during growth, although the specific reaction has not been clarified.

4.1.3.2 Tuning Growth with Additives

One striking advantage of the approach to deploy a liquid matrix as a coupling medium is the feasible possibility to mix in solvable additives into the electrolyte. This allows to adjust the behaviour of the liquid considering the additive species and concentrations as new degrees of freedom.
Here, this is briefly showcased by the tuning of the growth kinetics to increase or decrease the time a filament needs to form between two electrodes. Two electrolytes have been prepared by mixing methylene blue (MB) into pure DMSO with concentrations of 10^{-2} mol/l and 10^{-3} mol/l.

A drop of electrolyte has been placed on a substrate as shown in *Figure 4.1c*, where both electrodes have been connected to the SMU. While measuring the current, DC bias voltages from 1 V to 8 V have been applied until a metal filament has formed. The current compliance has been set to 500 μA. As soon as a filament had formed, the voltage has been kept for several seconds before it has been turned

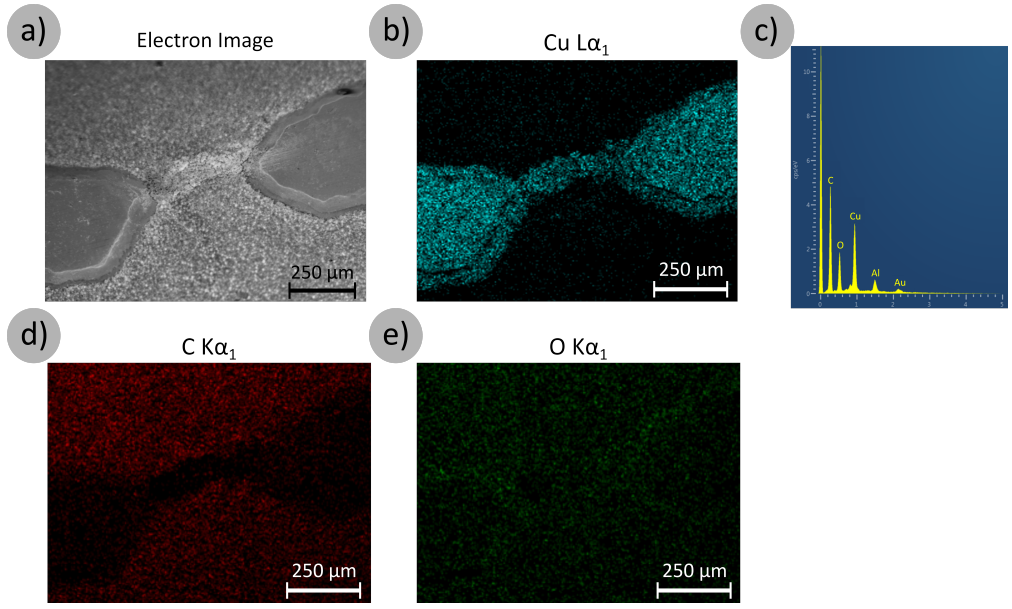

Figure 4.3: *EDX measurement of a Cu filament grown by redox-wiring. a) Electron image of the substrate with filament. b) EDX map of the Cu $L\alpha_1$ signal, indicating that the filament consist of the electrode material. c) Spectrum of the EDX measurement. d,e) C $K\alpha_1$ and O $K\alpha_1$ maps respectively. The difference between both maps indicate that the filament contains a significant portion of O as well.*

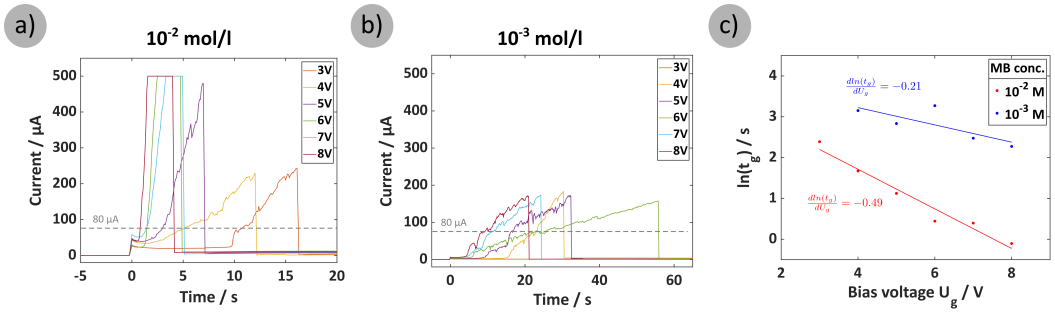

Figure 4.4: *Tuning of growth kinetics by methylene blue concentration in the electrolyte. a+b) Time-resolved current measurements at different DC bias voltages with the respective methylene blue concentration. The time-axis is referenced to the start of the voltage application. In b) the 3 V bias did not show any visible reaction. c) Scatter plot with the applied bias voltage U_g on the abscissa. The time t_g on the ordinate indicates the time since voltage application after which a current threshold of 80 µA is reached.*

off.
The respective current measurements are displayed in *Figure 4.4a+b*. To compare

the growth times of the measurements, a common current threshold has been defined to 80 μA. The threshold has been chosen to be sufficiently higher than the initial current for all measurements to resolve to filament contact point.
Figure 4.4c shows the time t_g for the respective applied voltage U_g until the threshold voltage is reached, where t_g is displayed in natural logarithmic scale. A linear fit has been performed using *MATLAB* 2022a and the respective slopes are shown, indicating the effect of the additive concentration on the growth kinetics. Considering the Butler-Volmer equation in *Equation* (2.3), the linear $\ln(t)$ dependence suggests an increasing effect of the MB on the charge transfer coefficient α.

4.1.4 Emulating Neuromorphic Features

Up to this point, the concept of guided redox-wiring has been shown in principle and characterized with respect to fundamental aspects. This section will address certain features that link the approach to the field of brain-inspired computing.
At first it is covered how guided redox-wiring mimics the mechanisms of distance-dependent guidance and long-term potentiation (LTP, see *section* 2.6.1) found in neural assemblies. Afterwards it is showcased how the guided-redox wiring platform is integrated into oscillator circuits, where it is leading to a synchronization and desynchronization of relaxation-type oscillators, which is a basal mechanism for higher brain functions, as introduced in *section* 2.6.2.

4.1.4.1 Distance-Dependent Guidance

Distance-dependent guidance is a mechanism of connectome development in the brain stating that the connection probability between neurons during axon growth decreases exponentially with the distance between them. This behaviour is based on several factors, e.g. the pure stochastic chance of hitting another neuron while growing or a molecular concentration gradient diverting the axon along the gradient[168].
In the context of guided redox-wiring the directed nature of the effect originates from the electrical field, affecting the ion drift in the electrolyte.
For a given potential applied to electrodes relative to a common GND, the electrical field E becomes weaker for electrodes farther away. So by considering

$$v_d = \mu E \tag{4.1}$$

the drift velocity v_d shrinks with E if the ion mobility μ is assumed to be constant in the electrolyte.
In *Figure 4.5a* it is shown how the same potential is applied to an arrangement of electrodes, one of which is farther away than the other two. It is seen, that the redox-wiring is guided by the lower distance towards the closer electrodes, while the distant one is avoided.

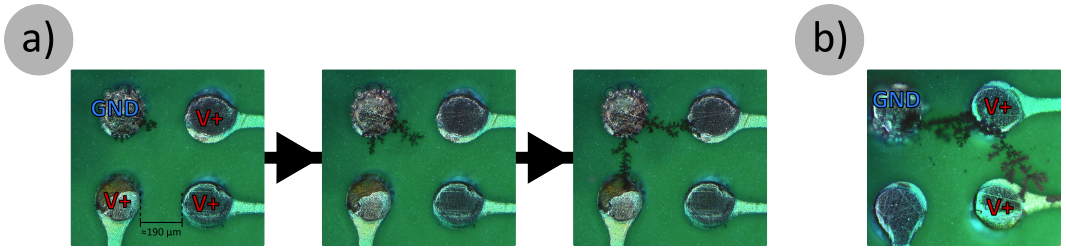

Figure 4.5: *Microscope images showcasing the distance effects in the guided redox-wiring. The applied bias voltage has been $V_+ = 7V$ in all cases. a) An application of equal potentials to the electrodes leads to a growth towards both the nearest electrodes but not the one farther away. b) Applying the voltage in the shown configuration the filament forms a path to the distant electrode with the nearest electrode acting as a mediator.*

Since the filament growth is a self-enhancing process due to the field concentration at the filament tip, the closer electrodes will be reached much faster. This in turn inhibits the growth towards the farther one, as the filament contact will establish a parallel low-resistance current path. However, *Figure 4.5b* shows, that a close electrode can act as a mediator. The filament changes the potential distribution, so that the potential between the distant electrode and the filament suffices to trigger redox-wiring towards it as soon as it has reached the close electrode.

4.1.4.2 Mimicking LTP

Guided redox-wiring is able to mimic the behaviour of LTP by applying a bipolar pulsed voltage signal to the electrode as the synaptic activity. In order to elucidate on this, a two electrode setup with liquid coupling is considered. A voltage pulse pattern U with an amplitude U_0 and a common GND is applied to the electrodes, so that a potential difference ΔU will develop between them. With the voltage threshold to trigger redox-wiring being denoted as U_g and $U_0 < U_g$, three cases can be distinguished, depending on the temporal relation between the pulses, which determine whether redox-wiring occurs. The three cases, that are also visualized in *Figure 4.6*, are:

- × **No pulse overlap:** If the pulses do not overlap at all, the potential difference ΔU will be limited to be U_0 at most. Thus, $\Delta U < U_g$ holds at any time, so no filament will grow.
- × **Full pulse overlap:** For perfectly simultaneous pulsing, the potential drop between the electrodes will be zero at all times, preventing redox-wiring.
- ✓ **Partial overlap:** In the case that the pulses overlap partially, there will be a time-window where the potential drop will be $\Delta U > U_g > U_0$, whenever

one pulse is in the negative regime, while the other one is currently positive. During this time frame redox-wiring will occur.

The microscope images in *Figure 4.6* indicate the connection state after applying the respective voltage pattern to the electrodes repeatedly, where $U_0 = 4V$ and the total pulse width has been $4s$. In the case without overlap the potential difference has been insufficient to yield a complete filament (red box). Whereas, if applied with partial overlap the voltage pulses trigger redox-wiring enough to create a full filament over time (green box), thus mimicking how repeated close pulsing with appropriate waveforms can potentiate the connection between active electrodes.

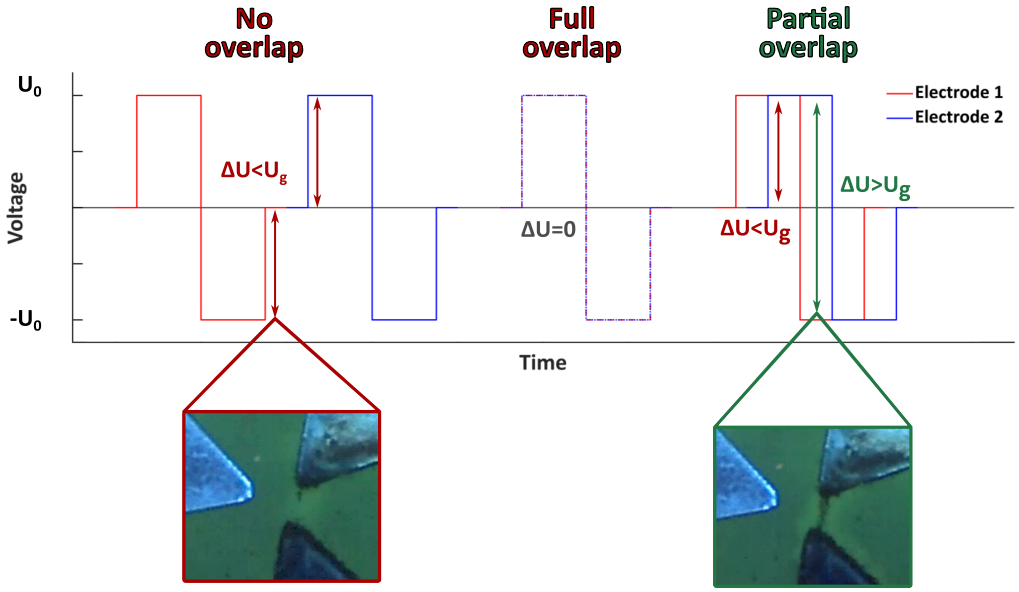

Figure 4.6: *Schematic plot distinguishing three cases of spiking between two electrodes, where U_g denotes the voltage threshold necessary to trigger redox-wiring. Only if the voltage pulses are sufficiently close to each other temporally (**partial overlap**), the potential drop exceeds U_g, triggering redox-wiring. This is indicated by the microscope images showing the growth states after 1 min with the respective voltage patterns ($U_0 = 4V$, $4s$ total pulse width).*

4.1.4.3 Synchronization of Oscillatory Ensembles

In *section* 2.6.2 the role of neural dynamics for cognitive functions has been introduced. In order to explore the prospects of a technical emulation of leaky integrate-and-fire neurons, relaxation-type oscillators have been combined with the liquid coupling of the guided redox-wiring approach.

The oscillators have been described in detail in the Supporting Material of [167],

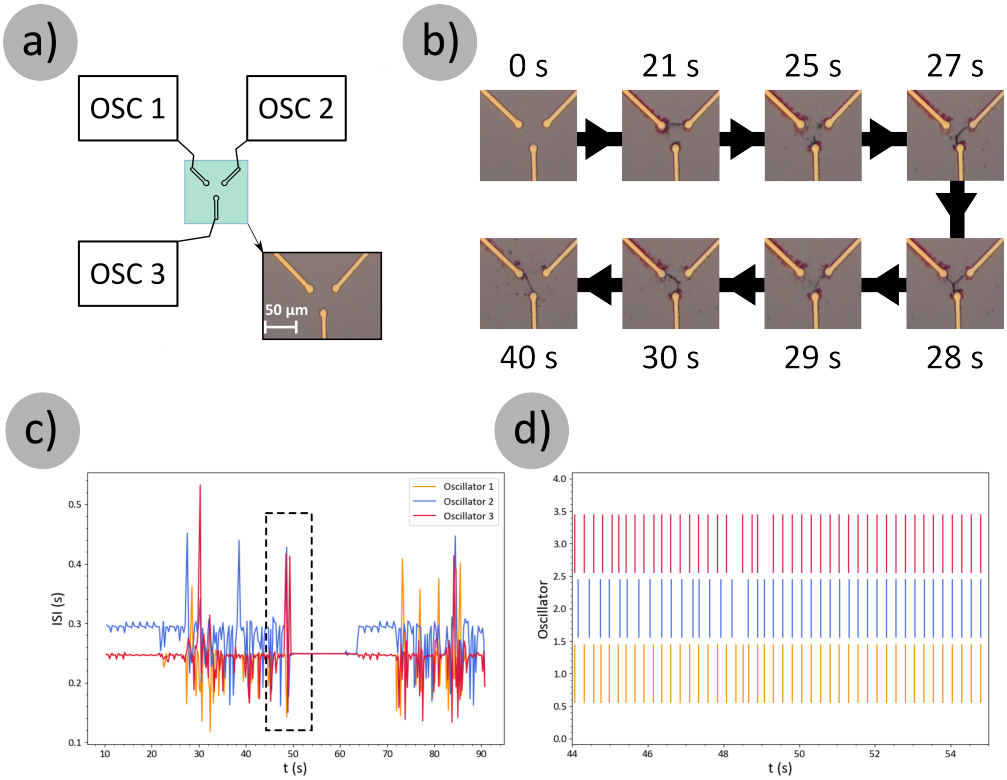

Figure 4.7: *Results of coupling three relaxation-type oscillators via guided redox-wiring. a) Schematic of how the oscillators have been coupled. The micrograph shows a microscope image of the gold contacts on the silicon substrate. b) Time-series of microscope images showing how the oscillators affect the connection state between the electrodes dynamically. c) Interspike intervals of the oscillators. It is shown how the oscillators synchronize by the filament coupling in the time window around 50 s to 70 s. d) Time-resolved oscillator spikes in the time window where the synchronization starts, indicated by the dashed box in c). Adapted from [167].*

which is provided as well in *Appendix* A.3[2].
The coupling has been established by placing a mixture of 1 mM $Zn(CH_3CO_2)_2$ in DMSO on a SiO_2 substrate with patterned gold contacts, fabricated by a standard UV-lithography and sputter deposition process. The setup as well as the substrate are shown in *Figure 4.7a*.
A time series of micrographs is shown in *Figure 4.7b* showing the connection state at the given timestamp. Initially, the oscillations are not synchronized, which is indicated by the oscillators' different interspike intervals (ISI), as can be seen in *Figure 4.7c*. Thus, there are repeated voltage drops between the electrodes. In this case the Zn^{2+} ions act as the active species forming the conductive filament by

[2]Text and figure created by Maximiliane Noll, Chair for Nanoelectronics, Kiel University

redox-wiring as can be seen in the micrographs. During the first 50 s the filaments are not stable and are ruptured due to the ongoing oscillations. However, after 50 s a filament formed branching to all three electrodes increasing the conductivity in between them for long enough to synchronize all oscillators. This synchronized state is clearly indicated by the equal ISI of all oscillators in *Figure 4.7c* as well as in *Figure 4.7d*, where the time-resolved oscillator spikes are shown. Since they now oscillate in phase, there is no voltage drop between them any more leading to a regime of synchrony. After the filament has collapsed over time the oscillators slowly start to desynchronize again.
The results indicate that redox-wiring is a suitable approach to couple an oscillatory ensemble for the emulation of neural mutual phase-synchronization.

4.2 Collective Connectivity by Dielectrophoresis

This section covers a liquid-solid composite system based on ZnO nanoparticles dispersed in a liquid solvent with low electrical conductivity. The application of a dynamic input on the composite in the form of an oscillating electrical field via an array of electrodes leads to a drift of particles by dielectrophoresis. The resulting rearrangement of the particles over time leads to a densification between certain electrodes, where a sufficient density between two electrodes is considered as an interconnection. Thus, the topology of the whole network is determined by the particles' density profile, which is altered collectively.
In the following sections a proof of principle for the concept is discussed by the example of ZnO particles. The sensitivity of ZnO towards UV-light is used to motivate the approach and assess the connection strength between electrodes.

4.2.1 Proof of Principle

The ZnO particles have been dispersed in the liquid matrix initially. The dispersion has been prepared by mixing 5 wt% ZnO particles ($< 200\ nm$, provided by Sigma Aldrich) in DMSO and homogenizing it by ultrasonication (Sonics Vibra-Cell VC 505 with 500 W at 35% amplitude for 1 min).
In order to densify the particles according to a specific pattern, a drop of the dispersion has been placed on the electrode grid of a BGA-36 PCB (supplied by ProtoAdvantage, see *Figure 4.8a*) with a pipette and an alternating square voltage with an amplitude of 10 V and a frequency of 0.5 Hz has been applied to the electrodes via a computer-controlled *Keithley 2400* SMU (see *Figure 4.8c*). The nominal grid spacing is 400 μm, with a surface-to-surface distance of $\approx 190\ \mu m$.
Adajcent electrodes have been connected to alternating polarities as exemplarily displayed in *Figure 4.8d* so that each electrode's direct neighbours always have opposite voltage signs and thus corresponding electrical field lines.

Via dielectrophoretic drift the particles have been densified in the pattern according to the actuated electrodes as shown in *Figure 4.8b* and *d*.

This shows how oscillating electrical signals are capable of changing the density distribution of particles according to the input.
To assess the topology of the network of ZnO particles, the UV-sensitivity of paths between electrodes is taken as a measure. *Figure 4.9* shows how a high-density region of ZnO particles has been formed. By applying the alternating voltage pattern to the columns 3 and 4 (see *Figure 4.9b*) the particles densify between them, while the rest of electrodes lies in a low-density region. Time-resolved current measurements have been performed from a common GND electrode to five distinct electrodes both in the high- and low-density regions as shown in *Figure 4.9b* at a constant bias voltage of $U = 1V$. The substrate has been illuminated with a pulse of UV-light during the measurement, as indicated by the purple regime in *Figure 4.9c*, to act as an external stimulus.

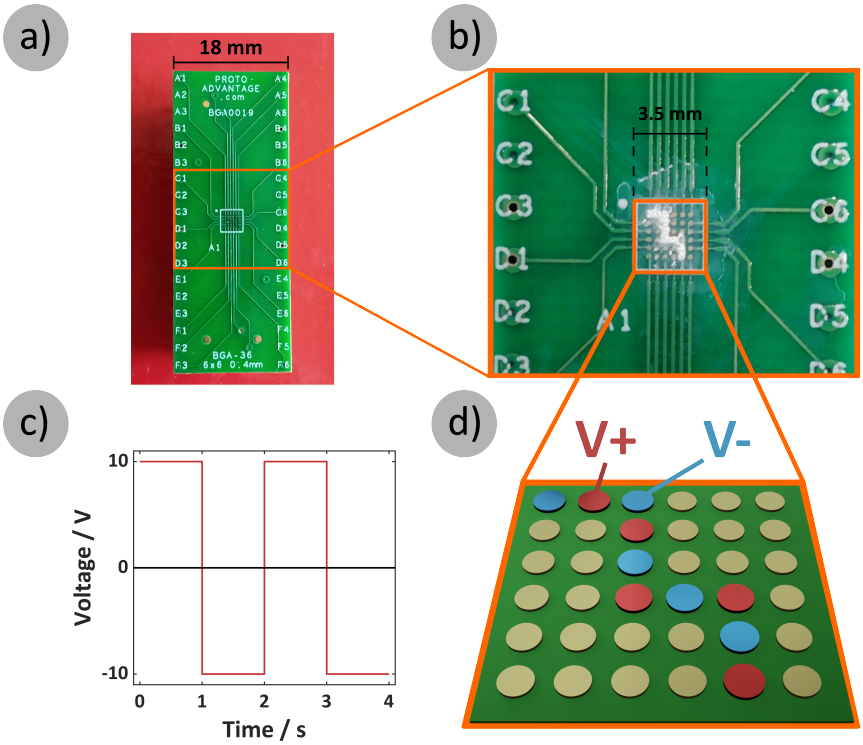

Figure 4.8: *ZnO nanoparticles rearranged by oscillating electrical fields between electrodes. a) Photograph of the BGA-36 PCB used as a substrate. b) Photograph of the electrode grid after arrangement of ZnO particles. c) The voltage pattern applied to the electrodes. d) Schematic showing which electrodes have been actuated. Adjacent electrodes have been connected to alternating polarities.*

It is seen in *Figure 4.9c* that the difference in particle density between the regions yields a corresponding qualitative difference in stimulus response. Thus, it is evident that this approach allows to unify plasticity as a network feature with sensor capabilities via according material choices.

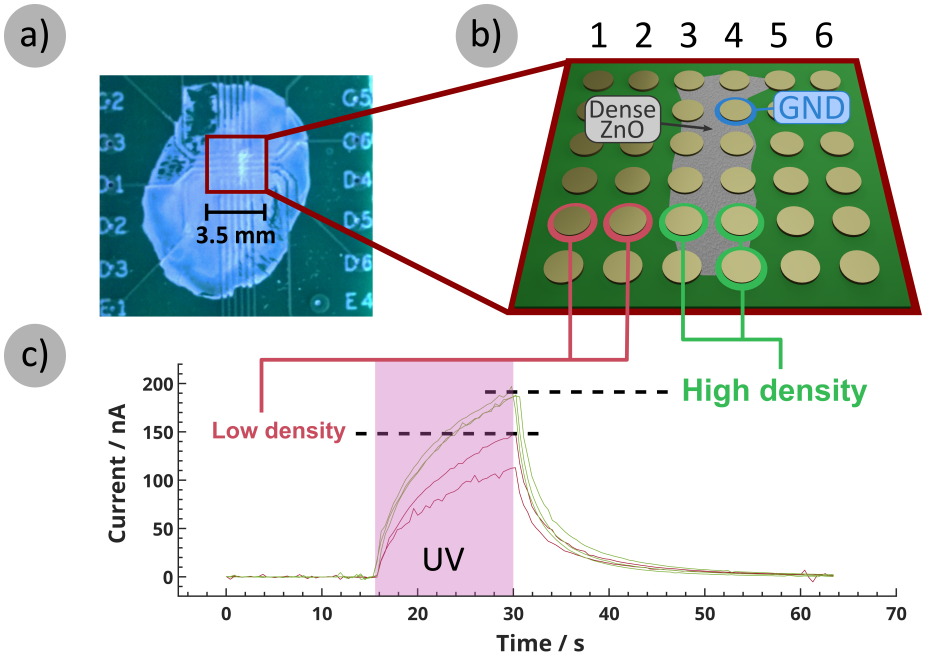

Figure 4.9: *Rearrangement of ZnO nanoparticles to regions of low density and high density, showing respective UV-sensitivity. a) Photograph of PCB after dielectrophoresis. b) Schematic showing which electrodes have been measured for the sensitivity measurement. c) Current-Time plot showing the UV-response of paths from GND to electrodes in low-density and high-density regions. The bias voltage for the current measurements was* $U = 1V$.

To showcase the approach's potential to dynamically change the collective connectivity of a whole network, it has been applied to a collection of 16 relaxation-type oscillators, which are described in detail in *Appendix* A.3. The oscillators have been connected to the central 4×4 grid of the PCB while the outer electrodes have been connected to GND. In *Figure 4.10* three sequential photographs are displayed representing the initial state as well as the timestamps of 9 s and 18 s of the experiment.[3] It can be seen how the topology of the network changes over time via the input from the oscillators, forming new connections between electrodes (e.g. B3-C3 or C1-C2) as well as breaking up others (e.g. B3-B4).

[3]The experiment has been conducted and recorded by Tom Birkoben and the experimental details have been described and discussed in [169] pp. 119-124.

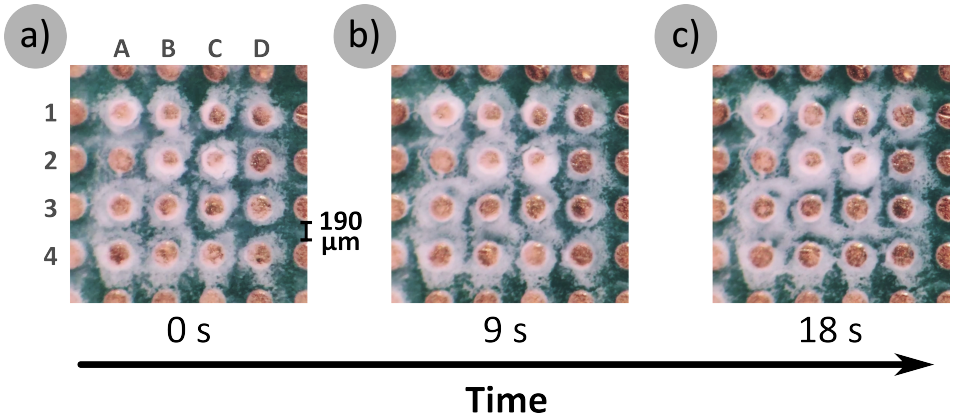

Figure 4.10: *Time series of photographs showing how 16 relaxation-type oscillators connected to the central 4×4 grid of electrodes (A1-D4) reshape the topology of the ZnO particle network.*

Closing up this section, it has been shown that in a liquid-solid-composite system functional particles can act as the network-defining feature of a network and be re-arranged dynamically by oscillating input of electrical fields. The current measurement in *Figure 4.9c* reveals that electrodes connected by a high-density region show a higher UV sensitivity than the electrodes in low-density regions. It indicates that the density-dependent functionalities of a particle species can serve as a parameter for a networks topology. This is particularly interesting for materials with sensor features, since it inherently combines a degree of plasticity for a network with an interface to external stimuli.

4.3 Conclusion

This chapter has covered the network space from the perspectives of topology and dynamics by introducing two approaches to change a network's topology according to a dynamic external input. Both exhibit a degree of plasticity:
Guided redox-wiring constitutes the topology of a network by conductive filaments growing between network nodes via electrochemical metallization and is able to mimic LTP and distance-dependent guidance, while also providing the capability to impact the dynamics of a network by synchronizing and desynchronizing oscillator ensembles.
The bottom-up nature avoids the pre-determined connectivity of cross-bar arrays and limits the demand of network resources to the regions of activity.
Simultaneously, the approach allows for true three-dimensional connectivity enabling a higher number of nearest neighbours and thus more complex network

layouts.
In a two-terminal setup redox-wiring can also be considered as part of the component space, providing activity dependent resistance.
As a small tangent to the design space, making use of sufficiently thick filaments, it is also conceivable to establish an input-dependent long-term stable pre-connectivity via redox-wiring.

Concerning the network of ZnO particles, the plasticity is expressed via the particle density, that has been shifted by dielectrophoresis, strengthening certain connections while simultaneously weakening others. By using functional metal oxide particles in the form of ZnO, it was possible to represent the connection strength by respective UV-sensitivity. This is a promising starting point towards memsensitive capabilities as it directly combines network plasticity with sensor features.

The next chapter discusses the usage of metal oxide particles as a sensor material as well. However, instead of treating an inherent plasticity, it focuses on the facile and flexible fabrication of sensor parts that have been pre-designed according to the design space.

Chapter 5

Design Space: 3D-Printed Sensors for Pre-Determined Functionality

In the context of the design space, in this chapter components with a pre-defined blueprint and thus an according functionality are covered. A prominent example for such elements in biological life are sensory features such as photoreceptors, which are paramount for the intake of information that is further processed by the nervous system.
Accordingly, this chapter covers the concept, fabrication and characterization of sensor devices made by means of additive manufacturing (AM).
It is shown how AM is deployed by means of direct ink writing (DIW) to fabricate photo- as well as gas sensor devices with tremendous design freedom regarding in-plane geometric shape and material choice and how additional post-processing steps can be utilized to further enhance the applicability of printed components.
Finally, the tunability of the sensing properties of metal-oxide semiconductors (MOS) by decoration with nanoparticles is discussed to serve as an incentive outlook for further increasing the enormous versatility of additive sensor fabrication.

A large part of this chapter has been excerpted from the following publication to which the reader is also referred:

[136]: **M.-I. Terasa**, L. Siebert, S. Kaps, P. Holtz, O. Lupan, J. Carstensen, F. Faupel, A. Vahl, R. Adelung, 2023, "Smart sensor arrays", Springer International Publishing, DOI: 10.1007/978-3-031-36705-2_11

5.1 Methodology of Print Preparation

This section presents the steps for the preparation to perform any particular print in procedural order. It showcases the large freedom of the DIW process with respect to geometry and used materials, which are defined by the computer-aided design (CAD) file and ink composition respectively.

5.1.1 Computer-Aided Design

In order for a 3D-printer to print a particular object, the data describing it has to be created digitally, which is most commonly achieved by tools of CAD. CAD programs are used to model or construct three-dimensional objects and commonly offer useful features such as symmetry, alignment or boolean operations (examples can be found in *Figure 5.1a+c*). The final shape information is stored in a respective file format such as OBJ or STL.

5.1.2 Slicer

Depending on the type of printer the shape of an object is interpreted by another software to convert the pure shape information into commands for the printer. For FDM printers, which build up the print layer by layer, a so called "Slicer" software splits the object into a number of layers (see *Figure 5.1b*). For each layer the traversal path for the extrusion head and amount of extruded material is calculated and respective printer commands - most commonly in the form of G-codes - are generated and stored in an ASCII-file.
By creating a planar 3D design, whose height is lower than or equal to the layer thickness of the printer, it is possible to print a single layer of material with two-dimensional geometries (cf. *Figure 5.1c+d*).

An overview over the softwares used in the scope of this work is given in *Table 5.1*.

Table 5.1: *Overview over software programs used to prepare and operate the 3D printer.*

Software	Usage
Autodesk Inventor	Construction of 3D-models
Slic3r	Slicing
Repetier	Printer firmware
Repetier Host	Printer operation

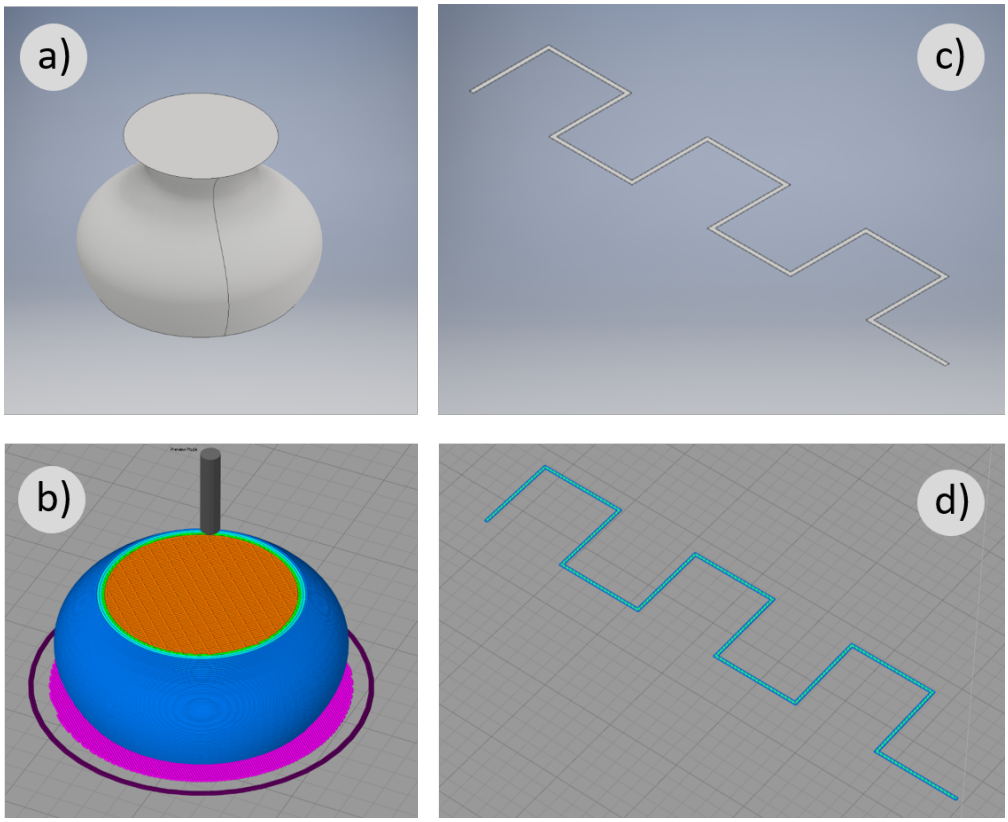

Figure 5.1: *Examples of CAD modelled objects and their sliced representation. a) A three-dimensional vase model created with* Autodesk Inventor 2019. *b) The vase is sliced into 202 layers, each showing the path the printhead will take. The cross-section reveals the rectangular fill pattern inside the object. c) A meander-like object with a nominal height of 0.2 mm. The sliced version seen in d) consists of one layer of material only.*

5.1.3 Ink preparation

The inks prepared for this work are based on ethanol (EtOH) as a solvent and polyvinyl butyrale (PVB) as a polymeric binder, making up the carrier fluid. The system PVB/ethanol has several beneficial features, explained in more detail in *section* 5.2. Functional micro- or nanoparticles are mixed into ethanol and the PVB is added under constant stirring, until the ink is homogenized.
The viscosity of the ink are determined by the amount of binder as well as the filling factor and species of microparticles. The carrier fluid for the prints performed for this work has been produced with a binder-to-solvent ratio of 1:3, whereas the filling factor of particles depends on the species. Inks containing t-ZnO have been produced with a filling factor of $\leq$ 20 wt%, since the tetrapodal structures tend to entangle and clog the extruder nozzle at higher contents. Inks with spherically

shaped particles of Fe, Cu and Zn have been produced with filling factors of up to 50 wt%, whereas for conductive inks with CNTs the filling factor was up to 2 wt%.

5.2 Post-processing

Using ethanol (EtOH) as a solvent and polyvinyl butyrale (PVB) as a polymeric binder has shown to yield interesting possibilities, which are exposed by the post-processing steps described in this section. They are further enhancing the flexibility of DIW for micro- or nanoparticle based components and can possibly be transferred to other similar systems as well.

5.2.1 Delamination and Re-application

An EtOH/PVB based ink can be printed on a glass substrate (see *Figure 5.2a*). Since PVB is a hydrophobic polymer, submerging the glass substrate in H_2O makes the printed material detach from the glass (see *Figure 5.2b*). If printed thinly, the composite becomes a flexible, self-supported structure, that can e.g. be folded to 2.5-dimensional shapes.
In addition, every printed part can be re-attached to any suitable surface, if slightly wetted with EtOH, including round or complex ones (see *Figure 5.2c*). Since printing and most other deposition techniques, such as sputter deposition, on this kind of surface are unfeasible or even impossible, this step dramatically increases the applicability of printed components for a much wider range of implementations. Furthermore, parts printed separately can be unified by wetting the interfaces with EtOH allowing to assemble devices freely without the need for multi-material printing (see *Figure 5.2d*).

5.2.2 Laser Milling

Heat treatment is a very common tool for the removal of sacrificial polymeric components, which in this case is the binder in the colloidal inks. Conventional heat treatment, e.g. annealing in an oven, has the downside that the heat is applied unlocalized and slowly. During this work, a computer-controlled 100 W CO_2 laser ($\lambda = 10.6\mu m$, provided by GS Lasersystems) has been deployed instead of traditional heating. The laser head can be moved in relative XYZ-axes and is controllable in terms of movement speed and radiation power allowing for flexible and precise heating with respect to localization and power transfer. In the following it is shown qualitatively how the energy transferred to the sample can be controlled by the process parameters:

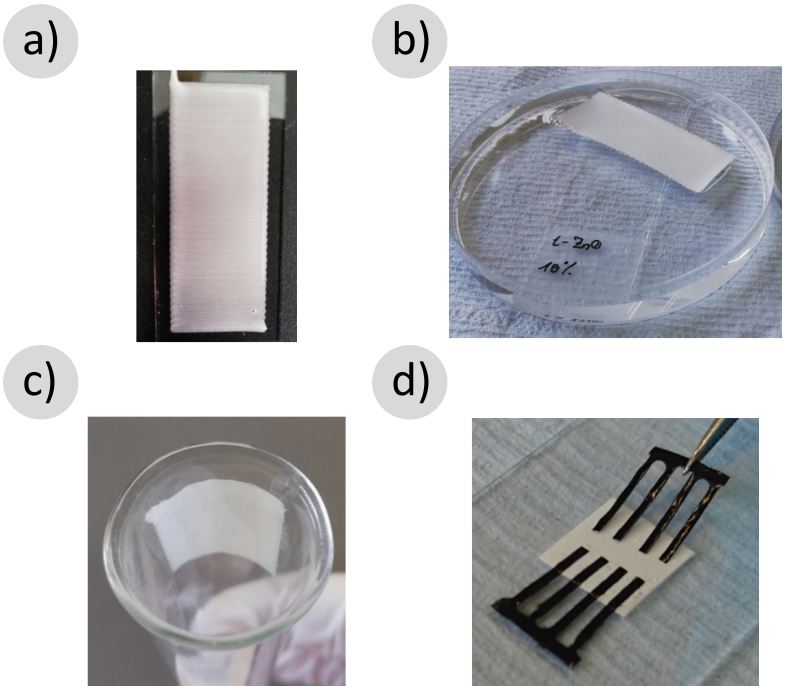

Figure 5.2: *Workflow of delaminating and re-applying EtOH/PVB based prints. a) A single layer of ink with 10 wt% ZnO is printed on a glass substrate. b) The substrate is submerged in deionized water. Due to the hydrophobic matrix the print delaminates from the glass surface. c) A part of the print is attached conformally to a round glass tube by slightly wetting its surface with ethanol. d) A sensor device is assembled by unifying parts made from ZnO and CNT inks on a standard glass slide by wetting the joints with ethanol.*

The incoming energy density E_A (in energy per unit area) of the laser towards the sample surface is calculated by the irradiance I_L and the irradiation time t_i, where the irradiance is given by the laser's power Φ and the spot size d_S, which in this case is $\approx 70\ \mu m$ in diameter in the focal plane:

$$E_A = I_L * t_i = \frac{\Phi t_i}{A} = \frac{4\Phi t_i}{\pi d_S^2} \tag{5.1}$$

While scanning over a surface with constant speed v_L, the time Δt during which the laser moves a given distance Δx is given by:

$$\Delta t = \frac{\Delta x}{v_L} \tag{5.2}$$

If it is considered that $\Delta x = d_S$ we obtain t_S, which is the time the beam irradiates a given point with its whole beam profile. Thus t_S can also be taken as the irradiation time t_i:

$$t_S = \frac{d_S}{v_L} = t_i \tag{5.3}$$

Now, if t_i is replaced with the middle term from *Equation* (5.3) we obtain an expression for the energy density, that is dependent on the process parameters:

$$\langle E_A \rangle = \frac{4\Phi}{\pi d_S v_L} \tag{5.4}$$

where Φ and v_L are the radiant power and the speed of the laser respectively, which are controllable by the computer, and d_S is the spot size, which can be increased by moving the sample surface out of the focus plane, i.e. on the Z-axis. The energy density has been replaced with the average energy density $\langle E_A \rangle$ to account for a non-homogeneous beam profile.

Equation (5.4) shows, that besides the laser power itself, both a defocus and higher head speed decrease the incoming energy density and can be utilized to tune it more precisely.
Making use of this heat treatment technique allows to obtain additional features by adjusting the regime of the parameters in *Equation* (5.4):
With low energy density, achieved by low power, fast movement and a defocused beam, a thin portion of polymeric binder has been removed from a single layer print, which will be referred to as "laser milling". Without damaging the embedded microparticles, the top portion of the layer has been stripped of its polymeric binder, exposing the functional particles, while keeping the bottom portion of the binder as mechanical support.
In *Figure 5.3* SEM micrographs are shown, indicating the effect of different speeds of the laserhead on the polymeric matrix. While no surface near binder is visible in *Figure 5.3a+b*, the microparticles in *Figure 5.3c* and *d* are respectively either partially or almost completely embedded in the binder.

The benefit of this method becomes clear when the two extreme cases are considered together:
If the microparticles are completely embedded in the polymer, the print can be delaminated, processed and re-applied, as described in *section* 5.2.1. However, the microparticles are shielded from external species such as light or gases, preventing any sensor functionality and possibly impeding electrical conductivity.
If all binder is removed, the particles are completely exposed offering large surface area, however there is no possibility to detach the print from the initial substrate, severly limiting its applicability.
By maintaining only a portion of the polymer matrix at the bottom, which is visible in *Figure 5.3e*, the benefits of both are combined, as it is possible to detach

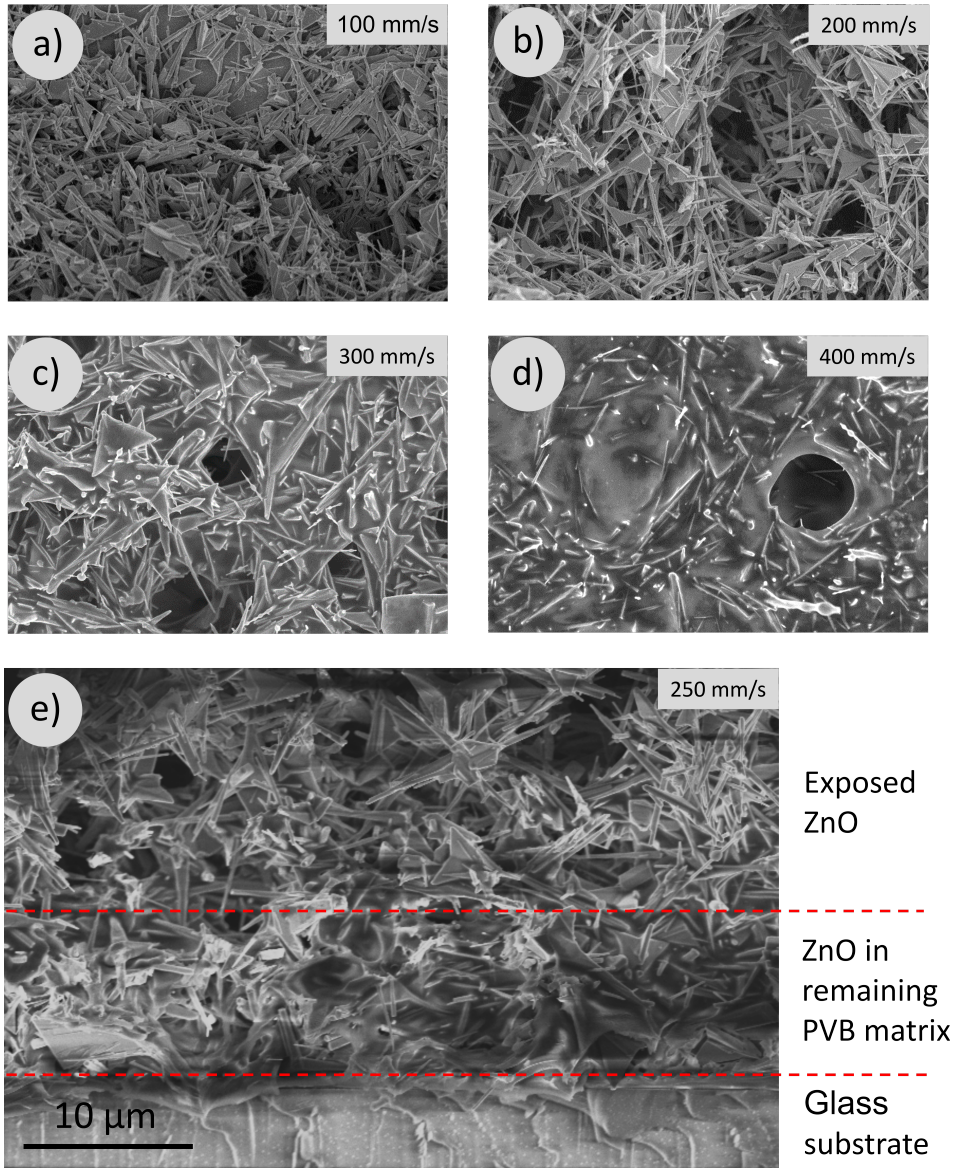

Figure 5.3: *SEM micrographs of a 10 wt% t-ZnO ink after laser milling at different speeds with 20% power and 9 mm defocus. Images c) and d) show how less of the polymeric binder has been removed for higher speeds. The scale bar in a) is valid for b-d) as well. e) shows the cross-section of a print revealing exposed ZnO at the top and embedded ZnO at the bottom portion of the print.*

and re-apply the print while the microparticles at the top portion are exposed to the surroundings, as schematically depicted in *Figure 5.4a*.
An all-printed freestanding sensor device has been fabricated by combining prints of t-ZnO as the sensor component and CNTs as the wiring with subsequent laser

milling. In *Figure 5.4b* the interface between the CNT and the ZnO region is shown in an SEM micrograph, indicating that by this gentle form of heat treatment the surface near binder could be removed without damaging the microparticles. After having been processed by laser milling the remaining polymer matrix allowed the print to be delaminated from the substrate and to bend the print to a 2.5-dimensional freestanding form, as shown in *Figure 5.4c*, while keeping its sensor functionality.

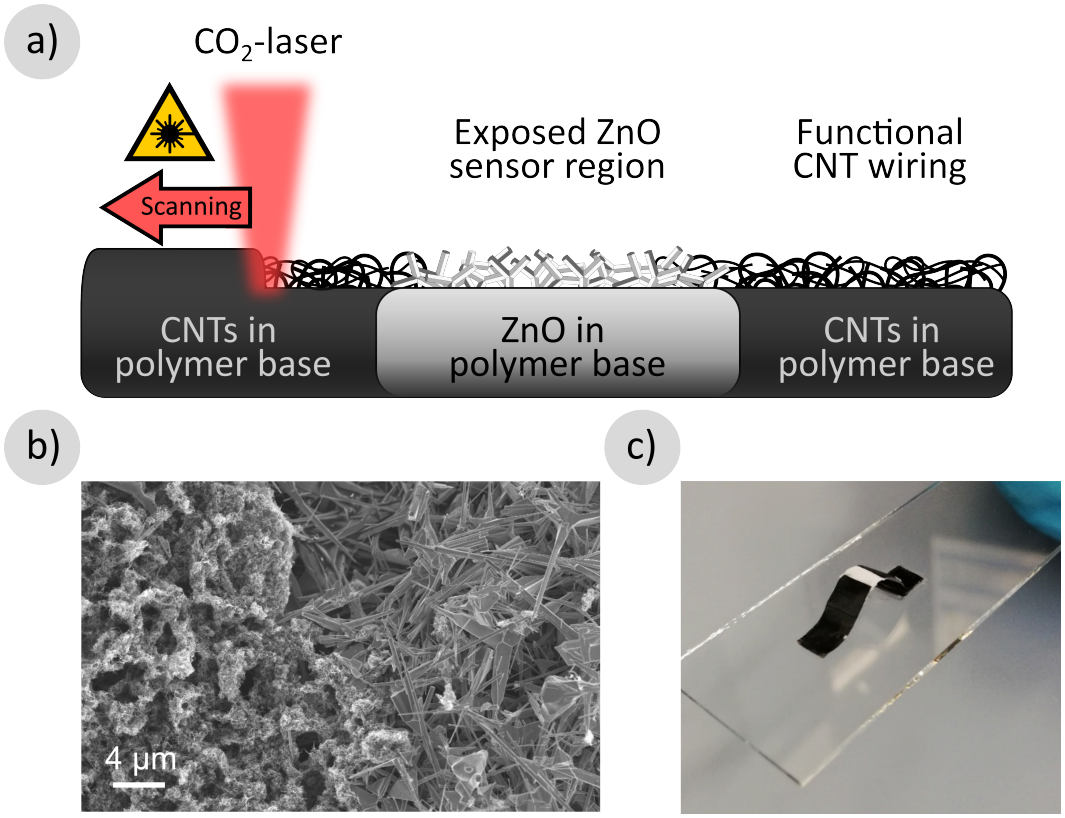

Figure 5.4: *a) Schematic of the gentle laser milling process by the example of a CNT/t-ZnO/CNT device. The laser only removes a portion of the polymeric binder. The microparticles are exposed, leading to conductive CNT wiring and a sensitive ZnO region. b) SEM micrograph of the CNT/t-ZnO interface after laser milling. No polymeric binder is visible on the surface and the microparticles are undamaged. (Image recorded by Dr. Ing. Leonard Siebert) c) An all-printed freestanding functional sensor device on a conventional glass substrate. After the gentle laser milling step the print has been delaminated from the substrate and reattached.*

5.3 Sensor characterization

In this section, the characterization of the printed sensor devices is presented. The sensors have been characterized qualitatively by measuring their current response to an applied voltage over time, with periods where they have been exposed to a suitable external stimulus, i.e. UV-light and gas molecules. The UV-response has also been measured during cyclic mechanical deformation.

5.3.1 UV Response

Experiments for the sensors' UV response have been conducted using a custom-built probing setup. Gold plated spring contacts have been used as probes placed on the sample and were connected to a computer controlled Keithley 2400 SMU for measurement readouts.
UV light has been applied as an external stimulus by a 365 nm UV-LED (LZ1-00UV00 by LED-Engin) with 1250 mW radiant flux. The setup has been enclosed in an opaque box to prevent ambient lighting conditions from affecting the measurement. The UV-LED has been attached to the box above the sample and has been supplied with a controlled DC current of 700 mA. The complete setup is shown schematically in *Figure 5.5*.

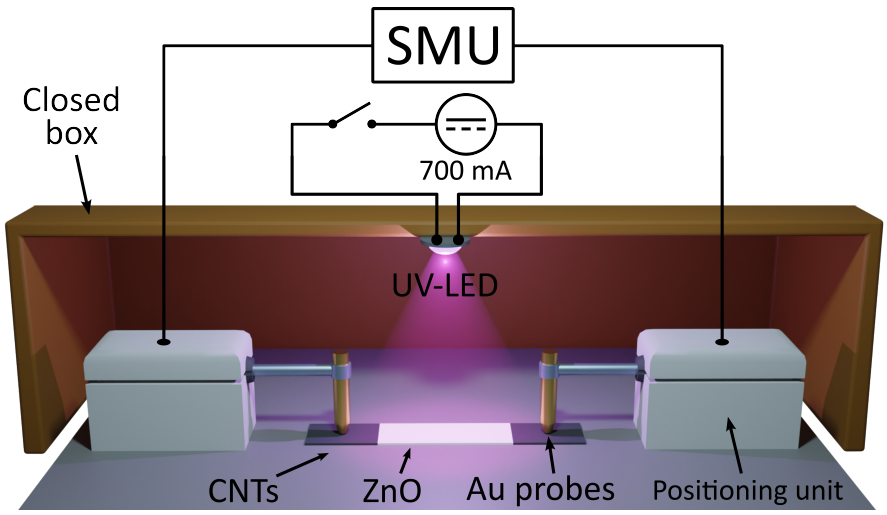

Figure 5.5: *3D schematic of a cross section of the experimental setup to characterize the printed sensors' UV response. The switch represents that the UV-LED has been turned on/off during the measurements.*

In order to ensure UV response functionality, current measurements with intermittent UV exposure have been conducted on assembled CNT/t-ZnO/CNT sensors with electrode spacings of 3, 9 and 20 *mm*. In *Figure 5.6* a measurement

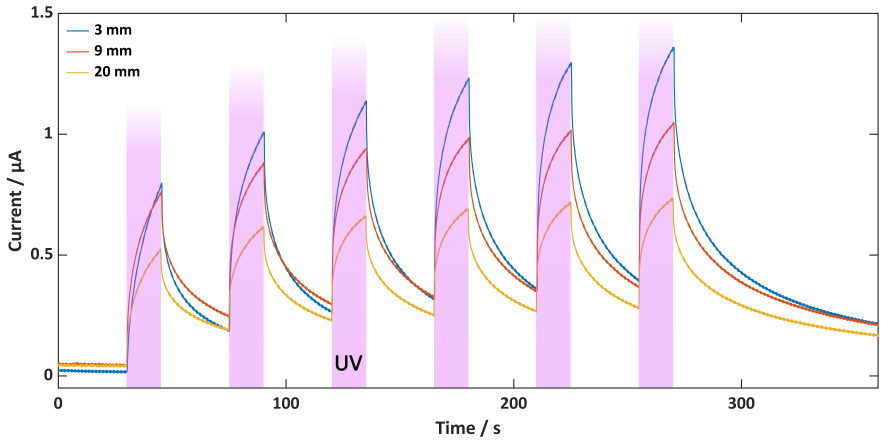

Figure 5.6: *Current measurements of three CNT/t-ZnO/CNT sensors with the given electrode spacing exposed to six UV pulses.*

is shown where the sensor has been exposed to six UV-pulses. For each pulse the UV-LED has been switched on for 15 s and off for 30 s.

The current response shows three main findings: the ZnO is functional as a sensor component towards UV-light, the CNT regions act as electrodes and wiring and the CNTs are sufficiently interfaced with the ZnO to allow a significant current flow.

The time constants of the UV response have been determined by fitting the rising and falling edges of each pulse with the model equation

$$f(t) = A * exp\left(\frac{-t}{\tau_1}\right) + B * exp\left(\frac{-t}{\tau_2}\right) + C \tag{5.5}$$

where τ_1 and τ_2 are the time constants and A, B and C are constant parameters. The fit has been performed using *MATLAB* 2022a.

The resulting values are shown in *Table 5.2* together with the respective relative current increase after 15 s of exposure. The decay time, also referred to as the recovery time, is in the order of magnitude of other reported ZnO-based sensors[170].

Table 5.2: *UV response merits for the current measurement shown in Figure 5.6.*

Spacing [mm]	3	9	20
$\tau_{\mathbf{1,2rise}}$ **[s]**	0.5, 10	0.5, 10	0.5, 10
$\tau_{\mathbf{1,2decay}}$ **[s]**	1.1, 15	1.1, 15	1.1, 15
$\mathbf{I_{UV}/I_{dark}}$	3.8 ± 0.89	3.0 ± 0.18	2.3 ± 0.39

The current ratios increase with the electrode spacing indicating that the serial resistance of the t-ZnO plays a significant role for the sensor response. However, the initial dark currents as well as the ratios normalized to their spacings are inconsistent with a purely linear relation. Factors impacting the sensor resistance among others are the distribution of the ZnO tetrapods and interfacing of their arms. The next section treats the impact of varying contact points among the tetrapod arms by the example of a mechanically strained sensor device.

5.3.2 Pulsed UV Response under Mechanical Cycling

In order to account for the sensors' flexibility, the operation of the printed sensors has been investigated, when subjected to mechanical deformation[1].
A CNT/t-ZnO/CNT sensor has been assembled and laser milled as shown in *Figure 5.2d* and *Figure 5.4a* respectively. The device has been mounted into the clamps of a custom-built electro-mechanical testing machine, where the clamps also serve as the electrical contacts. The clamps' relative position has been cycled between -2 mm and +2 mm, where negative values represent the tensile direction and positive values the compressive direction.

Simultaneously, the sensor has been illuminated with a UV-LED pulsed with 1 Hz via a HP 33120A function generator. The LED has been identical to the one described in *section* 5.3.1. Current readouts have been recorded via a computer controlled *Keithley 2400* SMU. The setup is depicted schematically in *Figure 5.7a*. The current response has been measured over a time of 2000 s and is shown with three different data windows in *Figure 5.7c*. The long-term behaviour in plot ① shows a saturation of conductivity with prolonged exposure, which is indicated by the moving average (deep blue line). Plot ② - showing a zoomed in view of the data in plot ① - clarifies the impact of the mechanical cycling. It indicates that a compressive deformation causes a drop in conductivity. Since the effect is completely reversible it is proposed that there is no mechanical damage to the sensor but instead that the arms of the ZnO tetrapods lose contact to one another due to the bending.
Further zooming in, as given in plot ③, the current oscillations reflect the response to the pulsed UV light (1 Hz), showing that the sensor functionality is retained upon straining, which makes this sensor approach suitable for applications where mechanical flexibility is a core requirement e.g. for electronic skins[171, 172].

[1] Adapted from P. Schadte, R. Madurawala et *al.*, 2024, *Flexible, fast and freestanding UV sensors by 3D-printing of networked materials*, submitted

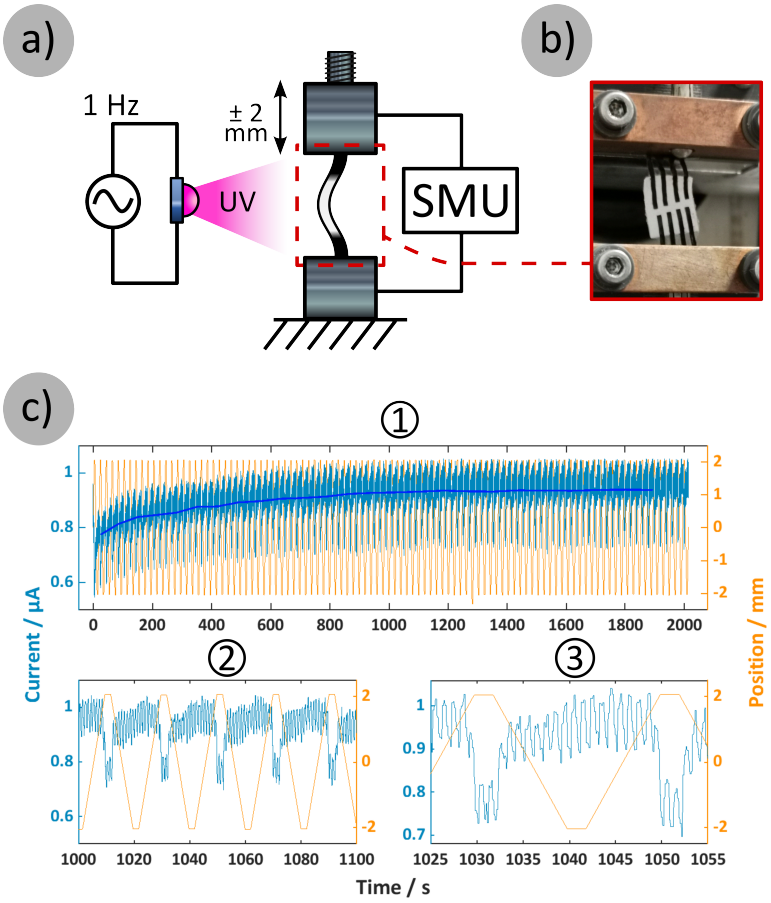

Figure 5.7: *Setup and results of the electro-mechanical experiment of a printed and delaminated CNT/t-ZnO/CNT sensor device. a) Schematic of the experimental setup. b) Photograph of the sensor mounted into the electro-mechanical clamps. c) Current measurement, with three plots showing different data windows to display various effects, affecting the response. ①: Complete measurement, showing long-term exposure dependency. ②: Data window showing the effect of the mechanical cycles. ③: Data window showing the response to the 1 Hz UV pulses.*

5.3.3 Gas response

Sensing of surrounding gases is an important aspect of health and security measures, e.g. for monitoring the concentration of chemical species in workspace or storage areas. As an example for medical relevance, it has been shown that the concentration of acetone in the human breath is an indicator for diabetic ketoacidosis[173].
In this context, the approach of the 3D-printed sensor has been applied to other systems of metal oxide particles: in [126] and [143] Cu as well as a mixture of

Cu and Fe particles respectively have been printed and thermally oxidized forming either $CuO/Cu_2O/Cu$ or CuO/Fe_2O_3 heterojunctions. The oxidation yielded needle-like nanostructures spreading out from the particles severely increasing the total sensor area as well as contact area between particles, both of which are beneficial merits for sensor devices (see *Figure 5.8a-d*).

The printed devices have been characterized towards their response to acetone

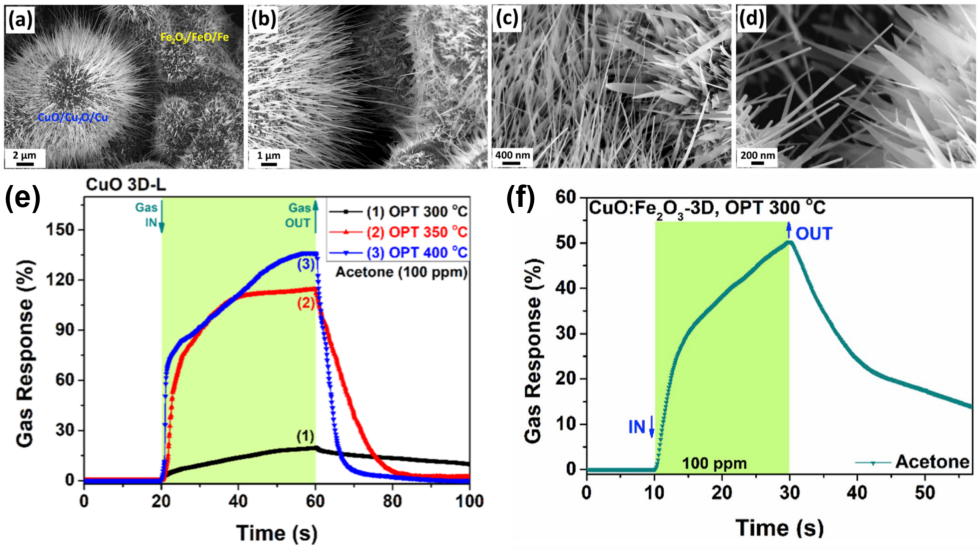

Figure 5.8: *a-d) SEM micrographs of the junctions between CuO and Fe_2O_3 microparticles with nano-needles. e+f) Resistive gas responses of 3D-printed sensor devices to 100 ppm acetone vapour. Reprinted with permission from [126] and [143].*

vapour to which they showed a response of up to 150 % at 100 ppm, in terms of resistance increase relative to its resistance in ambient air, as displayed in *Figure 5.8e+f*. The sensing mechanism is treated in *section* 2.5.2.

The results indicate that the applicability of the fabrication route expands to gas sensor components as well.

Furthermore, the ability to tune a sensor's properties is an important aspect for the optimization of its operation in specific environments. For metal oxide based sensors, this can be achieved by doping the sensor material with certain elements, or deposit additional nanoparticles on the sensor surface.

Important merits for a sensor operation are:

- Sensitivity, the extent of response with respect to the stimulus strength. A high sensitivity allows to resolve even small changes in stimulus.

- Selectivity, determining how well the response is limited to a specific stimulus species. A good selectivity allows conclusive signal interpretation.

- Stability, how reliable the sensor operates and retains its behaviour under changing environmental conditions.

The effect of doping and nanoparticle decoration on these merits of metal-oxide based sensors has been reported for a wide variety of material systems. A selection will be given in *Table 5.3*, which has been excerpted from [136].
The diversity of materials and effects indicates how the material space for the

Table 5.3: *Overview over a selection of metal oxide systems and the effect of the given doping and nanoparticle decoration on the sensor performance.*

Base System	**Nanoparticles**	**Effect**	**Ref.**
ZnO:Fe	AgO/Ag	Enhanced sensitivity to ethanol vapour	[174]
ZnO:Ag	Ag	Enhanced humidity stability	[175]
ZnO:Ag	AgAu	Enhanced sensitivity for VOCs	[176]
ZnO:Ag	AgPt	Enhanced selectivity for hydrogen	[176]
TiO_2	Ag, Au, AgAu, AgPt	Enhanced selectivity for various gases	[177, 178]
ZnO:Eu	Pd	Decrease of operating temperature to RT	[179]
ZnO:Pd	PdO	Enhanced selectivity and sensitivity for hydrogen	[180, 181]
SnO_2	Zn_2SO_4	Enhanced sensitivity for ethanol at RT	[182]

additive manufacturing of sensors is further expanded when dopants, decorators as well as mixtures of those are considered.

5.4 Conclusion

This chapter has discussed AM in general and DIW specifically as a tool to fabricate pre-designed functional components. DIW has been established as a fabrication route for micro- and nanoparticle based sensor devices, which has been demonstrated by the example of UV-sensors with t-ZnO particles and gas sensors with CuO as well as CuO/Fe_2O_3. Laser milling as a localized, well controllable

heat treatment yielded free-standing, flexible sensors with an exposed, functional top layer. Keeping the polymer base as structural support allowed for conformal or complex shaped devices. The UV response was retained under mechanical deformation, which is especially interesting in the context of electronic skin applications[171, 172].
DIW represents an ideal method to explore functional small-body materials as a platform for the design and fabrication of functional parts. Its capabilities to process any mixture of particles as well as doping and functionalization of particle species further increase the degrees of freedom, which perfectly matches with the quick iteration cycles to allow for rapid research and development of printed components.

Concluding this Thesis

This thesis is dedicated to the search for material systems and methods that are suitable to create physical substrates for *in-materia* approaches to neuromorphic computing. The search is motivated by features and mechanisms of biological neural assemblies, such as plasticity, three-dimensional connectivity, network hierarchy and oscillatory interactions, from which their astounding capabilities and energy efficiency originates.
In order to support the understanding of the results presented in this work, three aspects of a neuromorphic system have been defined, to which the material systems discussed are allocated: The component space, representing individual building blocks of a neural assembly, the network space representing how the components are interconnected to form a network and mechanisms to change its topology as well as the design space representing regions of a neural assembly that are based on a pre-determined blueprint with specific functionality, instead of being shaped dynamically by plasticity.

In *Chapter* 3 as part of the component space it has been described how a new lateral memristor concept has been developed and realized.
In contrast to a stack of thin films, which is the common configuration for memristive devices, the lateral orientation has been motivated by the exposure of the reactive switching sites to external investigative signals as well as stimuli.
A fabrication route has been established to achieve the nano-scaled distances required for resistive switching phenomena, that avoids sophisticated clean-room dependent equipment. Instead, a sparse network of CNTs has been deposited from a dispersion via facile methods such as ultrasonication and spin coating. It has shown to act as a mediator between external electrodes and the nanoscale by forming a conductive network but providing nanometer sized gaps, where a sparse film of AgAu nanoparticles yielded resistive ECM-type switching.
The switching was a hybrid of diffusive and bipolar switching with a retention time in the regime of several seconds. The limited lifetime has been attributed to the availability of Ag from the participating nanoparticles but also has shown to be tunable via the SET pulse width.
With its second-time retention, this memristor concept fills the middle ground between non-volatile memory cells and highly volatile selector devices as a biologi-

cally plausible short-term memory component. In contrast to volatile memristors, it is able to store information but does not need to be explicitly reset like it is necessary for non-volatile memory.
Additionally, as a tangent to the network space the facile fabrication of a sparse CNT network readily acts as a foundation for further multi-terminal applications such as reservoir computing.

Next, *Chapter* 4 addressed the search for a way to overcome static 2D wiring schemes, as these are deployed e.g. in the form of cross-bar arrays. Two material-based approaches have been presented that provide mechanisms for the dynamic three-dimensional reconfiguration of the interconnections in a network based on an external electrical input, which is inspired by the plasticity in neural assemblies. Both approaches have been dedicated to the network space as they provide mechanisms to dynamically alter a network's topology.
The first one presented how directed metal filaments have been grown in a liquid matrix between active electrodes via electrochemical metallization, in this specific case referred to as "redox-wiring". In contrast to *Chapter* 3 where ECM has been utilized on the nanoscale, redox-wiring is capable of forming metallic connections from the micro- up to the millimeter scale, making the process inherently capable of operating in hierarchical configurations.
An established filament increased the conductivity between participating electrodes significantly upon contact. Also it kept rising further with continuous excitation. Thus, with the conductivity considered as the connection strength, this material system provides the capability for network plasticity by changing its topology via a fully dynamic input. Since the approach is completely bottom-up, instead of having pre-built components only changing its state, it solely allocates material to where it is demanded, while also allowing for a truly three-dimensional wiring.
In addition to the general plasticity, redox-wiring exhibited distance-dependent guidance, a mechanism of connectome development in the brain, as well as the capability to mimic LTP of neurons by applying suitable voltage pulses as the excitation.
To address the dynamics in neural networks, which is expressed by the oscillating action potentials of neurons, redox-wiring has been deployed as a coupling mechanism for relaxation-type oscillators. The oscillators synchronized when interconnected by the generated filaments and desynchronized again upon the filaments' collapse emulating the pulse-coupling of neural oscillators, which is considered to be a basal mechanism for higher brain functions.
The second approach discussed a network of dielectric ZnO nanoparticles, that have been deposited on a grid of electrodes in a liquid matrix. The network has been reshaped collectively by shifting the particles via dielectrophoresis according to an alternating electrical input to the electrodes. The topology of the network

has been considered to be represented by the particle density along a given path, so that a drift of particles at a given point alters the connection between neighbouring electrodes. It has been confirmed that a connection's strength could be evaluated via the UV-sensitivity of the ZnO particles along it.
Thus, this process yielded a plasticity of the inherent features of the particle species, which in this case have been the sensitive properties of ZnO. This adds additional degrees of freedom to the plasticity in the form of functionality beyond electrical conductivity.

Finally, in *Chapter* 5 the design space has been addressed by discussing additive manufacturing as a tool to design and fabricate particle based sensor devices with the focus on DIW, which deposits particles dispersed in a highly viscous ink. Deploying DIW as a fabrication method offered many degrees of freedom with respect to fabricated geometries as well as employed particle species, which has been demonstrated by the fabrication of CNT/t-ZnO/CNT UV-sensors as well as gas sensors made of CuO/Fe_2O_3 heterostructures in various geometries. The presented laser milling technique provided a highly localized heat treatment that allowed to remove a well controllable amount of polymeric binder from printed layers, exposing the functional particles to external stimuli while keeping a stable polymeric base for mechanical support. The combination offered a facile way to produce flexible sensor devices that can be re-applied conformally to surfaces of any shape or kept as free-standing. Utilizing this flexibility, the sensor features have been retained under mechanical deformation, making this type of sensors interesting for electronic skin applications.
Moreover, the doping of sensor materials as well as a decoration with nanoparticles has been discussed as an additional step to expand and adjust the sensor properties e.g. to address different environmental conditions or improve the sensor performance.

Overall, the results of this work presented physical substrates for *in-materia* approaches providing a promising foundation to expand on silicon-based circuits for neuromorphic computing. The capability of mimicking features of biological neural networks via the interactions and properties of material systems incentivizes to combine them with existing CMOS-technology as mutual complements, whereas thorough circuit models will have to be developed to be able of integration. This work contributes new material platforms to *in-materia* computing in order to push towards a synergistic concurrence of existing and future facets of neuromorphic computing.

List of Publications

First Authorships

- Maik-Ivo Terasa et al. "Pathways towards truly brain-like computing primitives". In: *Materials Today* (2023). ISSN: 13697021. DOI: 10.1016/j.mattod.2023.07.019
- Maik-Ivo Terasa et al. "Smart Sensor Arrays". In: *Bio-Inspired Information Pathways*. Ed. by Martin Ziegler, Thomas Mussenbrock, and Hermann Kohlstedt. Vol. 16. Springer Series on Bio- and Neurosystems. Cham: Springer International Publishing, 2023, pp. 265–285. ISBN: 978-3-031-36704-5. DOI: 10.1007/978-3-031-36705-2{_}11
- Maik-Ivo Terasa et al. "Sparse CNT networks with implanted AgAu nanoparticles: A novel memristor with short-term memory bordering between diffusive and bipolar switching". In: *PloS one* 17.3 (2022), e0264846. DOI: 10.1371/journal.pone.0264846

Co-Authorships

- Oleg Lupan et al. "Additive Manufacturing as a Means of Gas Sensor Development for Battery Health Monitoring". In: *Chemosensors* 9.9 (2021), p. 252. DOI: 10.3390/chemosensors9090252
- Cristian Lupan et al. "Pd-Functionalized ZnO: Eu Columnar Films for Room-Temperature Hydrogen Gas Sensing: A Combined Experimental and Computational Approach". In: *ACS applied materials & interfaces* 12.22 (2020), pp. 24951–24964. DOI: 10.1021/acsami.0c02103
- Leonard Siebert et al. "Facile fabrication of semiconducting oxide nanostructures by direct ink writing of readily available metal microparticles and their application as low power acetone gas sensors". In: *Nano Energy* 70.2 (2020), p. 104420. ISSN: 22112855. DOI: 10.1016/j.nanoen.2019.104420

- Alexander Vahl et al. "Surface functionalization of ZnO: Ag columnar thin films with AgAu and AgPt bimetallic alloy nanoparticles as an efficient pathway for highly sensitive gas discrimination and early hazard detection in batteries". In: *Journal of Materials Chemistry A* 8.32 (2020), pp. 16246–16264. ISSN: 2050-7488. DOI: 10.1039/d0ta03224g

- Fabian Schütt et al. "Conversionless efficient and broadband laser light diffusers for high brightness illumination applications". In: *Nature communications* 11.1 (2020), p. 1437. DOI: 10.1038/s41467-020-14875-z

- Leonard Siebert et al. "3D-Printed Chemiresistive Sensor Array on Nanowire CuO/Cu2O/Cu Heterojunction Nets". In: *ACS applied materials & interfaces* (2019). DOI: 10.1021/acsami.9b04385

- Nicolai Ababii et al. "Effect of noble metal functionalization and film thickness on sensing properties of sprayed TiO2 ultra-thin films". In: *Sensors and Actuators A: Physical* 293 (2019), pp. 242–258. ISSN: 09244247. DOI: 10.1016/j.sna.2019.04.017

- Lidia Ghimpu et al. "Individual CdS-covered aerographite microtubes for room temperature VOC sensing with high selectivity". In: *Materials Science in Semiconductor Processing* 100.23 (2019), pp. 275–282. ISSN: 13698001. DOI: 10.1016/j.mssp.2019.05.013

- Oleg Lupan et al. "Room temperature gas nanosensors based on individual and multiple networked Au-modified ZnO nanowires". In: *Sensors and Actuators B: Chemical* 299 (2019), p. 126977. ISSN: 09254005. DOI: 10.1016/j.snb.2019.126977

- Vasile Postica et al. "Tuning ZnO Sensors Reactivity toward Volatile Organic Compounds via Ag Doping and Nanoparticle Functionalization". In: *ACS applied materials & interfaces* 11.34 (2019), pp. 31452–31466. DOI: 10.1021/acsami.9b07275

- Muchao Qu et al. "Structure changes of aligned carbon nanotubes in thermoplastics below percolation revealed by impedance spectroscopy". In: *Applied Nanoscience* 8.8 (2018), pp. 2071–2075. ISSN: 2190-5509. DOI: 10.1007/s13204-018-0865-y

References

[1] Michael J. Russell and A. J. Hall. "The emergence of life from iron monosulphide bubbles at a submarine hydrothermal redox and pH front". In: *Journal of the Geological Society* 154.3 (1997), pp. 377–402. ISSN: 0016-7649. DOI: 10.1144/gsjgs.154.3.0377.

[2] Timothy Shanahan. *The evolution of Darwinism: Selection, adaptation, and progress in evolutionary biology*. Cambridge, UK and New York: Cambridge University Press, 2004. ISBN: 0521834139.

[3] Gáspár Jékely. "Origin and early evolution of neural circuits for the control of ciliary locomotion". In: *Proceedings. Biological sciences* 278.1707 (2011), pp. 914–922. DOI: 10.1098/rspb.2010.2027.

[4] Judith P. Armitage. "Behavioural responses of bacteria to light and oxygen". In: *Archives of microbiology* 168.4 (1997), pp. 249–261. ISSN: 0302-8933. DOI: 10.1007/s002030050496.

[5] Aurèle Boussard et al. "Adaptive behaviour and learning in slime moulds: the role of oscillations". In: *Philosophical transactions of the Royal Society of London. Series B, Biological sciences* 376.1820 (2021), p. 20190757. DOI: 10.1098/rstb.2019.0757.

[6] Kerry Hinton et al. "Power consumption and energy efficiency in the internet". In: *IEEE Network* 25.2 (2011), pp. 6–12. ISSN: 0890-8044. DOI: 10.1109/MNET.2011.5730522.

[7] Andrea Zanella et al. "Internet of Things for Smart Cities". In: *IEEE Internet of Things Journal* 1.1 (2014), pp. 22–32. ISSN: 2327-4662. DOI: 10.1109/JIOT.2014.2306328.

[8] John Backus. "Can programming be liberated from the von Neumann style?" In: *Communications of the ACM* 21.8 (1978), pp. 613–641. ISSN: 0001-0782. DOI: 10.1145/359576.359579.

[9] Mohamed Shaafiee, Rajasvaran Logeswaran, and Andrew Seddon. "Overcoming the limitations of von Neumann architecture in big data systems". In: *Proceedings of the 7th International Conference Confluence 2017 on Cloud Computing, Data Science and Engineering*. Ed. by Abhay Bansal and Abhishek Singhal. Piscataway, NJ: IEEE, 2017, pp. 199–203. ISBN: 978-1-5090-3519-9. DOI: 10.1109/CONFLUENCE.2017.7943149.

[10] Hans Bode et al. "Quantitative analysis of cell types during growth and morphogenesis in Hydra". In: *Wilhelm Roux' Archiv fur Entwicklungsmechanik der Organismen* 171.4 (1973), pp. 269–285. ISSN: 0043-5546. DOI: 10.1007/BF00577725.

[11] Ennio Pannese. "Morphological changes in nerve cells during normal aging". In: *Brain structure & function* 216.2 (2011), pp. 85–89. DOI: 10.1007/s00429-011-0308-y.

[12] Alan L. Hodgkin and Andrew F. Huxley. "A quantitative description of membrane current and its application to conduction and excitation in nerve". In: *The Journal of physiology* 117.4 (1952), pp. 500–544. DOI: 10.1113/jphysiol.1952.sp004764.

[13] Leon Chua. "Memristor, Hodgkin-Huxley, and edge of chaos". In: *Nanotechnology* 24.38 (2013), p. 383001. ISSN: 0957-4484. DOI: 10.1088/0957-4484/24/38/383001.

[14] Shashi Kant Singh, Shubham Kumar, and Pawan Singh Mehra. "Chat GPT & Google Bard AI: A Review". In: *2023 International Conference on IoT, Communication and Automation Technology (ICICAT)*. IEEE, 2023, pp. 1–6. ISBN: 979-8-3503-0282-0. DOI: 10.1109/ICICAT57735.2023.10263706.

[15] Nassim Dehouche and Kullathida Dehouche. "What's in a text-to-image prompt? The potential of stable diffusion in visual arts education". In: *Heliyon* 9.6 (2023), e16757. ISSN: 2405-8440. DOI: 10.1016/j.heliyon.2023.e16757.

[16] Varun Gulshan et al. "Development and Validation of a Deep Learning Algorithm for Detection of Diabetic Retinopathy in Retinal Fundus Photographs". In: *JAMA* 316.22 (2016), pp. 2402–2410. DOI: 10.1001/jama.2016.17216.

[17] Florian Prayer et al. "Künstliche Intelligenz in der Bildgebung der Lunge". In: *Der Radiologe* 60.1 (2020), pp. 42–47. DOI: 10.1007/s00117-019-00611-2.

[18] Scott Mayer McKinney et al. "International evaluation of an AI system for breast cancer screening". In: *Nature* 577.7788 (2020), pp. 89–94. DOI: 10.1038/s41586-019-1799-6.

[19] Yann LeCun, Yoshua Bengio, and Geoffrey Hinton. "Deep learning". In: *Nature* 521.7553 (2015), pp. 436–444. DOI: 10.1038/nature14539.

[20] Ajay Shrestha and Ausif Mahmood. "Review of Deep Learning Algorithms and Architectures". In: *IEEE Access* 7 (2019), pp. 53040–53065. DOI: 10.1109/ACCESS.2019.2912200.

[21] Adnan Mehonic and Anthony J. Kenyon. "Brain-inspired computing needs a master plan". In: *Nature* 604.7905 (2022), pp. 255–260. DOI: 10.1038/s41586-021-04362-w.

[22] Mark E. Dean and Christopher Daffron. "A VLSI Design for Neuromorphic Computing". In: *2016 IEEE Computer Society Annual Symposium on VLSI (ISVLSI)*. IEEE, 2016, pp. 87–92. ISBN: 978-1-4673-9039-2. DOI: 10.1109/ISVLSI.2016.81.

[23] Harry J.M. Veendrick. *Nanometer CMOS ICs*. Cham: Springer International Publishing, 2017. ISBN: 978-3-319-47595-0. DOI: 10.1007/978-3-319-47597-4.

[24] Paul A. Merolla et al. "Artificial brains. A million spiking-neuron integrated circuit with a scalable communication network and interface". In: *Science (New York, N.Y.)* 345.6197 (2014), pp. 668–673. DOI: 10.1126/science.1254642.

[25] Tommaso Zanotti, Francesco Maria Puglisi, and Paolo Pavan. "Smart Logic-in-Memory Architecture for Low-Power Non-Von Neumann Computing". In: *IEEE Journal of the Electron Devices Society* 8 (2020), pp. 757–764. DOI: 10.1109/JEDS.2020.2987402.

[26] Xingqi Zou et al. "Breaking the von Neumann bottleneck: architecture-level processing-in-memory technology". In: *Science China Information Sciences* 64.6 (2021). ISSN: 1674-733X. DOI: 10.1007/s11432-020-3227-1.

[27] Julian F. Miller, Simon L. Harding, and Gunnar Tufte. "Evolution-in-materio: evolving computation in materials". In: *Evolutionary Intelligence* 7.1 (2014), pp. 49–67. ISSN: 1864-5909. DOI: 10.1007/s12065-014-0106-6.

[28] Gianluca Milano et al. "In materia reservoir computing with a fully memristive architecture based on self-organizing nanowire networks". In: *Nature materials* 21.2 (2022), pp. 195–202. ISSN: 1476-1122. DOI: 10.1038/s41563-021-01099-9.

[29] Ian T. Vidamour et al. "Reconfigurable reservoir computing in a magnetic metamaterial". In: *Communications Physics* 6.1 (2023). DOI: 10.1038/s42005-023-01352-4.

[30] Matthew Dale et al. "Reservoir computing in materio: A computational framework for in materio computing". In: *2017 International Joint Conference on Neural Networks (IJCNN)*. IEEE, 2017, pp. 2178–2185. ISBN: 978-1-5090-6182-2. DOI: 10.1109/IJCNN.2017.7966119.

[31] Matthew D. Pike et al. "Atomic Scale Dynamics Drive Brain-like Avalanches in Percolating Nanostructured Networks". In: *Nano letters* 20.5 (2020), pp. 3935–3942. DOI: 10.1021/acs.nanolett.0c01096.

[32] Zdenka Kuncic and Tomonobu Nakayama. "Neuromorphic nanowire networks: principles, progress and future prospects for neuro-inspired information processing". In: *Advances in Physics: X* 6.1 (2021). ISSN: 2374-6149. DOI: 10.1080/23746149.2021.1894234.

[33] Christopher S. Dunham et al. "Nanoscale neuromorphic networks and criticality: a perspective". In: *Journal of Physics: Complexity* 2.4 (2021), p. 042001. DOI: 10.1088/2632-072X/ac3ad3.

[34] Niko Carstens et al. "Brain-like critical dynamics and long-range temporal correlations in percolating networks of silver nanoparticles and functionality preservation after integration of insulating matrix". In: *Nanoscale advances* 4.15 (2022), pp. 3149–3160. DOI: 10.1039/D2NA00121G.

[35] Duncan J. Watts and Steven H. Strogatz. "Collective dynamics of 'small-world' networks". In: *Nature* 393.6684 (1998), pp. 440–442. DOI: 10.1038/30918.

[36] Kaixuan Sun, Jingsheng Chen, and Xiaobing Yan. "The Future of Memristors: Materials Engineering and Neural Networks". In: *Advanced Functional Materials* 31.8 (2021). DOI: 10.1002/adfm.202006773.

[37] Ruopeng Wang et al. "Recent Advances of Volatile Memristors: Devices, Mechanisms, and Applications". In: *Advanced Intelligent Systems* 2.9 (2020). ISSN: 2640-4567. DOI: 10.1002/aisy.202000055.

[38] Qiangfei Xia and J. Joshua Yang. "Memristive crossbar arrays for brain-inspired computing". In: *Nature materials* 18.4 (2019), pp. 309–323. ISSN: 1476-1122. DOI: 10.1038/s41563-019-0291-x.

[39] Leon O. Chua. "Memristor-The missing circuit element". In: *IEEE Transactions on Circuit Theory* 18.5 (1971), pp. 507–519. ISSN: 0018-9324. DOI: 10.1109/TCT.1971.1083337.

[40] Leon O. Chua and Sung Mo Kang. "Memristive devices and systems". In: *Proceedings of the IEEE* 64.2 (1976), pp. 209–223. ISSN: 0018-9219. DOI: 10.1109/PROC.1976.10092.

[41] Dmitri B. Strukov et al. "The missing memristor found". In: *Nature* 453.7191 (2008), pp. 80–83. DOI: 10.1038/nature06932.

[42] Takenori Fujii et al. "Hysteretic current–voltage characteristics and resistance switching at an epitaxial oxide Schottky junction SrRuO3/SrTi0.99Nb0.01O3". In: *Applied Physics Letters* 86.1 (2005), p. 012107. ISSN: 0003-6951. DOI: 10.1063/1.1845598.

[43] A. Beck et al. “Reproducible switching effect in thin oxide films for memory applications”. In: *Applied Physics Letters* 77.1 (2000), pp. 139–141. ISSN: 0003-6951. DOI: 10.1063/1.126902.

[44] Masanori Hosomi et al. “A novel nonvolatile memory with spin torque transfer magnetization switching: spin-ram”. In: *IEEE InternationalElectron Devices Meeting, 2005. IEDM Technical Digest.* IEEE, 2005, pp. 459–462. ISBN: 0-7803-9268-X. DOI: 10.1109/IEDM.2005.1609379.

[45] James F. Scott. “Applications of modern ferroelectrics”. In: *Science (New York, N.Y.)* 315.5814 (2007), pp. 954–959. DOI: 10.1126/science.1129564.

[46] Vincent Garcia and Manuel Bibes. “Ferroelectric tunnel junctions for information storage and processing”. In: *Nature communications* 5 (2014), p. 4289. DOI: 10.1038/ncomms5289.

[47] David C. Wright et al. “Arithmetic and biologically-inspired computing using phase-change materials”. In: *Advanced materials (Deerfield Beach, Fla.)* 23.30 (2011), pp. 3408–3413. DOI: 10.1002/adma.201101060.

[48] Marco Cassinerio, Nicola Ciocchini, and Daniele Ielmini. “Logic computation in phase change materials by threshold and memory switching”. In: *Advanced materials (Deerfield Beach, Fla.)* 25.41 (2013), pp. 5975–5980. DOI: 10.1002/adma.201301940.

[49] Jyrki Lappalainen, Janos Mizsei, and M. Huotari. “Neuromorphic thermal-electric circuits based on phase-change VO 2 thin-film memristor elements”. In: *Journal of Applied Physics* 125.4 (2019), p. 044501. ISSN: 0021-8979. DOI: 10.1063/1.5037990.

[50] Deepti Chaudhary et al. “Bipolar resistive switching and nonvolatile memory effect in poly (3-hexylthiophene) –carbon nanotube composite films”. In: *Carbon* 130 (2018), pp. 553–558. ISSN: 00086223. DOI: 10.1016/j.carbon.2018.01.058.

[51] Paola Russo, Ming Xiao, and Norman Y. Zhou. “Carbon nanowalls: A new material for resistive switching memory devices”. In: *Carbon* 120 (2017), pp. 54–62. ISSN: 00086223. DOI: 10.1016/j.carbon.2017.05.004.

[52] Yanmei Sun et al. “Logic Gate Functions Built with Nonvolatile Resistive Switching and Thermoresponsive Memory Based on Biologic Proteins”. In: *The journal of physical chemistry letters* 10.24 (2019), pp. 7745–7752. DOI: 10.1021/acs.jpclett.9b03238.

[53] Lu Wang, Wenhao Li, and Dianzhong Wen. “Soybean-based memristor for multilevel data storage and emulation of synaptic behavior”. In: *Microelectronic Engineering* 267-268 (2023), p. 111911. ISSN: 01679317. DOI: 10.1016/j.mee.2022.111911.

[54] Tao Guo et al. “From Memristive Materials to Neural Networks”. In: *ACS applied materials & interfaces* 12.49 (2020), pp. 54243–54265. DOI: 10.1021/acsami.0c10796.

[55] Yibo Li et al. “Review of memristor devices in neuromorphic computing: Materials sciences and device challenges”. In: *Journal of Physics D: Applied Physics* 51.50 (2018), p. 503002. ISSN: 0022-3727. DOI: 10.1088/1361-6463/aade3f.

[56] Gyeong-Su Park et al. “In situ observation of filamentary conducting channels in an asymmetric Ta$_2$O5-x/TaO2-x bilayer structure”. In: *Nature communications* 4 (2013), p. 2382. DOI: 10.1038/ncomms3382.

[57] Zhongrui Wang et al. “Resistive switching materials for information processing”. In: *Nature Reviews Materials* 5.3 (2020), pp. 173–195. DOI: 10.1038/s41578-019-0159-3.

[58] Deok-Hwang Kwon et al. “Atomic structure of conducting nanofilaments in TiO2 resistive switching memory”. In: *Nature Nanotechnology* 5.2 (2010), pp. 148–153. ISSN: 1748-3395. DOI: 10.1038/nnano.2009.456.

[59] Xiaojian Zhu, Seung Hwan Lee, and Wei D. Lu. “Nanoionic Resistive–Switching Devices”. In: *Advanced Electronic Materials* 5.9 (2019), p. 1900184. DOI: 10.1002/aelm.201900184.

[60] Michael Lübben and Ilia Valov. “Active Electrode Redox Reactions and Device Behavior in ECM Type Resistive Switching Memories”. In: *Advanced Electronic Materials* 5.9 (2019), p. 1800933. DOI: 10.1002/aelm.201800933.

[61] Fang Yuan et al. “Real-Time Observation of the Electrode-Size-Dependent Evolution Dynamics of the Conducting Filaments in a SiO2 Layer”. In: *ACS nano* 11.4 (2017), pp. 4097–4104. DOI: 10.1021/acsnano.7b00783.

[62] Stephan Menzel. “Comprehensive modeling of electrochemical metallization memory cells”. In: *Journal of Computational Electronics* 16.4 (2017), pp. 1017–1037. ISSN: 1569-8025. DOI: 10.1007/s10825-017-1051-2{\#}Abs1.

[63] Stephan Menzel, Ulrich Böttger, and Rainer Waser. “Simulation of multilevel switching in electrochemical metallization memory cells”. In: *Journal of Applied Physics* 111.1 (2012), p. 014501. ISSN: 0021-8979. DOI: 10.1063/1.3673239.

[64] Pengxiao Sun et al. “Physical model of dynamic Joule heating effect for reset process in conductive-bridge random access memory”. In: *Journal of Computational Electronics* 13.2 (2014), pp. 432–438. ISSN: 1569-8025. DOI: 10.1007/s10825-013-0552-x.

[65] Stephan Menzel et al. "Simulation of polarity independent RESET in electrochemical metallization memory cells". In: *2013 5th IEEE International Memory Workshop*. IEEE, 2013, pp. 92–95. ISBN: 978-1-4673-6169-9. DOI: 10.1109/IMW.2013.6582106.

[66] Wei Wang et al. "Surface diffusion-limited lifetime of silver and copper nanofilaments in resistive switching devices". In: *Nature communications* 10.1 (2019), p. 81. DOI: 10.1038/s41467-018-07979-0.

[67] Jer-Chyi Wang et al. "High-Performance Multilevel Resistive Switching Gadolinium Oxide Memristors With Hydrogen Plasma Immersion Ion Implantation Treatment". In: *IEEE Electron Device Letters* 35.4 (2014), pp. 452–454. ISSN: 0741-3106. DOI: 10.1109/LED.2014.2304970.

[68] Wei Hu et al. "High speed and multi-level resistive switching capability of Ta2O5 thin films for nonvolatile memory application". In: *Journal of Alloys and Compounds* 676 (2016), pp. 356–360. ISSN: 09258388. DOI: 10.1016/j.jallcom.2016.03.211.

[69] Muhammad Ismail et al. "Stabilized and RESET-voltage controlled multilevel switching characteristics in ZrO2-based memristors by inserting a-ZTO interface layer". In: *Journal of Alloys and Compounds* 835 (2020), p. 155256. ISSN: 09258388. DOI: 10.1016/j.jallcom.2020.155256.

[70] Krishna Rudrapal et al. "Forming–Free, Self–Compliance, Bipolar Multi–Level Resistive Switching in WO 3–x Based MIM Device". In: *Advanced Electronic Materials* 8.11 (2022), p. 2200250. ISSN: 2199-160X. DOI: 10.1002/aelm.202200250.

[71] Hee-Dong Kim et al. "Transparent multi-level resistive switching phenomena observed in ITO/RGO/ITO memory cells by the sol-gel dip-coating method". In: *Scientific reports* 4 (2014), p. 4614. DOI: 10.1038/srep04614.

[72] Na Bai et al. "Homo-layer hafnia-based memristor with large analog switching window". In: *Applied Physics Letters* 118.4 (2021). ISSN: 0003-6951. DOI: 10.1063/5.0032556.

[73] Doo Seok Jeong et al. "Emerging memories: Resistive switching mechanisms and current status". In: *Reports on progress in physics. Physical Society (Great Britain)* 75.7 (2012), p. 076502. DOI: 10.1088/0034-4885/75/7/076502.

[74] Chaoliang Tan et al. "Non-volatile resistive memory devices based on solution-processed ultrathin two-dimensional nanomaterials". In: *Chemical Society reviews* 44.9 (2015), pp. 2615–2628. DOI: 10.1039/c4cs00399c.

[75] Daniele Ielmini and H.-S. Philip Wong. "In-memory computing with resistive switching devices". In: *Nature Electronics* 1.6 (2018), pp. 333–343. ISSN: 2520-1131. DOI: 10.1038/s41928-018-0092-2.

[76] Yogesh Sharma, Pankaj Misra, and Ram S. Katiyar. "Unipolar resistive switching behavior of amorphous YCrO3 films for nonvolatile memory applications". In: *Journal of Applied Physics* 116.8 (2014). ISSN: 0021-8979. DOI: 10.1063/1.4893661.

[77] Dao You Guo et al. "Unipolar resistive switching behavior of amorphous gallium oxide thin films for nonvolatile memory applications". In: *Applied Physics Letters* 106.4 (2015). ISSN: 0003-6951. DOI: 10.1063/1.4907174.

[78] Dmitri B. Strukov, Fabien Alibart, and R. Stanley Williams. "Thermophoresis/diffusion as a plausible mechanism for unipolar resistive switching in metal–oxide–metal memristors". In: *Applied Physics A* 107.3 (2012), pp. 509–518. ISSN: 0947-8396. DOI: 10.1007/s00339-012-6902-x.

[79] Shuang Gao et al. "Improving Unipolar Resistive Switching Uniformity with Cone-Shaped Conducting Filaments and Its Logic-In-Memory Application". In: *ACS applied materials & interfaces* 10.7 (2018), pp. 6453–6462. DOI: 10.1021/acsami.7b19586.

[80] Zhongrui Wang et al. "Memristors with diffusive dynamics as synaptic emulators for neuromorphic computing". In: *Nature materials* 16.1 (2017), pp. 101–108. ISSN: 1476-1122. DOI: 10.1038/NMAT4756.

[81] Niko Carstens et al. "Neuronal–like Irregular Spiking Dynamics in Highly Volatile Memristive Intermediate–scale AgPt–Nanoparticle Assemblies". In: *Particle & Particle Systems Characterization* 40.3 (2023), p. 2200131. ISSN: 09340866. DOI: 10.1002/ppsc.202200131.

[82] Hae Jin Kim et al. "Fabrication of a Cu–Cone–Shaped Cation Source Inserted Conductive Bridge Random Access Memory and Its Improved Switching Reliability". In: *Advanced Functional Materials* 29.8 (2019). DOI: 10.1002/adfm.201806278.

[83] Jonathan Spring et al. "Toward Controlling Filament Size and Location for Resistive Switches via Nanoparticle Exsolution at Oxide Interfaces". In: *Small (Weinheim an der Bergstrasse, Germany)* 16.41 (2020), e2003224. DOI: 10.1002/smll.202003224.

[84] Chloé Minnai et al. "Facile fabrication of complex networks of memristive devices". In: *Scientific Reports* 7.1 (2017), p. 7955. ISSN: 2045-2322. DOI: 10.1038/s41598-017-08244-y.

[85] Byung Joon Choi et al. "Electrical performance and scalability of Pt dispersed SiO2 nanometallic resistance switch". In: *Nano letters* 13.7 (2013), pp. 3213–3217. DOI: 10.1021/nl401283q.

[86] Alexander Vahl et al. "Diffusive Memristive Switching on the Nanoscale, from Individual Nanoparticles towards Scalable Nanocomposite Devices". In: *Scientific reports* 9.1 (2019), p. 17367. DOI: 10.1038/s41598-019-53720-2.

[87] Rajashree Hirlekar et al. "Carbon nanotubes and its applications: a review". In: *Asian Journal of Pharmaceutical and Clinical Research* 2.4 (2009), pp. 17–27.

[88] Sumio Iijima. "Helical microtubules of graphitic carbon". In: *Nature* 354.6348 (1991), pp. 56–58. DOI: 10.1038/354056a0.

[89] Sumio Iijima and Toshinari Ichihashi. "Single-shell carbon nanotubes of 1-nm diameter". In: *Nature* 363.6430 (1993), pp. 603–605. DOI: 10.1038/363603a0.

[90] Michael F. L. de Volder et al. "Carbon nanotubes: present and future commercial applications". In: *Science (New York, N.Y.)* 339.6119 (2013), pp. 535–539. DOI: 10.1126/science.1222453.

[91] Dong Qian et al. "Mechanics of carbon nanotubes". In: *Applied Mechanics Reviews* 55.6 (2002), pp. 495–533. ISSN: 0003-6900. DOI: 10.1115/1.1490129.

[92] Lourdes Agüí, Paloma Yáñez-Sedeño, and José M. Pingarrón. "Role of carbon nanotubes in electroanalytical chemistry: a review". In: *Analytica chimica acta* 622.1-2 (2008), pp. 11–47. DOI: 10.1016/j.aca.2008.05.070.

[93] Deepa Vairavapandian, Pornnipa Vichchulada, and Marcus D. Lay. "Preparation and modification of carbon nanotubes: review of recent advances and applications in catalysis and sensing". In: *Analytica chimica acta* 626.2 (2008), pp. 119–129. DOI: 10.1016/j.aca.2008.07.052.

[94] K. HYEOKA.Y. AN and YOUNG HEE LEE. "ELECTRONIC-STRUCTURE ENGINEERING OF CARBON NANOTUBES". In: *Nano* 01.02 (2006), pp. 115–138. ISSN: 1793-2920. DOI: 10.1142/S1793292006000136.

[95] Riichiro Saito, Gene Dresselhaus, and Mildred S. Dresselhaus. *Physical properties of carbon nanotubes*. London: Imperial College Press, 1998. ISBN: 1-86094-093-5. URL: http://ebooks.worldscinet.com/ISBN/9781860943799/9781860943799.shtml.

[96] Susan B. Sinnott and Rodney Andrews. "Carbon Nanotubes: Synthesis, Properties, and Applications". In: *Critical Reviews in Solid State and Materials Sciences* 26.3 (2001), pp. 145–249. ISSN: 1040-8436. DOI: 10.1080/20014091104189.

[97] Rufan Zhang et al. "Growth of half-meter long carbon nanotubes based on Schulz-Flory distribution". In: *ACS nano* 7.7 (2013), pp. 6156–6161. DOI: 10.1021/nn401995z.

[98] Valentin N. Popov. "Carbon nanotubes: Properties and application". In: *Materials Science and Engineering: R: Reports* 43.3 (2004), pp. 61–102. DOI: 10.1016/j.mser.2003.10.001.

[99] Bertrand Bourlon et al. “Determination of the intershell conductance in multiwalled carbon nanotubes”. In: *Physical Review Letters* 93.17 (2004), p. 176806. ISSN: 0031-9007. DOI: 10.1103/PhysRevLett.93.176806.

[100] Alan B. Kaiser and Viera Skákalová. “Electronic conduction in polymers, carbon nanotubes and graphene”. In: *Chemical Society reviews* 40.7 (2011), pp. 3786–3801. DOI: 10.1039/C0CS00103A.

[101] W. R. Rossen and P. A. Gauglitz. “Percolation theory of creation and mobilization of foams in porous media”. In: *AIChE Journal* 36.8 (1990), pp. 1176–1188. ISSN: 0001-1541. DOI: 10.1002/aic.690360807.

[102] Geoffrey Grimmett. “What is Percolation?” In: *Percolation*. Ed. by S. S. Chern et al. Vol. 321. Grundlehren der mathematischen Wissenschaften. Berlin, Heidelberg: Springer Berlin Heidelberg, 1999, pp. 1–31. ISBN: 978-3-642-08442-3. DOI: 10.1007/978-3-662-03981-6{\textunderscore}1.

[103] David C. Wright, David J. Bergman, and Yacov Kantor. “Resistance fluctuations in random resistor networks above and below the percolation threshold”. In: *Physical review. B, Condensed matter* 33.1 (1986), pp. 396–401. ISSN: 0163-1829. DOI: 10.1103/PhysRevB.33.396.

[104] Arianna Coniglio. “Cluster structure near the percolation threshold”. In: *Journal of Physics A: Mathematical and General* 15.12 (1982), pp. 3829–3844. ISSN: 0305-4470. DOI: 10.1088/0305-4470/15/12/032.

[105] Daniel P. Langley et al. “Percolation in networks of 1-dimensional objects: comparison between Monte Carlo simulations and experimental observations”. In: *Nanoscale horizons* 3.5 (2018), pp. 545–550. DOI: 10.1039/c8nh00066b.

[106] C.-W. Nan, Y. Shen, and Jing Ma. “Physical Properties of Composites Near Percolation”. In: *Annual Review of Materials Research* 40.1 (2010), pp. 131–151. ISSN: 1531-7331. DOI: 10.1146/annurev-matsci-070909-104529.

[107] Hsueh-Chia Chang and Leslie Y. Yeo. *Electrokinetically driven microfluidics and nanofluidics*. Cambridge: Cambridge Univ. Press, 2010. ISBN: 978-0-521-86025-3.

[108] David M. Graham, Mark A. Messerli, and Ronald Pethig. “Spatial manipulation of cells and organelles using single electrode dielectrophoresis”. In: *BioTechniques* 52.1 (2012), pp. 39–43. ISSN: 0736-6205. DOI: 10.2144/000113802.

[109] Joel Voldman. “Electrical forces for microscale cell manipulation”. In: *Annual review of biomedical engineering* 8 (2006), pp. 425–454. ISSN: 1523-9829. DOI: 10.1146/annurev.bioeng.8.061505.095739.

[110] Khashayar Khoshmanesh et al. "Dielectrophoretic platforms for bio-microfluidic systems". In: *Biosensors & bioelectronics* 26.5 (2011), pp. 1800–1814. DOI: 10.1016/j.bios.2010.09.022.

[111] Peilin Zhou et al. "Spatial Manipulation and Assembly of Nanoparticles by Atomic Force Microscopy Tip-Induced Dielectrophoresis". In: *ACS applied materials & interfaces* 9.19 (2017), pp. 16715–16724. DOI: 10.1021/acsami.7b03565.

[112] Junya Suehiro et al. "Dielectrophoretic fabrication and characterization of a ZnO nanowire-based UV photosensor". In: *Nanotechnology* 17.10 (2006), p. 2567. ISSN: 0957-4484. DOI: 10.1088/0957-4484/17/10/021. URL: http://iopscience.iop.org/article/10.1088/0957-4484/17/10/021/pdf.

[113] Mohammad Towshif Rabbani, Mukul Sonker, and Alexandra Ros. "Carbon nanotube dielectrophoresis: Theory and applications". In: *Electrophoresis* 41.21-22 (2020), pp. 1893–1914. ISSN: 0173-0835. DOI: 10.1002/elps.202000049.

[114] Zhong Lin Wang. "Zinc oxide nanostructures: Growth, properties and applications". In: *Journal of Physics: Condensed Matter* 16.25 (2004), R829–R858. ISSN: 0953-8984. DOI: 10.1088/0953-8984/16/25/R01.

[115] Paula Judith Perez Espitia et al. "Zinc Oxide Nanoparticles: Synthesis, Antimicrobial Activity and Food Packaging Applications". In: *Food and Bioprocess Technology* 5.5 (2012), pp. 1447–1464. ISSN: 1935-5130. DOI: 10.1007/s11947-012-0797-6.

[116] Chris G. van de Walle. "Hydrogen as a cause of doping in zinc oxide". In: *Physical Review Letters* 85.5 (2000), pp. 1012–1015. ISSN: 0031-9007. DOI: 10.1103/PhysRevLett.85.1012.

[117] Aleksandra B. Djurišić et al. "ZnO nanostructures: growth, properties and applications". In: *Journal of Materials Chemistry* 22.14 (2012), p. 6526. ISSN: 0959-9428. DOI: 10.1039/C2JM15548F.

[118] Anlian Pan et al. "ZnO flowers made up of thin nanosheets and their optical properties". In: *Journal of Crystal Growth* 282.1-2 (2005), pp. 165–172. ISSN: 00220248. DOI: 10.1016/j.jcrysgro.2005.05.003.

[119] Zhihong Jing and Jinhua Zhan. "Fabrication and Gas-Sensing Properties of Porous ZnO Nanoplates". In: *Advanced Materials* 20.23 (2008), pp. 4547–4551. ISSN: 1521-4095. DOI: 10.1002/adma.200800243.

[120] Hiran D. Kiriarachchi et al. "Growth Mechanism of Sea Urchin ZnO Nanostructures in Aqueous Solutions and Their Photocatalytic Activity for the Degradation of Organic Dyes". In: *ACS omega* 4.9 (2019), pp. 14013–14020. DOI: 10.1021/acsomega.9b01772.

[121] Yogendra Kumar Mishra et al. "Direct Growth of Freestanding ZnO Tetrapod Networks for Multifunctional Applications in Photocatalysis, UV Photodetection, and Gas Sensing". In: *ACS applied materials & interfaces* 7.26 (2015), pp. 14303–14316. DOI: 10.1021/acsami.5b02816.

[122] Haocheng Ji, Wen Zeng, and Yanqiong Li. "Gas sensing mechanisms of metal oxide semiconductors: A focus review". In: *Nanoscale* 11.47 (2019), pp. 22664–22684. DOI: 10.1039/c9nr07699a.

[123] Gang Cheng et al. "ZnO nanowire Schottky barrier ultraviolet photodetector with high sensitivity and fast recovery speed". In: *Applied Physics Letters* 99.20 (2011). ISSN: 0003-6951. DOI: 10.1063/1.3660580.

[124] Jing Wang et al. "Synthesis, properties and applications of ZnO nanomaterials with oxygen vacancies: A review". In: *Ceramics International* 44.7 (2018), pp. 7357–7377. ISSN: 02728842. DOI: 10.1016/j.ceramint.2018.02.013.

[125] Hannes Kind et al. "Nanowire Ultraviolet Photodetectors and Optical Switches". In: *Advanced Materials* 14.2 (2002), pp. 158–160. ISSN: 1521-4095. DOI: 10.1002/1521-4095(20020116)14:2{\textless}158::AID-ADMA158{\textgreater}3.0.CO;2-W.

[126] Leonard Siebert et al. "3D-Printed Chemiresistive Sensor Array on Nanowire CuO/Cu2O/Cu Heterojunction Nets". In: *ACS applied materials & interfaces* (2019). DOI: 10.1021/acsami.9b04385.

[127] Niyom Hongsith et al. "Ethanol sensor based on ZnO and Au-doped ZnO nanowires". In: *Ceramics International* 34.4 (2008), pp. 823–826. ISSN: 02728842. DOI: 10.1016/j.ceramint.2007.09.099.

[128] Robert C. Malenka and Roger A. Nicoll. "Long-term potentiation–a decade of progress?" In: *Science (New York, N.Y.)* 285.5435 (1999), pp. 1870–1874. DOI: 10.1126/science.285.5435.1870.

[129] Natalia Caporale and Yang Dan. "Spike timing-dependent plasticity: a Hebbian learning rule". In: *Annual review of neuroscience* 31 (2008), pp. 25–46. ISSN: 0147-006X.

[130] Timothy V. Bliss and Graham L. Collingridge. "A synaptic model of memory: long-term potentiation in the hippocampus". In: *Nature* 361.6407 (1993), pp. 31–39. DOI: 10.1038/361031a0.

[131] Francisco Varela et al. "The brainweb: phase synchronization and large-scale integration". In: *Nature reviews. Neuroscience* 2.4 (2001), pp. 229–239. DOI: 10.1038/35067550.

[132] Peter J. Uhlhaas et al. "Neural synchrony in cortical networks: history, concept and current status". In: *Frontiers in integrative neuroscience* 3 (2009), p. 17. DOI: 10.3389/neuro.07.017.2009.

[133] Alison Hanson. "Spontaneous electrical low-frequency oscillations: a possible role in Hydra and all living systems". In: *Philosophical transactions of the Royal Society of London. Series B, Biological sciences* 376.1820 (2021), p. 20190763. DOI: 10.1098/rstb.2019.0763.

[134] Heinz Georg Schuster and W. Just. *Deterministic choice: An introduction*. 4th updated and enl. ed. Weinheim: Wiley-VCH, 2005. ISBN: 978-3-527-40415-5.

[135] Stefan Bornholdt and Heinz Georg Schuster. *Handbook of graphs and networks: An interdisciplinary approach*. Weinheim: Wiley-VCH, 2002. ISBN: 3527403361.

[136] Maik-Ivo Terasa et al. "Smart Sensor Arrays". In: *Bio-Inspired Information Pathways*. Ed. by Martin Ziegler, Thomas Mussenbrock, and Hermann Kohlstedt. Vol. 16. Springer Series on Bio- and Neurosystems. Cham: Springer International Publishing, 2023, pp. 265–285. ISBN: 978-3-031-36704-5. DOI: 10.1007/978-3-031-36705-2{_}11.

[137] Tuan D. Ngo et al. "Additive manufacturing (3D printing): A review of materials, methods, applications and challenges". In: *Composites Part B: Engineering* 143.2 (2018), pp. 172–196. ISSN: 13598368. DOI: 10.1016/j.compositesb.2018.02.012.

[138] Kaufui V. Wong and Aldo Hernandez. "A Review of Additive Manufacturing". In: *ISRN Mechanical Engineering* 2012.4 (2012), pp. 1–10. ISSN: 2090-5130. DOI: 10.5402/2012/208760.

[139] Jennifer A. Lewis. "Direct-write assembly of ceramics from colloidal inks". In: *Current Opinion in Solid State and Materials Science* 6.3 (2002), pp. 245–250. ISSN: 13590286. DOI: 10.1016/S1359-0286(02)00031-1.

[140] Jennifer A. Lewis. "Direct Ink Writing of 3D Functional Materials". In: *Advanced Functional Materials* 16.17 (2006), pp. 2193–2204. DOI: 10.1002/adfm.200600434.

[141] Jennifer A. Lewis et al. "Direct Ink Writing of Three-Dimensional Ceramic Structures". In: *Journal of the American Ceramic Society* 89.12 (2006), pp. 3599–3609. ISSN: 00027820. DOI: 10.1111/j.1551-2916.2006.01382.x.

[142] Lisa Rueschhoff et al. "Additive Manufacturing of Dense Ceramic Parts via Direct Ink Writing of Aqueous Alumina Suspensions". In: *International Journal of Applied Ceramic Technology* 13.5 (2016), pp. 821–830. DOI: 10.1111/ijac.12557.

[143] Leonard Siebert et al. "Facile fabrication of semiconducting oxide nanostructures by direct ink writing of readily available metal microparticles and their application as low power acetone gas sensors". In: *Nano Energy* 70.2 (2020), p. 104420. ISSN: 22112855. DOI: 10.1016/j.nanoen.2019.104420.

[144] Joseph Goldstein et al. *Scanning electron microscopy and X-ray microanalysis*. 3. ed. New York: Kluwer Academic/Plenum Publ, 2003. ISBN: 978-0-306-47292-3. URL: http://www.loc.gov/catdir/enhancements/fy0813/2002028276-d.html.

[145] Edward Cohen and E. J. Lightfoot. "Coating Processes". In: *Kirk-Othmer Encyclopedia of Chemical Technology*. Hoboken, NJ, USA: John Wiley & Sons, Inc, 2000. ISBN: 0471238961. DOI: 10.1002/0471238961.1921182203150805.a01.pub3.

[146] Kion Norrman, A. Ghanbari-Siahkali, and N. B. Larsen. "6 Studies of spin-coated polymer films". In: *Annual Reports Section "C" (Physical Chemistry)* 101 (2005), p. 174. ISSN: 0260-1826. DOI: 10.1039/B408857N.

[147] Guillaume Berteloot et al. "Evaporation of a sessile droplet: inside the coffee stain". In: *Journal of colloid and interface science* 370.1 (2012), pp. 155–161. DOI: 10.1016/j.jcis.2011.10.053.

[148] Diederik Depla, S. Mahieu, and J. E. Greene. "Sputter Deposition Processes". In: *Handbook of Deposition Technologies for Films and Coatings*. Elsevier, 2010, pp. 253–296. ISBN: 9780815520313. DOI: 10.1016/B978-0-8155-2031-3.00005-3.

[149] Mai Thanh Nguyen et al. "Double target sputtering into liquid: A new approach for preparation of Ag–Au alloy nanoparticles". In: *Materials Letters* 171 (2016), pp. 75–78. DOI: 10.1016/j.matlet.2016.02.047.

[150] Haile Takele Beyene et al. "Preparation and plasmonic properties of polymer-based composites containing Ag–Au alloy nanoparticles produced by vapor phase co-deposition". In: *Journal of Materials Science* 45.21 (2010), pp. 5865–5871. ISSN: 0022-2461. DOI: 10.1007/s10853-010-4663-5.

[151] Hellmut Haberland et al. "Thin films from energetic cluster impact: A feasibility study". In: *Journal of Vacuum Science & Technology A: Vacuum, Surfaces, and Films* 10.5 (1992), pp. 3266–3271. ISSN: 0734-2101. DOI: 10.1116/1.577853.

[152] Oleksandr Polonskyi et al. "Plasma based formation and deposition of metal and metal oxide nanoparticles using a gas aggregation source". In: *The European Physical Journal D* 72.5 (2018). ISSN: 1434-6060. DOI: 10.1140/epjd/e2017-80419-8.

[153] Alexander Vahl et al. "Single target sputter deposition of alloy nanoparticles with adjustable composition via a gas aggregation cluster source". In: *Nanotechnology* 28.17 (2017), p. 175703. ISSN: 0957-4484. DOI: 10.1088/1361-6528/aa66ef.

[154] Simon Ristig et al. "Nanostructure of wet-chemically prepared, polymer-stabilized silver-gold nanoalloys (6 nm) over the entire composition range". In: *Journal of materials chemistry. B* 3.23 (2015), pp. 4654–4662. DOI: 10.1039/C5TB00644A.

[155] Maik-Ivo Terasa et al. "Sparse CNT networks with implanted AgAu nanoparticles: A novel memristor with short-term memory bordering between diffusive and bipolar switching". In: *PloS one* 17.3 (2022), e0264846. DOI: 10.1371/journal.pone.0264846.

[156] Mirko Hansen et al. "A double barrier memristive device". In: *Scientific Reports* 5.1 (2015), pp. 1–12. ISSN: 2045-2322. DOI: 10.1038/srep13753. URL: https://www.nature.com/articles/srep13753.pdf.

[157] Andrey Sokolov et al. "Partially Oxidized MXene Ti 3 C 2 T x Sheets for Memristor having Synapse and Threshold Resistive Switching Characteristics". In: *Advanced Electronic Materials* 7.2 (2021), p. 2000866. DOI: 10.1002/aelm.202000866.

[158] Alexandros Emboras et al. "Nanoscale plasmonic memristor with optical readout functionality". In: *Nano letters* 13.12 (2013), pp. 6151–6155.

[159] Claudia Hoessbacher et al. "The plasmonic memristor: A latching optical switch". In: *Optica* 1.4 (2014), p. 198. ISSN: 2334-2536. DOI: 10.1364/OPTICA.1.000198.

[160] Daniel C. Ratchford et al. "Quantification of Efficient Plasmonic Hot-Electron Injection in Gold Nanoparticle-TiO2 Films". In: *Nano letters* 17.10 (2017), pp. 6047–6055. DOI: 10.1021/acs.nanolett.7b02366.

[161] Yevgeniy S. Puzyrev et al. "Memristive devices from ZnO nanowire bundles and meshes". In: *Applied Physics Letters* 111.15 (2017), p. 153504. ISSN: 0003-6951. DOI: 10.1063/1.5008265.

[162] Phuong Y. Le et al. "Electroformed, Self–Connected Tin Oxide Nanoparticle Networks for Electronic Reservoir Computing". In: *Advanced Electronic Materials* (2020), p. 2000081. DOI: 10.1002/aelm.202000081.

[163] Yangyin Chen. "ReRAM: History, Status, and Future". In: *IEEE Transactions on Electron Devices* 67.4 (2020), pp. 1420–1433. ISSN: 0018-9383. DOI: 10.1109/TED.2019.2961505.

[164] Chao Du et al. "Reservoir computing using dynamic memristors for temporal information processing". In: *Nature communications* 8.1 (2017), p. 2204. DOI: 10.1038/s41467-017-02337-y.

[165] Henry O. Sillin et al. "A theoretical and experimental study of neuromorphic atomic switch networks for reservoir computing". In: *Nanotechnology* 24.38 (2013), p. 384004. ISSN: 0957-4484. DOI: 10.1088/0957-4484/24/38/384004.

[166] Ed Bullmore and Olaf Sporns. "Complex brain networks: graph theoretical analysis of structural and functional systems". In: *Nature reviews. Neuroscience* 10.3 (2009), pp. 186–198. DOI: 10.1038/nrn2575.

[167] Maik-Ivo Terasa et al. "Pathways towards truly brain-like computing primitives". In: *Materials Today* (2023). ISSN: 13697021. DOI: 10.1016/j.mattod.2023.07.019.

[168] Marcus Kaiser. "Mechanisms of Connectome Development". In: *Trends in cognitive sciences* 21.9 (2017), pp. 703–717. DOI: 10.1016/j.tics.2017.05.010.

[169] Tom Birkoben. *Dynamics meets Morphology : towards Dymorph Computation*. Kiel: Universitätsbibliothek Kiel, 2021. URL: https://macau.uni-kiel.de/servlets/MCRFileNodeServlet/macau_derivate_00003601/Dissertation%20Birkoben.pdf.

[170] Liguo Qin et al. "Economic Friendly ZnO-Based UV Sensors Using Hydrothermal Growth: A Review". In: *Materials (Basel, Switzerland)* 14.15 (2021). ISSN: 1996-1944. DOI: 10.3390/ma14154083.

[171] Sigurd Wagner et al. "Electronic skin: Architecture and components". In: *Physica E: Low-dimensional Systems and Nanostructures* 25.2-3 (2004), pp. 326–334. ISSN: 13869477. DOI: 10.1016/j.physe.2004.06.032.

[172] Xiandi Wang et al. "Recent Progress in Electronic Skin". In: *Advanced science (Weinheim, Baden-Wurttemberg, Germany)* 2.10 (2015), p. 1500169. ISSN: 2198-3844. DOI: 10.1002/advs.201500169.

[173] Joseph C. Anderson. "Measuring breath acetone for monitoring fat loss: Review". In: *Obesity (Silver Spring, Md.)* 23.12 (2015), pp. 2327–2334. DOI: 10.1002/oby.21242.

[174] Vasile Postica et al. "Tuning doping and surface functionalization of columnar oxide films for volatile organic compound sensing: Experiments and theory". In: *Journal of Materials Chemistry A* 6.46 (2018), pp. 23669–23682. ISSN: 2050-7488. DOI: 10.1039/c8ta08985j.

[175] Vasile Postica et al. "Tuning ZnO Sensors Reactivity toward Volatile Organic Compounds via Ag Doping and Nanoparticle Functionalization". In: *ACS applied materials & interfaces* 11.34 (2019), pp. 31452–31466. DOI: 10.1021/acsami.9b07275.

[176] Alexander Vahl et al. "Surface functionalization of ZnO: Ag columnar thin films with AgAu and AgPt bimetallic alloy nanoparticles as an efficient pathway for highly sensitive gas discrimination and early hazard detection in batteries". In: *Journal of Materials Chemistry A* 8.32 (2020), pp. 16246–16264. ISSN: 2050-7488. DOI: 10.1039/d0ta03224g.

[177] Oleg Lupan et al. "Ultra-thin TiO 2 films by atomic layer deposition and surface functionalization with Au nanodots for sensing applications". In: *Materials Science in Semiconductor Processing* 87 (2018), pp. 44–53. ISSN: 13698001. DOI: 10.1016/j.mssp.2018.06.031.

[178] Nicolai Ababii et al. "Effect of noble metal functionalization and film thickness on sensing properties of sprayed TiO2 ultra-thin films". In: *Sensors and Actuators A: Physical* 293 (2019), pp. 242–258. ISSN: 09244247. DOI: 10.1016/j.sna.2019.04.017.

[179] Cristian Lupan et al. "Pd-Functionalized ZnO: Eu Columnar Films for Room-Temperature Hydrogen Gas Sensing: A Combined Experimental and Computational Approach". In: *ACS applied materials & interfaces* 12.22 (2020), pp. 24951–24964. DOI: 10.1021/acsami.0c02103.

[180] Oleg Lupan et al. "Functionalized Pd/ZnO Nanowires for Nanosensors". In: *physica status solidi (RRL) - Rapid Research Letters* 12.1 (2018), p. 1700321. ISSN: 18626254. DOI: 10.1002/pssr.201700321.

[181] Oleg Lupan et al. "PdO/PdO2 functionalized ZnO: Pd films for lower operating temperature H2 gas sensing". In: *Nanoscale* 10.29 (2018), pp. 14107–14127. DOI: 10.1039/c8nr03260b.

[182] Oleg Lupan et al. "Properties of a single SnO2: Zn2SnO4 – Functionalized nanowire based nanosensor". In: *Ceramics International* 44.5 (2018), pp. 4859–4867. ISSN: 02728842. DOI: 10.1016/j.ceramint.2017.12.075.

[183] Oleg Lupan et al. "Additive Manufacturing as a Means of Gas Sensor Development for Battery Health Monitoring". In: *Chemosensors* 9.9 (2021), p. 252. DOI: 10.3390/chemosensors9090252.

[184] Fabian Schütt et al. "Conversionless efficient and broadband laser light diffusers for high brightness illumination applications". In: *Nature communications* 11.1 (2020), p. 1437. DOI: 10.1038/s41467-020-14875-z.

[185] Lidia Ghimpu et al. "Individual CdS-covered aerographite microtubes for room temperature VOC sensing with high selectivity". In: *Materials Science in Semiconductor Processing* 100.23 (2019), pp. 275–282. ISSN: 13698001. DOI: 10.1016/j.mssp.2019.05.013.

[186] Oleg Lupan et al. "Room temperature gas nanosensors based on individual and multiple networked Au-modified ZnO nanowires". In: *Sensors and Actuators B: Chemical* 299 (2019), p. 126977. ISSN: 09254005. DOI: 10.1016/j.snb.2019.126977.

[187] Muchao Qu et al. "Structure changes of aligned carbon nanotubes in thermoplastics below percolation revealed by impedance spectroscopy". In: *Applied Nanoscience* 8.8 (2018), pp. 2071–2075. ISSN: 2190-5509. DOI: 10.1007/s13204-018-0865-y.

[188] Semiconductor Components Industries, LLC. *2N6027 Programmable Unijunction Transistor*. 2004.

[189] Robert Boylestad and Louis Nashelsky. *Electronic devices and circuit theory*. 7., international ed. Upper Saddle River, NJ: Prentice-Hall Internat, 1999. ISBN: 013769282x.

[190] Marina Ignatov et al. "Synchronization of two memristively coupled van der Pol oscillators". In: *Applied Physics Letters* 108.8 (2016), p. 084105. ISSN: 0003-6951. DOI: 10.1063/1.4942832.

[191] Marina Ignatov et al. "Memristive stochastic plasticity enables mimicking of neural synchrony: Memristive circuit emulates an optical illusion". In: *Science advances* 3.10 (2017), e1700849. DOI: 10.1126/sciadv.1700849.

Appendix A

A.1 Equation for Filament Growth Speed

The derivation of the growth speed of a conductive filament in an electrochemical metallization cell is based on Faraday's law of electrolysis, correlating deposited mass m with transferred charge Q:

$$m = \frac{QM_{Me}}{Fz} \tag{A.1}$$

where $M_{Me} = m_{Me} * N_A$ is the molar mass of the deposited metal, $F = e * N_A$ is Faraday's constant and z is the valence of the metal.
Eliminating the Avogadro constant N_A from M_{Me} and F and substituting m yields

$$V * \rho_{Me} = -\frac{Qm_{Me}}{ez} \tag{A.2}$$

with V and ρ_{Me} being the volume of the filament and the density of the metal respectively as well as m_{Me} being the atomic mass of the metal and $-e$ the elementary charge of an electron. When it is now assumed, that the cross section A of the filament is constant, the equation can be reformed to

$$x * A = -\frac{Qm_{Me}}{\rho_{Me}ez} \tag{A.3}$$

with x being the filament length in growth direction.
Finally, by deriving with respect to the time t one obtains the expression

$$\frac{\partial x}{\partial t} = -\frac{m_{Me}}{\rho_{Me}ez} * J_{Me} \tag{A.4}$$

relating the growth of x over time to the ionic current density J_{Me}.

A.2 Retention time versus *SET* pulse width

The time-resolved current measurement shown in *Figure 3.11* has shown a positive correlation between the retention time and SET pulse width.
Since the reset to the HRS does not occur immediately, two data points have been taken for each *SET* pulse width: The start of the current decline as well as the time the current reaches the HRS level again.
The grey line represents a quadratic fit of the lower data points in the form of $Ax^2 + Bx + C$ with the values $A = 4.1$, $B = 4.3$, $C = 0$.

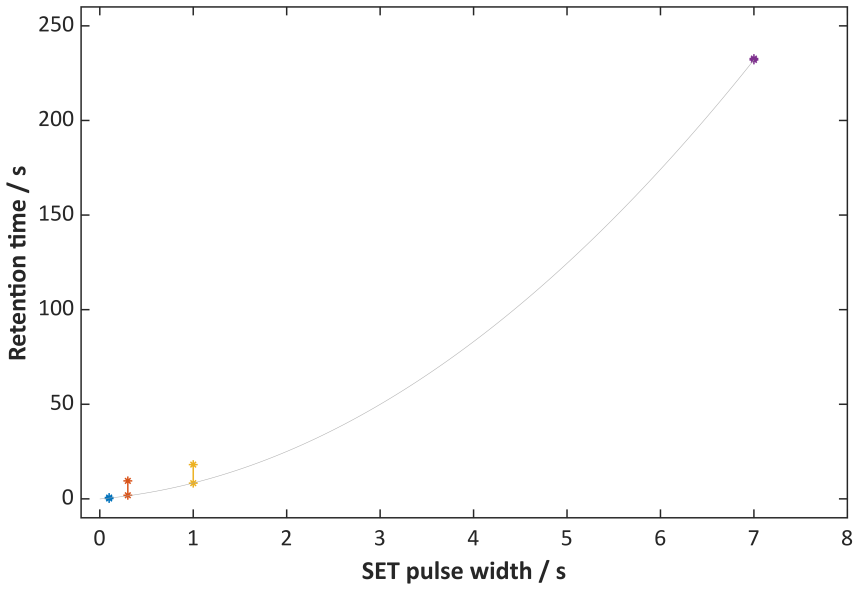

Figure A.1: *Retention time over SET pulse width from the current measurement in Figure 3.11.*

A.3 Details of the Relaxation Type Oscillators

The following paragraph is directly excerpted from the Supporting Material S2 of [167].

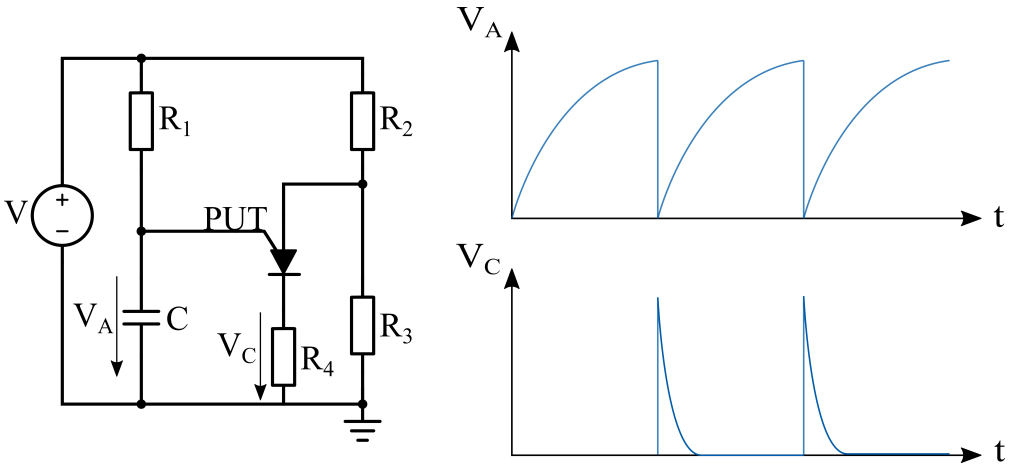

Figure A.2: *Circuit diagram of the relaxation oscillators. On the right the time evolution of V_A and V_C as indicated in the diagram are shown.*

We applied van der pol relaxation-type oscillators based on programmable unijunction transistors 2N6027 (PUTs) in order to mimic leaky integrate and fire neurons (LIF) in electrical circuits (see *Figure A.2*). The PUT is a four-layer diode and has a strongly non-linear I-V curve[188, 189]. The device has two possible states, an off (high resistance) and on (low resistance) state. In the off state no current can flow from anode to cathode. When the voltage difference from anode to cathode reaches the threshold the device switches into the on state and a current can flow. Only when the current drops below the valley current switches the PUT back into the off state. The threshold voltage can be programmed by the resistors R2 and R3. In the oscillator circuit the resistor R1 in series to capacitor C is used to generate a charging current for the capacitor. The capacitor voltage increases through the charging current and therefore the voltage from anode to cathode of the PUT. When the threshold is reached the PUT switches into the on state and the capacitor gets discharged over the resistor R4. When the charge decreases also the current decreases until it is below the valley current. Here, the PUT switches back into the off state. The coupling of two and more PUT oscillators compromising solid state memristive devices has been studied in previous works[190, 191].